Hydrogen production from irradiated calcium silicate hydrate

Chengying Yin

UNIVERSITÉ PARIS SUD
Comprendre le monde, construire l'avenir

Hydrogen production from irradiated calcium silicate hydrate

Thèse de doctorat de l'Université Paris-Saclay
préparée à l'Université Paris-Sud

École doctorale n°571 Sciences chimiques : molécules, matériaux, instrumentation et biosystèmes (2MIB)
Spécialité de doctorat Chimie

Thèse présentée et soutenue à Marcoule, 15, Novembre, 2019 par

Chengying YIN

Composition du Jury :

M. Mehran Mostafavi Professeur, Université Paris-Saclay	Président
Mme. Isabelle Pochard Maître de Conférences HDR CNRS, Institut UTINAM, Besançon	Rapporteur
Mme. Nathalie Moncoffre Directrice de Recherche CNRS, IP2I-Lyon	Rapporteur
M. Jean-Baptiste d'ESPINOSE de LACAILLERIE Professeur, ESPCI Paris	Examinateur
M. Jean-Philippe Renault Chercheur CEA, CEA Saclay	Directeur de thèse
Mme. Adeline Dannoux-Papin Chercheur CEA, CEA Marcoule	Encadrant de thèse
M. Jérémy Haas Chercheur CEA, CEA Marcoule	Encadrant de thèse

Les ciments Portland utilisés pour le conditionnement ou l'enrobage de déchets radioactifs sont principalement composés de phases silicates et aluminates dont l'hydratation conduit à la formation de deux hydrates principaux, les hydrates de silicate de calcium (C-S-H) et la portlandite ($Ca(OH)_2$). Le comportement de la pâte de ciment sous irradiation est bien connu dans la littérature en termes de radiolyse de l'eau interstitielle et donc d'émission d'hydrogène radiolytique. Leur stabilité sous irradiation pouvant atteindre l'ordre de plusieurs GGy de doses absorbées en font des matériaux de choix pour les déchets d'emballages. De plus, une diminution de la résistance mécanique s'explique par la décomposition des hydrates, l'apparition de phases amorphes et la dissociation de l'eau chimiquement liée. Enfin, l'hydrogène radiolytique est principalement produit par radiolyse de l'eau interstitielle ("libre"). Des études récentes ont montré que l'eau d'hydratation ("liée") de différents hydrates contribue également. De plus, l'eau à l'interface des hydrates inclus dans le ciment joue un rôle essentiel. Bien que l'effet de l'irradiation sur la microstructure et l'émission d'hydrogène radiolytique aient été étudiés, il reste peu de connaissances sur la radiolyse de l'eau à l'interface des hydrates et comment elle contribue à la stabilité du matériau cimentaire sous irradiation. Selon certains auteurs, certains effets spécifiques devraient être attendus dans des matériaux tels que les transferts d'énergie ou la diffusion d'espèces radiolytiques transitoires dans le solide et/ ou à l'interface eau/ solide. Les défauts électroniques dus au rayonnement dans les différents hydrates (CSH, portlandite, ...) du ciment sont inconnus. Mais identifier et étudier leur stabilité est la clé pour comprendre les mécanismes impliqués dans la radiolyse de l'eau dans un environnement complexe.Le but de cette étude est de comprendre les mécanismes radiolytiques de la production d'hydrogène dans la CSH, d'étudier l'effet des impuretés (telles que les ions alcalins, les hydroxydes supplémentaires ou les ions nitrates) sur la production de gaz H_2 dans la CSH et d'examiner s'il existe des interactions entre les différents phases principales (CSH et portlandite) dans la matrice de ciment. Après avoir utilisé diverses techniques de caractérisation, les échantillons ont été soumis à différents types d'irradiation (rayons gamma et électrons et faisceaux d'ions lourds (HI)) pour déterminer leur rendement radiolytique en H_2, G (H_2). Dans le système C-S-H, il a été démontré, sous irradiation gamma, que le G (H_2) ne dépend pas de la teneur en eau.En outre, le système C-S-H produit lui-même efficacement du gaz H_2. La comparaison entre les résultats obtenus sous rayons gamma et ceux obtenus sous HI implique: il n'y a pas/ peu d'effet LET en C-S-H. Alors qu'avec les ions nitrate en C-S-H, une forte diminution de G (H_2) est observée. L'irradiation des hydrates de C2S et C3S

principalement composés de C-S-H et de portlandite montre qu'il n'y a pas de phénomène de transfert d'énergie entre ces deux phases. Enfin, les expériences de spectroscopie par résonance paramagnétique électronique (EPR) ont permis de proposer des mécanismes radiolytiques. Tous ces résultats nous aident à comprendre les effets des rayonnements dans les ciments.

Acknowledgments

Firstly, I would like to express my sincere gratitude to my supervisors Adeline Dannoux-Papin and Jérémy Haas, for their guidance helped me in all the time of research and writing of this thesis. Thank you for your patience. As well as my director Jean-Philippe Renault, for the scientific advice and important discussion during the thesis, for his patience and immense knowledge.

Besides my advisors, I would like to thank the rest of my thesis committee: Isabelle Pochard, Nathalie Moncoffre, Mehran Mostafavi, Jean-Baptiste d'Espinose de LACAILLERIE, for accepting the invitation to be the members of jury of my thesis.

I would like to thank the chiefs of LCBC, Stéphane Perrin and Fabien Frizon, for their help during the thesis. Thank you all for receiving me in your laboratory and allowing me to use research facilities.

My deepest thanks go to Stéphane Esnouf for helping me on the EPR experiments and for teaching me to perform the analysis from the very beginning, this thesis work cannot be conducted without you! I won't forget how kind you were! Thank you so much.

I would like to express my gratitude to Arnaud Poulesquen, for SAXS/ WAXS analysis and TEM experiments, Thank you for the help, for your clear explanation, your time and your kindness.

My sincere thanks also go to Jennifer Sanchez-Canet, Pascal Antonucci, Karine Ressayre, Thomas Piallat, David Rudloff, Aderine Gerenton, Géraldine Dideron, Maryline Charlot-Ortega, Leslie Berthillot, Véronique Labed.

I would like to thank David Chartier, Céline Cau-Dit-Coumes, Jean-Baptiste Champenois, and David Lambertin, they had always encouraging words and pertinent scientific advice.

I thank my fellow labmates Birsen, Jihane, Pauline, Oriane, Nicolas, Frédéric, Svetlana, Donatien, Julien and Priscillia, for all the fun we have had in the last three years.

I take this opportunity to express gratitude to all of the administration group in the lab for helping me focusing the research, they are Myriam Capion, Kelly Salomez, and Xia Lo.

Last but not least, I would like to thank my family: my parents for supporting me spiritually throughout writing this thesis and my life in general.

List of contents

List of Tables

List of Figures

Glossary

Cement chemistry notations:

C=CaO S=SiO_2 H=H_2O

Hydrated phases:

C-S-H Calcium silicate hydrate

C2S hydrates Dicalcium silicate hydrate

C3S hydrates Tricalcium silicate hydrate

Techniques:

ICP-AES Inductively coupled plasma atomic emission spectroscopy

IC Ion chromatography

XRD X-Ray diffraction

TGA Thermogravimetric analysis

DVS Dynamic vapor sorption

EPR Electron paramagnetic resonance

TEM Transmission electron microscope

WAXS/ SAXS Wide and Small-Angle X-Ray Scattering

Divers:

OPC Ordinary Portland cement

BET Brunauer-Emmett-Teller

LET Linear energy transfer

Micro-GC Micro-gas chromatography

RID Radiation induced defect

INTRODUCTION

Radioactive waste can be classified according to a number of criteria: origin, physical and chemical nature, level and type of radioactivity, lifetime, etc. In France, radioactive waste is managed according to classification based on:

- Its radioactivity
- Its lifetime

There are six categories of radioactive waste (Figure 1):

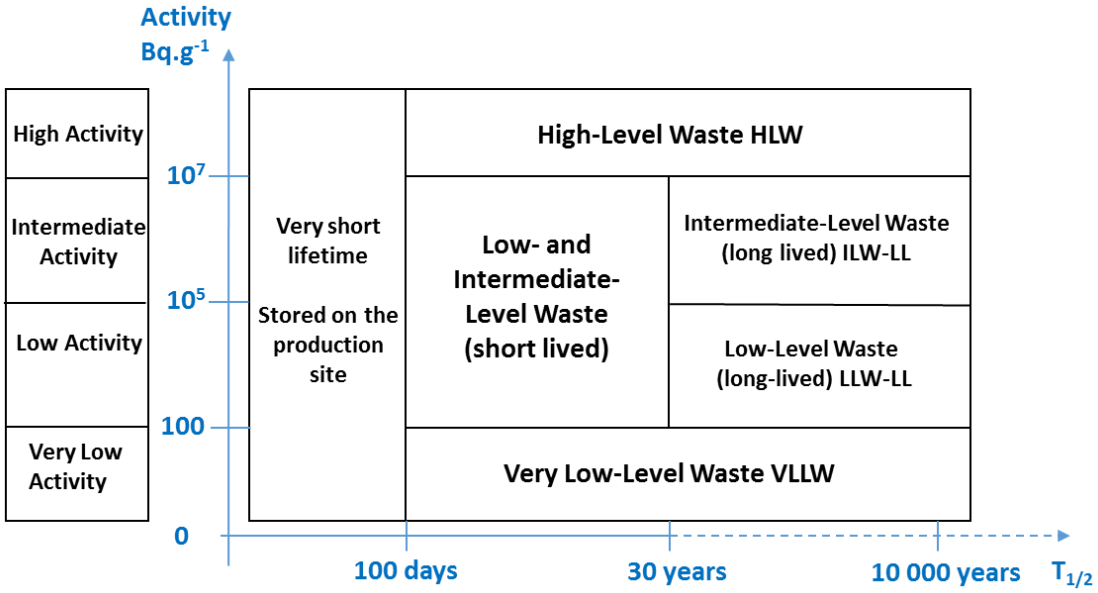

Figure 1. Simplified classification of radioactive waste according to its radioactivity and its lifetime. Reproduced from [1].

According to ANDRA's National Inventory of Radioactive Materials and Waste 2012, as at the end of 2010, LILW-SL accounted for 63% of the total volume of radioactive waste produced in France, or 830,000 m^3 and 0.02% of the total radioactivity of radioactive waste in France. Those low and intermediate level wastes issued from the dismantling of nuclear facilities are usually conditioned in calcium silicate cement to ensure the stability and the confinement of the radioactivity for disposal and future geological storage (see Figure 2).

The use of a cement matrix has been considered because it has many advantages. It is inexpensive, easy to produce and can be tailored to reach various different properties such as soundness, strength. In addition, the alkalinity of certain cements allows them to insolubilize a large number of radionuclides and thus limit their diffusion [2]. Cementitious matrices thus rank as reference materials for low and intermediate-level waste conditioning, whether for their storage or their surface or geological disposal.

However, the conditioning of radioactive waste in a cementitious matrix poses many problems when cement are submitted to ionizing radiation, from the interaction between cement and radioactive waste [3].

Figure 2. 500-litre container for ILW [4]

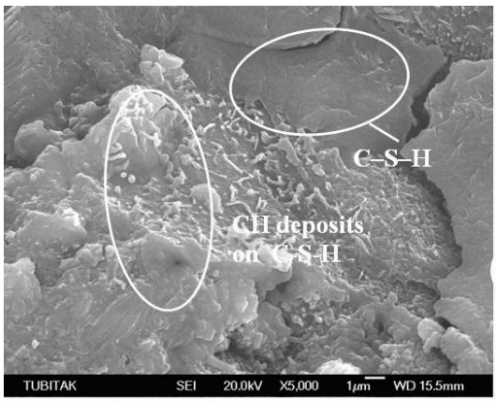

Figure 3. SEM images of the mortar specimens after 28 days of curing OPC [5]

Concrete is a composite material composed of fine and coarse aggregates bonded by cement paste. The cement paste is an assembly of different anhydrous phases and hydrated phases or hydroxides (see Figure 3), containing a significant amount of water that is trapped in its porosity. Therefore, radiation effects are encountered when the cement paste is exposed under ionizing radiation. Numerous studies have therefore conducted to determine the impact of radiation [6-14].

Structure modifications and radiolytic gas production under ionizing radiation have been studied [15]. The results show that until very high dose (GGy), the hydrates exhibit a good structural resistance without amorphization under irradiation.

As a matter of fact, irradiation consequences mostly emerge as the residual water radiolysis and gaseous dihydrogen emanation, to consider long-term storage. Indeed these packages of waste need to meet the criteria defined by the ANDRA who requires the limitation of H_2 released. Therefore, in our study, we only focused on hydrogen production.

In reality, when cemented waste packages display a complex radiological inventory with fission (or activation) products and actinides (fuel clads, for example), there are different radiation field emitted, such as γ rays, β rays and α rays. Therefore, different radiation sources were used in our studies, such as gamma rays, electron and heavy ions beam radiations.

Cement paste is mainly composed of calcium silicate hydrates (abbreviated C-S-H) and portlandite. It also contains residual clinker (that only partially reacted with water) such as alite, belite and ferrite. Since it is a material with various possible compositions and a complex nano- and micro- structure [16,17], the radiolytic process leading to hydrogen release in such material is challenging and not well understood. The behavior of cement paste [6,7] [17-21] under irradiation is usually described in the literature in terms of the radiolysis of pore water and therefore the radiolytic hydrogen emission. However, this is not completely understood and recent studies have shown that, besides the pore water, the water of hydration ("bound") of different hydrates contributes as well to the radiolytic hydrogen production [22,23]. In such hydrated compounds, radiolysis is not well described and the literature is quite limited.

The purpose of the present work is to understand the water radiolysis in the calcium silicate hydrates (C-S-H), which is the main hydration product of Portland cement and how the interface between solid and water can modify the radiolytic mechanisms.

We tried to take into account the fact that:

i) The irradiation could occur in different humidity

ii) The structure and composition of the material could be modified.

CHAPTER 1: Literature review

In this chapter, the hydration of Portland cement, the structure of Calcium Silicate Hydrates usually will be presented. Then the basics of the interaction of radiation with matter will be introduced. At the end of the chapter, state-of-the-art on the radiolysis of absorbed and confined water in solids will be presented.

1.1. Cement chemistry

1.1.1. Portland cement

Ordinary Portland cement (OPC) is made by heating limestone and clay in a kiln at about 1450°C, which chemically transforms into hard nodules called clinker. The typical oxides composition is about 67% CaO, 22% SiO_2, 5% Al_2O_3, 3% Fe_2O_3 and 3% other components constituting the four major phases, called alite ($3CaO\ SiO_2$), belite ($2CaO\ SiO_2$), aluminate and ferrite. Several other phases, such as alkali sulfates and calcium oxide, are normally present in minor amounts.

The clinker is mixed with a few percents of calcium sulfate to be grinded and resulting in the finely ground powder named cement. The calcium sulfate hydrate, usually called gypsum, is actually added to control the hydration mechanism and to improve the strength development.

The hardening to form the well-known final material results from hydration reactions between the major phases contained in cement powder and water. This hydration process leads to the formation of hydrated calcium silicates (C-S-H) (50%), the main hydrate of OPC, portlandite ($Ca(OH)_2$) (20%), as well as hydrated calcium aluminates and sulfoaluminates (ettringite and monosulfoaluminate) [24].

1.1.2. Calcium silicate hydrate

The calcium silicate hydrate, the main product of the reaction of Portland cement with water, are formed during the hydration of C_3S ($3CaO.SiO_2$) or beta-C_2S ($2CaO.SiO_2$).

1.1.2.1. Chemical composition

The chemical composition of calcium silicate hydrate (C-S-H) is thought to substantially affect many properties of concrete, and is primarily responsible for the strength in cement based materials [24]. The C-S-H composition evolution with C/S ratio were examined by many authors [25-31] (Figure 1. 1). Two main types of results are published and analysed: the first, from C-S-H directly made from CaO and SiO_2 diluted suspensions, the second are related to the C-S-H formed in paste of Portland cement or C_3S with or without mineral additions such as silica fumes, slag or fly ashes. The first type of preparation limits the C/S ratio of C-S-H between about 0.6 to 1.5 [32]. The second types of studies devoted to C-S-H from cement pastes, reveals an higher C/S ratio of C-S-H, about 1.75 [32].

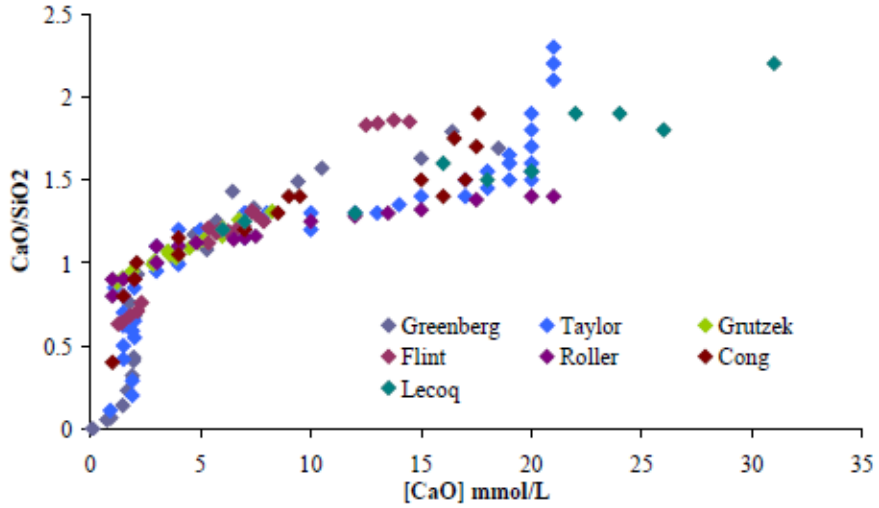

Figure 1. 1. Evolution of the stoichiometry of C-S-H as a function of the hydroxide concentration Calcium solution (Taylor, 1950) (Cong and Kirkpatrick, 1996) (Lecoq, 1993) (Grutzek, 1989) (Roller, 1940) (Flint and Wells, 1934) (Greenberg, 1965) from Courault [38].

1.1.2.2. Structure

Whatever was the C/S ratio between 0.7 and 1.5, X-ray diffraction patterns are very similar. Although C-S-H is poorly crystalline, some diffraction peaks can be observed, they are shown in Figure 1. 2. In XRD patterns, the maximum at 7.2-9.3° 2Θ corresponds to (001) reflection using the structural model from [33][35][37][51]. It varies in position depending on the distance between two calcium plans in the structure of the C-S-H.

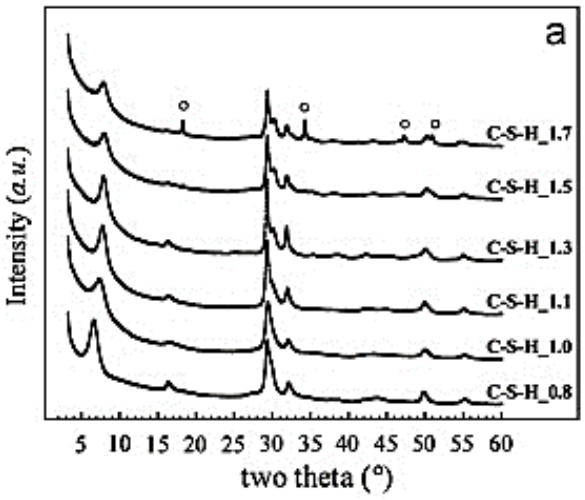

Figure 1. 2. X-ray powder diffraction of C-S-H with different Ca/Si ratio (circle indicates the presence of portlandite). Reproduced from [34].

The most accepted descriptions are based on the crystal structures of natural minerals: jennite [35,36] and tobermorite [37][51]. In tobermorite, a non-hydroxylated CaO layer is present, while in jennite, calcium in the main layer is hydroxylated. Three different types of tobermorite are generally distinguished: 14Å, 11Å or 9Å with different basal spacing structure and water content [39]. The most used model to characterize C-S-H is the 11Å tobermorite. It can be described as a calcium plan with silica chains on its both sides organized in a "drieierketten" structure. A repeated chain of three silica tetrahedral are shown below in Figure 1. 3. Two of these silica tetrahera are linked to the calcium planes and are called pairing tetrahedra, while the third tetrahedron, linking the two pairing tetrahedral, is called bridging tetrahedron. The layers are stacked together and are separated by an interlayer space, which may contain water molecules, calcium ions, alkalis and other ions [40].

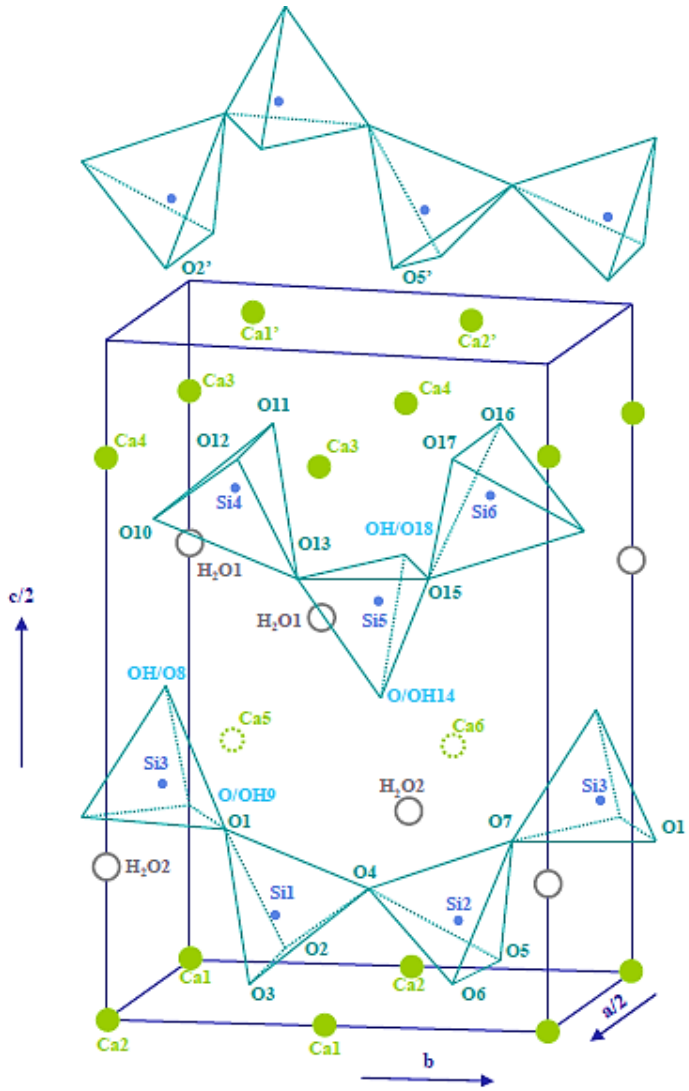

Figure 1. 3. Structure of 11Å tobermorite, Hamid [40], a/2=5.58 Å, b=7.39 Å, and c/2=11.389 Å,

1.1.3. Specific surfaces of CSH

CSH exhibits layered or sheet-shape objects arranged in a dense and laminar pattern, as shown on Figure 1. 4.

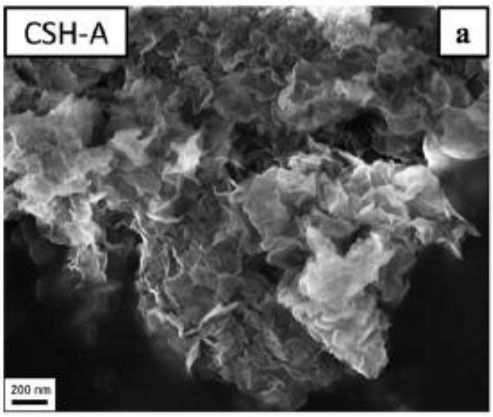

Figure 1. 4. SEM micrograph of C-S-H, when C/S=1 [41]

The morphology of the C-S-H gel at the nanoscale has also been investigated by small-angle X-ray [42-45] and neutron scattering [46-49]: the average number of stacking layers increases with the water content, from 4.5 (with 10% water content) to 11 (with 30% water content) [50], the total thickness of the globule is 4-10 nm. The observation with atomic force microscope supposes those C-S-H nanoparticles are 60×30 nm^2 and 5 nm thick [51]. The crystallite size perpendicular to the layer plane is 4–5 nm [52].

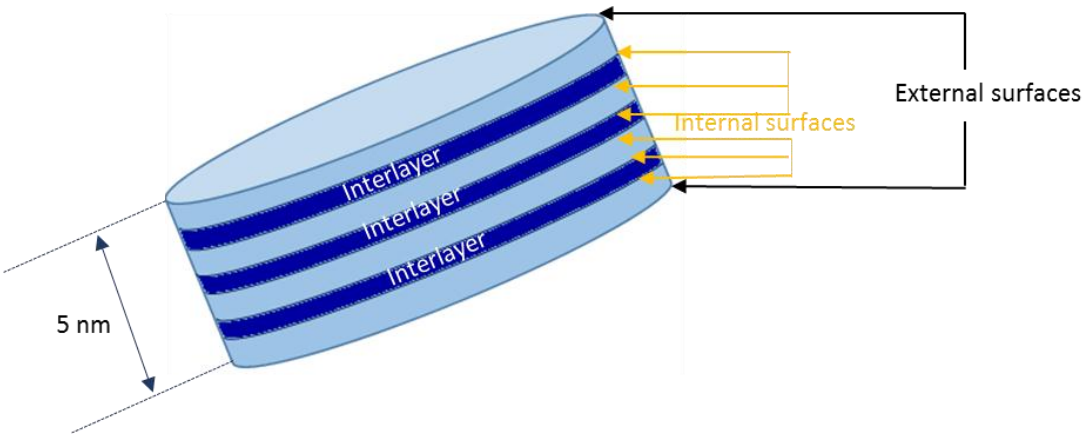

Figure 1. 5. Schematic representation of the stack of sheets for a C-S-H particle.

As with many layered compounds, external and internal (interlayer) surfaces (see Figure 1. 5) of C-S-H enable multilayer water molecules adsorption to the hydrophilic surfaces. In order to investigate the changing of the developed surface depending on the C/S, the specific surface area has been investigated with different gases or vapors, such as N_2, H_2O, and CH_3OH, calculated from [53]:

- Surface chemical theory;
- The knowledge of the cross-section of one molecule of the gas used;
- The number of molecules required to cover a surface completely.

Table 1. Surface area from BET theory of Analysed CSH samples measured from Nitrogen adsorption volumetry [53]

Samples	**Effective C/S ratio**	**S_{BET} (m^2/g)**
CSH 0.6	0.69	408
CSH 0.8	0.82	356
CSH 1.0	1.06	271
CSH 1.2	1.23	194
CSH 1.6	1.42	231

In the work of C. Roosz and co-workers [53], the calculated BET specific surface areas (S_{BET}) decreased with increasing C/S ratio from 408 (C/S=0.6) to 194 m^2/g (C/S=1.2) (see Table 1). The S_{BET} evolution could be explained by considering an increase of the particle size from 4 (CSH 0.6) to 8 nm (C-S-H 1.2) [53], inducing a decrease of the particle external surface. At higher ratios, C-S-H with C/S=1.6 displays a higher value (231 m^2/g) than C-S-H with C/S=1.2. This could be attributed to the precipitation of portlandite nanoparticles during the drying step, which tends to increase the surface area of the C-S-H with C/S=1.6 [53].

The water distribution in the C-S-H microstructure has been described by Water vapour isotherms experiments [53]. The calculated BET specific surface areas (S_{BET}) for the adsorption branch decrease with increasing Ca/Si from 431 (CSH 0.6) down to 180 m^2/g (CSH 1.6) (Table 2), in agreement with the N_2 external surface area S_{BET} and increasing particle size.

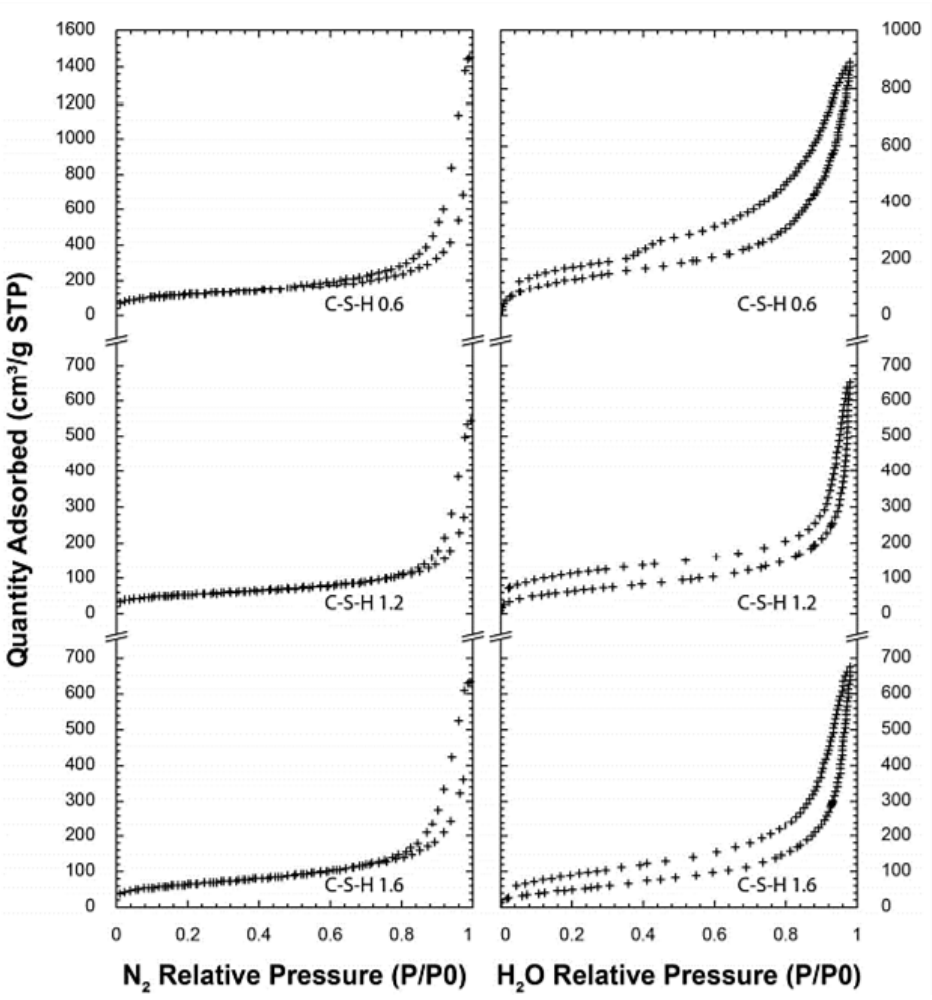

Figure 1. 6. Nitrogen and water vapor adsorption/desorption isotherms of C-S-H 0.6, 1.2 and 1.6 samples. [53]

Table 2. Surface area from BET theory of Analysed CSH samples measured from Water Vapour Isotherms [53].

Samples	**Effective C/S ratio**	**S_{BET} (m^2/g)**
CSH 0.6	0.69	431
CSH 1.2	1.23	214
CSH 1.6	1.42	180

1.1.3.1. Surface charge

The bridging silicate tetrahedra and the tetrahedra at the ends of the chains possess unlinked oxygen atoms, forming Si-OH groups that are also called silanol sites. The increase of the pH induces a partial dissociation of silanol group according to the following equilibrium to give a negative charge [54]:

$$\equiv SiOH + HO^- \longrightarrow \equiv SiO^- + H_2O$$

Since C-S-H are stable in alkaline solutions, the silanol sites are therefore carrying a negative charge. This charge is compensated by the Ca^{2+} present in the interlayer or on the surface to ensure electroneutrality.

1.1.4. Texturation

Based on the experimental data obtained about C-S-H, Jennings proposes a nanostructural model describing quantitatively the organisation of the elementary bricks and the porous network. The assembly of spheroidal elementary bricks flocculate to form larger and well-defined units is considered [55]. These elemental units are "disks" with a section transverse 5 nm described previously [56]. This textural pattern also defines distinct pores, interlayer spaces, which allows to model the density of C-S-H under different relative humidity conditions (Figure 1. 7). The globules are particles of nanometer dimension that assemble into statistically well-defined patterns. Water-filled spaces include:

- The interlayer spaces= 0.9-1.4 nm, refers to the porosity inside the globule,
- The intraglobule spaces (IGP) $<$ 1 nm, refers to the porosity inside the globule
- The small gel pores (SGP) = 1-3 nm, refers to very small porosity trapped between the globules ,
- The large gel pores (LGP) = 3-12 nm, refer to porosity trapped between the globules.

In each type of pores, the water has a specific thermodynamic character. The most tightly bound water is absorbed on the surface of the globules and within the IGP [56].

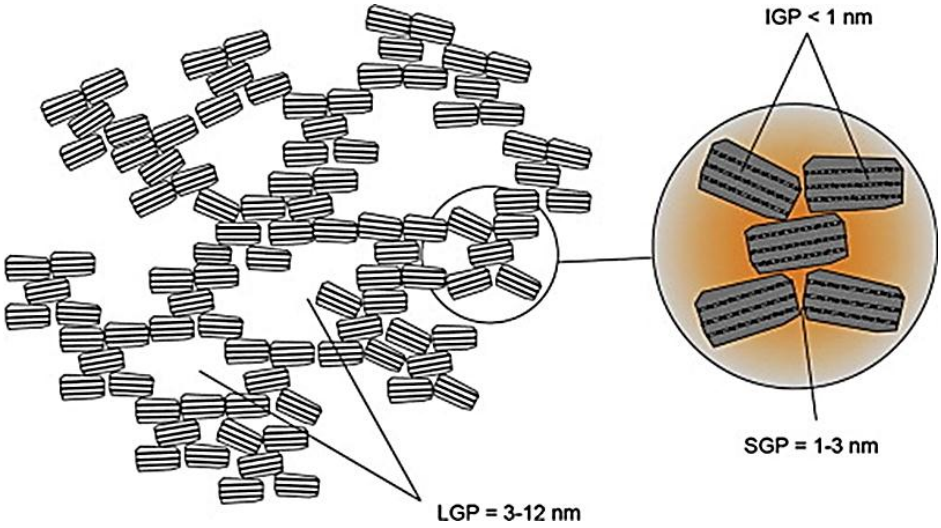

Figure 1. 7. Large gel pores (LGP), small gel pore (SGP), intraglobular pores are presented in CM-II model [56].

This model also asserts the irreversible decrease in intercrystalline porosity due to drying, temperature variations and ageing.

1.1.5. Different types of water

Water, and more generally OH groups are the source of radiolytic H_2. In hydrates like C-S-H, different types of water can be found in the C-S-H and have to be discussed because of their different contribution under irradiation (see Figure 1. 8):

- Water of crystallization: water located in the interlayer space which is not removed when heating and/or drying sample under vacuum.
- Structural water which exists as a hydroxyl groups from silanol (Si-OH) and Ca-OH in the C-S-H structure.
- Evaporable water. It can be divided into two subcategories depending on its physical state:
    - In a fully saturated pore volume, several layers of water molecules are adsorbed on the pore surfaces by attractive forces. This particular state of water is called **“bound water”**. Which can be expelled from sample without alter its structure.
    - The other water molecules fall into the second subcategory of evaporable water called **“liquid water”**. It is located in the middle of wide enough pores (> 2 nm).

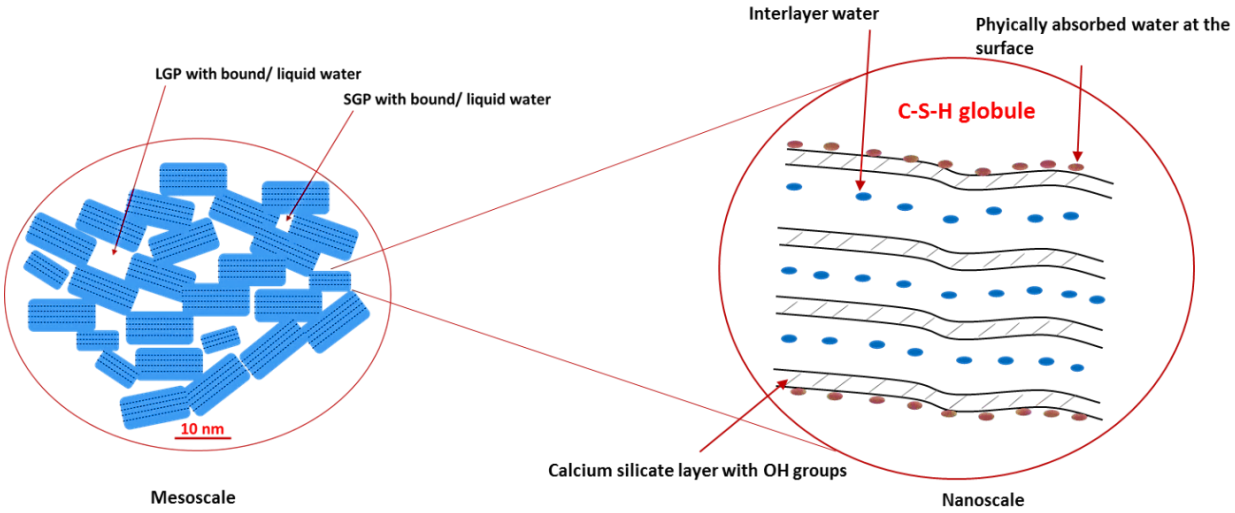

Figure 1. 8. Different forms of water in C-S-H (adapted from [56]).

1.1.6. Modification of C-S-H with the C/S ratio

In addition to the structural variations observed previously (see chapter 1.1.1.2 and 1.1.3), the C/S ratio also affects the interlayer distance and the pH of the equilibrium solution (Figure 1. 9 and Figure 1. 10) [57][120]. The distance between two calcium planes decreases with increasing C/S ratio. This is highlighted with XRD analyses by the shift of the position of the lowest angles peak with the C/S ratio from 14 Å at C/S = 0.8 to 12 Å at C/S = 1.2. The distance between two calcium planes is decreasing brutally when the C/S ratio reach the 1.0 value. On the contrary, the pH increases with the increase of the C/S ratio. The transition of two types of C-S-H phases takes place in both cases around the C/S ratio equals to 1.

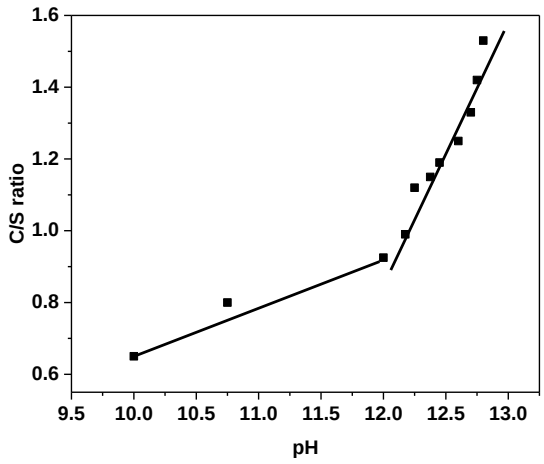

Figure 1. 9. Curve of the C/S ratio of the hydrate versus the pH of the hydration solution [57].

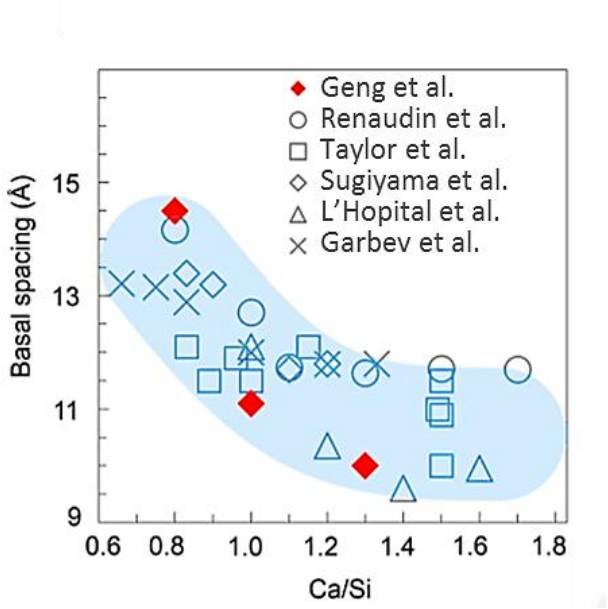

Figure 1. 10. Variation of the distance between two calcium plans with the C/S ratio [120].

1.1.7. Uptake in C-S-H

One of the interests of cementitious materials is that hydrates and in particular C-S-H are very flexible materials which can incorporate several species provided by the clinker, supplementary cementitious materials (SCMs) or radionuclide in case of conditioning applications, as for instance:

- Radionuclide: ^{90}Sr substitutes the Ca^{2+} ions in C-S-H [58]. Cs retention was found to decrease with increasing SiO_2:CaO ratio [59]. Iwaida et al. [60] observed a shortening of the silicate chains in C-S-H which had sorbed Cs, indicating breakage of the silicate chains had occurred.
- Aluminate, as a replacement of silicate in the chain.
- Alkali: as a substitution of a proton charge balancing the silanol group [61-63] or a calcium ion (Ca^{2+}) in the interlayer [62,63], or (iii) by filling an empty site in the interlayer [63].

These incorporations lead to a modification of their structure and can also affect hydration kinetics, hydrated phase assemblage, pore solution chemistry and early-age properties of cements [64].

1.1.8. Carbonation of C-S-H

It is necessary to notice that the carbonation of C-S-H may happen during long storage time. In storage environment, the C-S-H react with CO_2 or CO_3^{2-} ions in order to form different polymorph of $CaCO_3$. Wet or moist materials are especially susceptible to be attacked, but dry ones are not immune [65]. Four polymorphs of calcium carbonate exist with increasing stability: amorphous calcium carbonate, vaterite, aragonite, and calcite [65].

Grove et al. [66] studies the changes of hydrated C_3S pastes in a CO_2 environment. XRD results indicate calcite was the most dominant polymorph of calcium carbonate, with some vaterite.

1.1.9. Conclusion

This first part gives a quick overview of Portland cement chemistry with a specific focus on the composition and the structure of Calcium silicate hydrates (C-S-H). As the main hydrate of Portland cement, we assume that the improvement of the understanding of the behaviour of C-S-H under irradiation is of great interest: the structure of the hydrate, the nature of the water engaged and the composition of C-S-H can be easily modified and consequently change radiolytic gas production.

1.2. Interaction of radiations with matter

In the context of nuclear industry, it is important to control the two main effects of irradiation on cementitious materials: on the one hand, the release of H_2 issued from the radiolysis of the water which can lead to reach the flammability threshold. On the other hand, structural modifications (crystal structure, porosity, dehydration), which can alter the mechanical properties of the materials. But in our study, we only focus on the H_2 production.

In this part, a general review of radiation interaction with matter will be presented. Then, it gives an overview of the parameters influencing the production of gas under irradiation and radiolysis data in analogous materials available in the literature in connection with our study.

1.2.1. Type of radiation

Radiation chemistry is a subject that deals with the chemical changes induced by high energy radiation. The radiations usually used in radiation chemical studies are high energy photon (X−rays, γ rays) or charged particles (electrons, α particles, heavy ions etc) [67]. All these particles can cause the ionizing of the medium in which they are absorbed, so they are also often named “ionizing radiation. Ionization means the removal of electrons from atoms of the medium. In order to remove an electron from an atom, a certain amount of energy must be transferred to the atom. According to the law of conservation of energy, this amount of energy is equal to the decrease in kinetic energy of the particle that causes ionization. (Figure 1. 11).

The most basic difference between photochemistry and radiation chemistry is that in the former the energy is lost selectively to a chosen molecule, while in the latter the energy is lost to each component in proportion to its electron density.

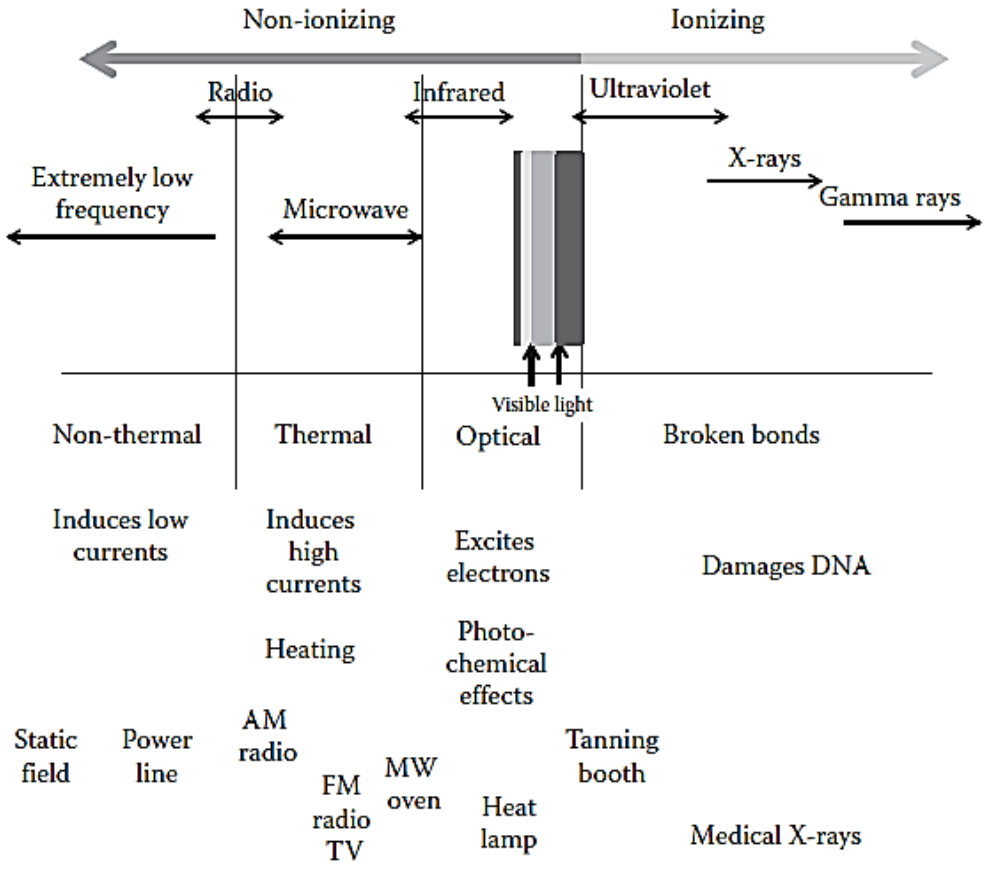

Figure 1. 11. Ionizing and non-ionizing radiations [67].

1.2.2. Direct ionizing radiation and indirect ionizing radiation

The direct ionizing radiation is composed of high-energy charged particles, which ionize atoms of the material due to Coulomb interaction with their electrons. Such particles are, e.g., high-energy electrons and positrons (β-radiation), high-energy ^{4}He nuclei (α-radiation), and various other nuclei, e.g., accelerated ions (ion beams).

Indirectly ionizing radiation is composed of neutral particles that do not directly ionize atoms or do that very infrequently, but due to interactions of those particles with matter, high-energy free charged particles are occasionally emitted. The latter particles directly ionize atoms of the medium. Examples of indirectly ionizing radiation are high-energy photons (vacuum ultraviolet, X-ray, and gamma radiation) and neutrons of any energy (neutrons are special and interact only with nuclei to emit protons).

1.2.3. Types of interactions with matter

In the initial interaction of an incident particle with any molecules, there is an inelastic collision, where the kinetic energy of the particle is completely or partially transferred into the molecules. The way of radiation energy given to a molecule depends predominantly on the type of radiation [68].

1.2.3.1. Interaction of photons (X-rays, γ rays, Extreme UV) with matter

Photons are electromagnetic radiation with zero mass, zero charge, and a velocity that is always c, the speed of light. Because they are electrically neutral, they do not steadily lose energy via Coulomb interactions with atomic electrons, unlike charged particles. There are three energy loss mechanisms by photons interaction with matter.

(1) Photoelectric effect (at photon energy < 0.1 MeV). In this case, one electron from an inner shell is ejected when it collides with a photon (Figure 1. 12).

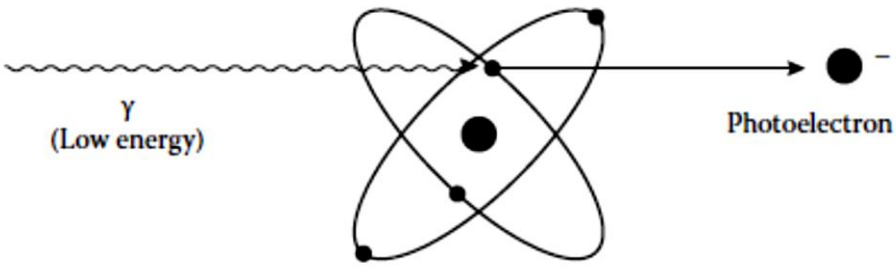

Figure 1. 12. Photoelectric effect [68].

(2) Compton scattering (at 0.1 MeV > photon energy > 1 MeV). The photon collides with an electron and gives up part of its energy to the electron (Figure 1. 13).

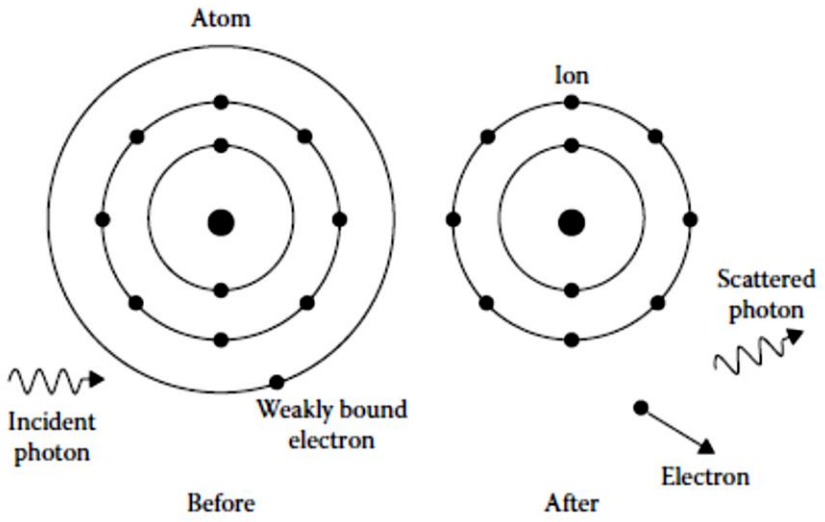

Figure 1. 13. Compton scattering by a weakly bound electron [68].

(3) Pair production (at photon energy > 1 MeV). It produces an electron and a positron (Figure 1. 14).

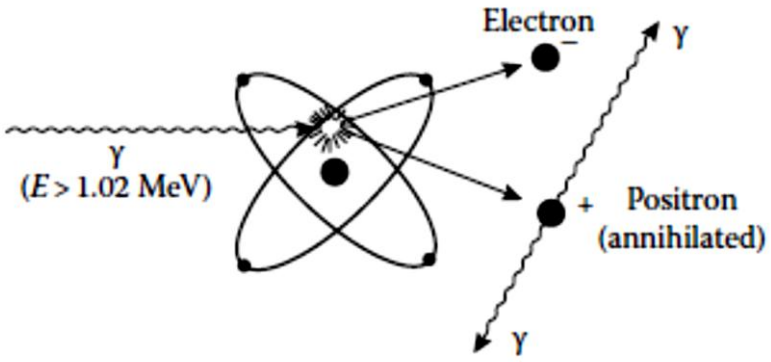

Figure 1. 14. Electron-positron pair production [68].

With increase in photon energy (Figure 1. 15), the dominant interaction changes from photoelectric to Compton to pair production. For ^{60}Co ɣ-rays, almost the entire interaction is induced by the Compton effect [67], producing electrons of 1 MeV energy and below.

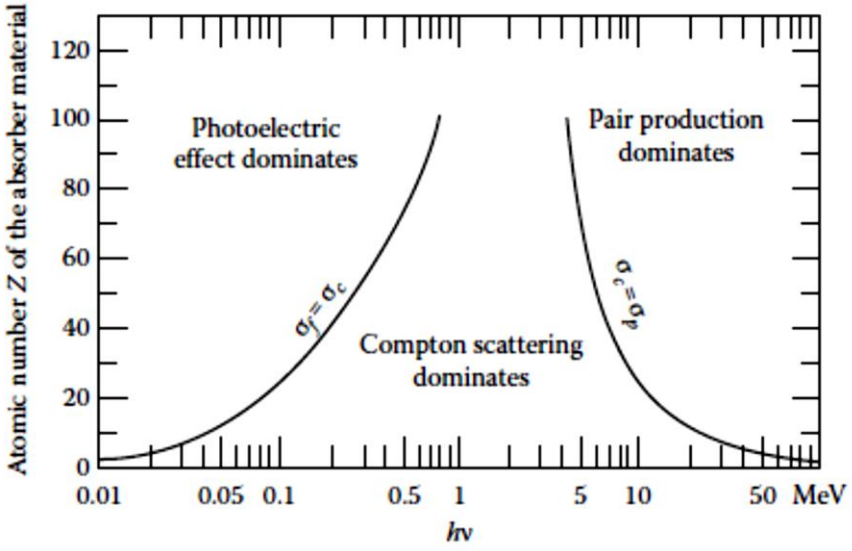

Figure 1. 15. The relative importance of various process of gamma radiation interaction with matter [68].

1.2.3.2. Interaction of charged particles (electron, heavy ions, α particles) with matter

The basic mechanism for the slowing down of a moving charged particle is Coulombic interactions between the particle and electrons in the medium. Electrons lose energy by exciting and ionizing atoms along trajectory.

However, heavy particles may act also in the medium through ballistic (or nuclear) collisions when their energy is low or intermediate. A nuclear collision occurs when heavy charged particles interact with atomic nuclei. The putative role of this regime in our experiments will be discussed later.

1.2.4. Definition of LET

An important factor that distinguishes different radiation types from one another is the linear energy transfer (LET), which is the rate at which the radiation loses energy with distance travelled through the absorber.

It describes how much energy an ionizing particle transfers to the material transverse per unit distance. Therefore, it is also called stopping power. The unit is keV.µm^{-1}. In mathematic formula (Bethe Block), it is defined as [69]:

$$LET = -(\frac{dE}{dx}) \quad (1)$$

$$-\left(\frac{dE}{dx}\right) = \frac{4\,\pi\,z^2\,e^4\,n\,N}{m\,{v_i}^2}\,ln(\frac{2\,m\,v_i^2}{I}) \quad (2)$$

z = atomic number of the heavy particle,

e = magnitude of the electron charge,

n = number of electrons per unit volume in the medium,

m = electron rest mass,

c = speed of light in vacuum,

v_i = speed of the incident particle,

I = mean excitation energy of the medium.

The stopping power is proportional to z^2. It increases rapidly at low energies, reaches a maximum and decreases gradually with increasing energy. Low LET species are usually low mass, either photons or electron mass species (β particles, positrons) and interact sparsely along their path through the absorber, leading to isolated regions of reactive radical species. High LET species are usually greater in mass than one electron, for example α particles, and lose energy rapidly resulting in a cluster of ionization events in close proximity to one another. Consequently, the heavy particle travels a relatively short distance from its origin and due to the dense geometry of track formed by radiation, the initial spurs reaction become much fast and probability of recombination reactions of each species is accelerated to be higher.

The LET increases in the following order:

y-rays and high energy electrons < protons < deuterons < α particles < heavy ions (see Table 3)

Table 3. Linear energy transfer (LET) in water for different types of radiation [69].

Rays	**LET (keV/µm)**
Gamma (photons) 1 MeV	0.23
Gamma (photons) 100 keV	0.70
Beta (electrons) 1 MeV	0.23
Beta (electrons) 100 keV	0.70
Fast neutrons 2.5 MeV	40
Alpha (helium nucleus) 5 MeV	136

1.2.5. Definition of Radiolytic yield

Radiolytic yields present the results of quantitative research on the chemical effects of ionizing radiation. The formula is as followed:

$$G = \frac{Number\ of\ species\ formed\ or\ disppeared}{100\ eV\ absorbed} \quad (3)$$

The commonly used unit of radiolytic yield is mol.J^{-1}, and in the early literature the unit is molecules /100 eV. They could be transferred into each other by:

$$1\ molecule\ (100\ eV)^{-1} = 1.036 \times 10^{-7}\ mol.J^{-1} \quad (4)$$

1.2.6. Elastic or inelastic collisions

In practice, for some given irradiation conditions, it is important to determine what is the main process that is responsible for defects creation. Then the ratio of the number of defects created by inelastic collisions $N_{inelas.}$ to the number of atoms displace d by elastic collisions $N_{elas.}$ can be evaluated:

$$\frac{N_{inelas.}}{N_{elas.}} = \frac{10^9 \cdot \left(-\frac{dE}{dx}\right)_{inelas.} \cdot e \cdot G}{N_0 \cdot \sigma_d} \quad (5)$$

Where $(-\frac{dE}{dx})_{inelas}$ is the stopping power for inelastic collisions (unity: MeV.cm^2.g^{-1}), G is the yield of formation of defects and N_0 is the number of atoms/cm^2 and σ_d defect formation cross section cm^2.

It is estimated that if electron energy exceeded 1 MeV and G exceeds 10^{-10} mol/J, the dominating process of defect creation is inelastic collisions (i.e radiolysis of the material) [70].

1.2.7. Radiolysis of Water

1.2.7.1. Liquid water

The radiolysis of water has been studied extensively since the beginning of radiation chemistry. In this section, the radiolysis of liquid water phenomena is described, which may help us to understand the radiolysis of different types of water. The value of radiolytic yield of H_2 formed in liquid water is a reference for us to compare with our future results.

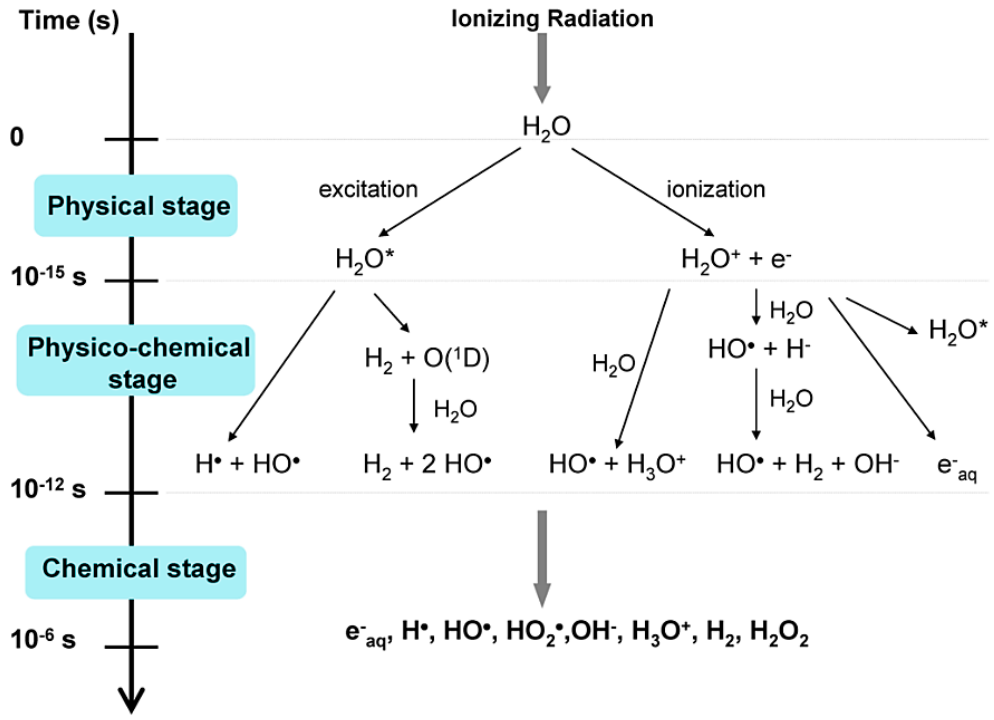

Figure 1. 16. Main reactions occur in the three stages of water radiolysis [71] [72].

Typically, water radiolysis follows two main stages: the non-homogenous and homogenous stages. The non-homogenous stages contains three steps depending on the time scales [71][72]: the physical step, the physico-chemical step and the chemical step. (see Figure 1. 16).

(1) In the physical step, the initial event is the transfer of a sufficient energy in order to excite and ionize water molecules:

$$H_2O \xrightarrow[Ionizing\ radiation]{} H_2O^{+^\circ} + e^- \quad (6)$$

$$H_2O \xrightarrow[Ionizing\ radiation]{} H_2O^* \quad (7)$$

(2) In the physico-chemical step (10^{-15} - 10^{-12}), these first three initial species ($H_2O^{+\circ}$, e^-, H_2O^*) begin to diffuse in the medium and eventually react with each other.

The excited and ionized molecules relax by dissociative relaxation:

$$H_2O^* \rightarrow HO° + H° \quad (8)$$

Or according to an ion-molecule reaction:

$$H_2O^{+\circ} + H_2O \rightarrow H_3O^+ + HO° \quad (9)$$

After H_2O ionization, two events can take place: the recombination of electron-hole or the electron thermalization:

$$e^- \rightarrow e_{hyd}{}^- \quad (10)$$

In chemical stage (10^{-12} - 10^{-6}), the species, produced in the spurs, begin to diffuse randomly by reacting with each other in the regions of high local concentrations. However, some of these species escape from the reactions in the tracks and become homogeneously distributed in the medium. The escaped species can react with each other or alternatively with the solute.

Finally, water radiolysis can be written as follows:

$$H_2O \xrightarrow[Ionizing\ radiation]{} e_{aq}^-, HO°, H°, HO_2°, H_3O^+, OH^-, H_2O_2, H_2 \quad (11)$$

It is important to point out that the dioxygen O_2 is not a primary species in the radiolysis of water.

According to the time stages, the radiolytic yield is often classified as three type:

(1) Initial radiolytic yield, which is noted as G°(X). This radiolytic yield refers to the yield of ions or excited states (X) in the end of physicochemical stage ~ 10^{-12} s. It is very difficult to measure directly this value.

(2) Primary radiolytic yield which is noted as g(X). g(X) corresponds to the transient species, radicals or molecules measured at the time when the homogenous distribution is achieved ~ 10^{-7} s after the passage of ionizing radiation. The value of g(X) is normally lower than G°(X) due to the spurs reactions.

(3) Global or apparent radiolytic yield which is noted as G(X). This yield represent some stable molecules which is measured using steady state method at relative longer time.

In our study, only the global radiolytic yields are considered.

1.2.7.2. pH effect on G values

However, the escape yields (see Table 4) depend on several parameters, such as LET of the radiation and the pH (see Figure 1. 17) [73][75].

Table 4. H_2 radiolytic yields obtained as a function of the type of radiation and the pH. Gamma radiation and accelerated electrons have a LET value of 0.2-0.3 keV/ µm, whereas in the case of 5 MeV alpha particles, the LET value is 130 keV/ µm [74,75].

Radiations	**$G(H_2) \times 10^{-6}$ (mol/J)**
Gamma electrons (0.1-10 MeV) pH = 3-11	0.045
Gamma electrons (0.1-10 MeV) pH = 0.5	0.041
5 MeV Alpha particles (LET=130 keV/µm) pH = 13	0.104

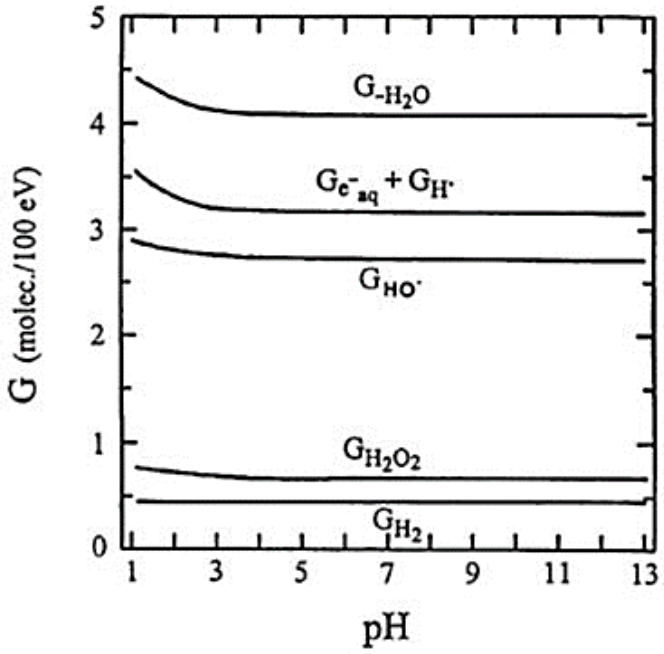

Figure 1. 17. Dependence of (primary radical and molecular yields) RMY in the ^{60}Co y-irradiation of water on pH in the range 1.3 to 13. The accuracy of the yields was estimated to be 3%.

1.2.7.3. LET effects on G values

The radiolytic yields of the molecular products (H_2 and H_2O_2) increase with LET while those of the radicals (e^-_{aq}, H°, HO°) decrease as a result of an increase of the density of ionizations in the tracks. Thus, radicals recombine more efficiently with high LET particles (Intratrack radical processes becoming increasingly important) favoring the formation of molecular species [73].

Continuous irradiation by low-LET radiation is known to lead to very low steady-state concentrations of dihydrogen and hydrogen peroxide (and the values presented in Table 4 are maximum values) whereas high LET radiation can form significant amounts of these products. The mechanism accounting for this behaviour has been proposed by Allen [76,77]. Reactions (12) and (13) make up a chain reaction in which water molecules are formed again; the rate of destruction of H_2 and H_2O_2 is equal to their production rate in water. This chain reaction is propagated by the H° atom and the HO° radical. Therefore, the higher their concentration, the more efficient their recombination.

$$HO^{\circ} + H_2 \rightarrow H_2O + H^{\circ} \quad (12)$$

$$H^{\circ} + H_2O_2 \rightarrow H_2O + HO^{\circ} \quad (13)$$

1.2.8. Irradiation in materials by types of water

C-S-H are complex material that can present different types of water. As it's well known, water, and more generally OH groups are the source of dihydrogen, each type of water has a different behaviour with respect to radiolysis:

-adsorbed water, on the surface of the spheroidal elementary bricks

-water of the hydrates

-pore water

Even if bulk water radiolysis is well known, many questions remain about the radiolysis of adsorbed and confined water.

1.2.8.1. Adsorbed water

The radiolysis of water can be strongly affected at interfaces between solid and liquid. In the case of the radiolysis of water at the interfaces between oxide and water, it was found that the type of oxide greatly impacts the H_2 production [78-82]. This is illustrated in the work of Petrik et al. [80], who studied the H_2 yield as a function of the band gap of the different oxides (see Figure 1. 18 below) submitted to γ radiation with adsorbed water molecules at their surface. The comparison between calculated yield and bulk water yield enables to sort oxides in three groups [84]:

- Oxides lowering the H_2 yield as compared to bulk water (CuO, MnO_2…);
- Oxides that do not seem to affect the H_2 yield (SiO_2, CeO_2, Al_2O_3, TiO_2…);
- Oxides increasing the H_2 yield (ZrO_2, Nd_2O_3…), hence energy transfer occurs.

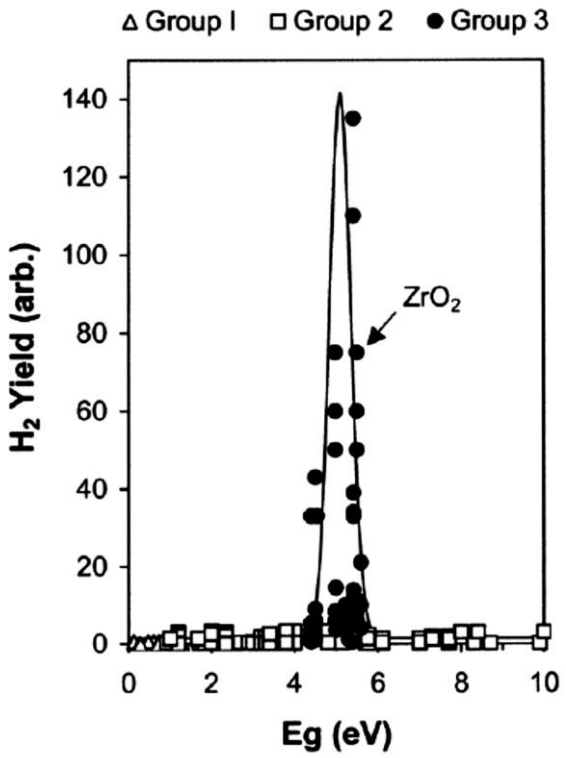

Figure 1. 18. Dihydrogen yield as a function of the oxide band gap in the γ-radiolysis of H_2O molecules absorbed on oxides. G (H_2) is calculated with respect to the energy of γ rays directly absorbed by the H_2O molecules. (Reprinted from Ref. [80])

According to Le Caër [84], many parameters related to solid can affect the dihydrogen yield at the oxide/water interface:

- The band gap of the oxide (see Figure 1. 18) [80];
- The doping of the oxide [80];
- The crystal phase [90];
- The exciton migration distance [83];
- The water adsorption form (physisorbed/chemisorbed water) [86];
- The surface density of hydroxyl groups [83][86].

The lack of studies dealing with the behaviour of cements and their hydrates under irradiation, especially C-S-H, requires finding analogue materials to be compared with.

However, recent results [15][87] suggest that hydrates, like oxides can facilitate energy transfer to adsorbed water, with energy transfer as efficient as in ZrO_2, but depending on the nanostructuration (see Table 5).

1.2.8.2. Trapped water: hydrates and hydroxides

Hydroxides contain different types of water such as free water, bond water, which is similar in the case of C-S-H. Therefore, the value of radiolytic yield of H_2 formed in water would serve as a reference to compare our results. Table 5 summarizes $G(H_2)$ in different hydroxides. H_2 formation differs with various radiation source. Some hydroxides may have a substantial H_2 releasing.

The radiolysis of nanoparticulate $Al(OH)_3$ and AlOOH under γ irradiation was studied and hydrogen production from dry samples was quantified [88]. The studies surprisingly indicate the common oxyhydroxide, boehmite, produces significant hydrogen when exposed to gamma irradiation.

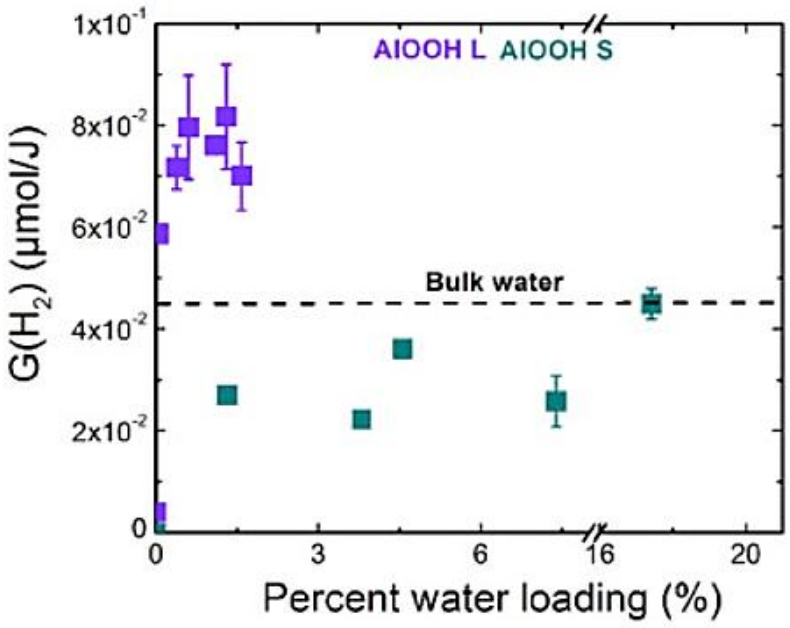

Figure 1. 19. Hydrogen production from electron-irradiated AlOOH L and S (Large particle size and small particle size are denoted AlOOH L and AlOOH S respectively) with respect to water loading. Violet squares (AlOOH L). Cyan blue squares (AlOOH S). Black dotted line: primary radiolytic yield of liquid water [89].

The radiolysis of nanosized $Al(OH)_3$ and AlOOH in dried condition has been examine using electron beams [89]. In a dry state, AlOOH L have radiolytic yields in the range of (0.05±0.02) $\times 10^{-7}$ mol/J. While, when minute amount of water is added to system (1% in mass, which represents less than one absorbed water layer), the measured yields arises to (7.6±0.2) $\times 10^{-8}$ mol.J^{-1} (see Figure 1. 19), which means that such an irradiated materials produces more efficient H_2 than an equivalent mass of water (see above adsorbed water 1.2.8.1). Figure 1. 19 shows the yields of smaller particles (AlOOH S) are lower than that of larger particles (AlOOH L), this result is quite surprising considering that smaller sizes are usually expected to favor energy transfer processes, while in materials like hydroxides, some reactive species can remain trapped in the solid network.

LaVerne et al. studied microparticulate $Ca(OH)_2$ under gamma rays and 5 MeV He ions [90]. The 5 MeV He ion radiolysis of $Ca(OH)_2$ gives a significant lower yield than observed with gamma rays, so radicals or other reactive precursors to H_2 must be recombining in the high LET helium ion track to give other products.

Compared to oxides, there is not enough data in the literature to understand how the hydrate nature, crystallite size can modify the radiolytic mechanisms.

Table 5. Molecular hydrogen radiolytic yields found in literature.

Materials	**Radiation sources**	**G(H_2) (.10^{-7}mol/J)**	**Reference**
$Al(OH)_3$†	^{60}Co Gamma rays	0	[88]
AlOOH†	^{60}Co Gamma rays	0.057-0.13	[88]
$Al(OH)_3$††	Electron beam	0.021±0.005	[91]
AlOOH L†††	Electron beam	0.05±0.02	[91]
AlOOH S†††	Electron beam	0-0.004	[91]
$Ca(OH)_2$††††	^{60}Co Gamma rays	0.21	[90]
$Ca(OH)_2$††††	He 5 MeV	0.051	[90]

†Baked at 60°C for 24 hours. Particle size 45-63 µm

††Baked at 170°C during 5 h for AlOOH

†††Baked at 130°C during 4 h for $Al(OH)_3$

††††Baked at 100°C for 24 hours. Specific surface area not specified.

1.2.8.3. Pore water in 3D network

Cements and hydrates are known to have a wide range of porosity (see Chapter 1.1.4). So, the investigation of this parameter on the gas production, which has been shown important in glasses, is difficult for cement based materials. Controlled pore water glasses (nanoporous silica glasses that can be obtained with mean pore diameters ranging from 8 to 300 nm), whose the chemical composition is the closest to cements, have shown that radiolytic phenomena that occur in water confined nanoporous silica are dramatically different from those in bulk water. For hydrated or dried glasses (see Table 6 and Table 7) irradiated using gamma rays, there is no real connection between the specific surface of material and the quantity of dihydrogen production [82]. The comparison of H_2 production by irradiation of dry and hydrated materials shows that a large part of the H_2 originates from the homolytic breaking of the silanol O-H bonds at the glass surface of the materials.

Table 6. Evolution of the dihydrogen radiolytic yield in hydrated glasses as a function of the pore size using ^{137}Cs gamma rays [82].

Pore diameter of the glass (nm)	**$G(H_2)$ ($.10^{-7}$ mol/J)**
8	1.7±0.7
25	n.d.
50	2.2±0.6
300	2.4±0.3

Table 7. Evolution of the dihydrogen radiolytic yield in dried glasses as a function of the pore size using gamma (^{137}Cs) rays. Dried materials were baked at 140°C for 1 hour and then at 500°C for 6 hours [82].

Pore diameter of the glass (nm)	**$G(H_2)$ ($.10^{-7}$ mol/J)**
8	2.2±0.1
25	n.d.
50	3.2±0.4
300	2.1±0.1

Geopolymer, an amorphous based material made of silicate (SiO_4) and aluminate (AlO_4) was recently studied for the immobilization of low and intermediate level nuclear waste [92] containing Mg-Zr alloys [93] prior to disposal. It is a mesoporous material (2-50 nm pore sizes) [94], thus having pores in ranges comparable to porous glasses. Their structure is composed of aluminate and silicate tetrahedrons polymerized where the negative charge on aluminium is balanced by extra framework alkali cations such as sodium.

In their case, the confined water was responsible for most of the gas release while the contribution from residual silanol groups was suggested to be negligible [95]. The yield normalized by the water mass was about 0.42 10^{-7} mol/J for sodium geopolymer, very near from bulk water and suggesting that the energy transfer were negligible. However, exchanging sodium for other ions like cesium increased the yields, probably by modifying the porosity in favour of small pores. As in hydrates, the connection between elementary composition, structure and H_2 production can thus be quite complex.

1.2.8.4. Pore water in 2D network

Extensive information has been collected over the last 35 years on radiation effects on clay minerals, which have a layered structure as C-S-H [96]. The investigation of several clay minerals, namely kaolinite, dickite, montmorillonite, illite and sudoite, by electron paramagnetic resonance spectroscopy has shown the presence of defects produced by natural or artificial radiations [96].

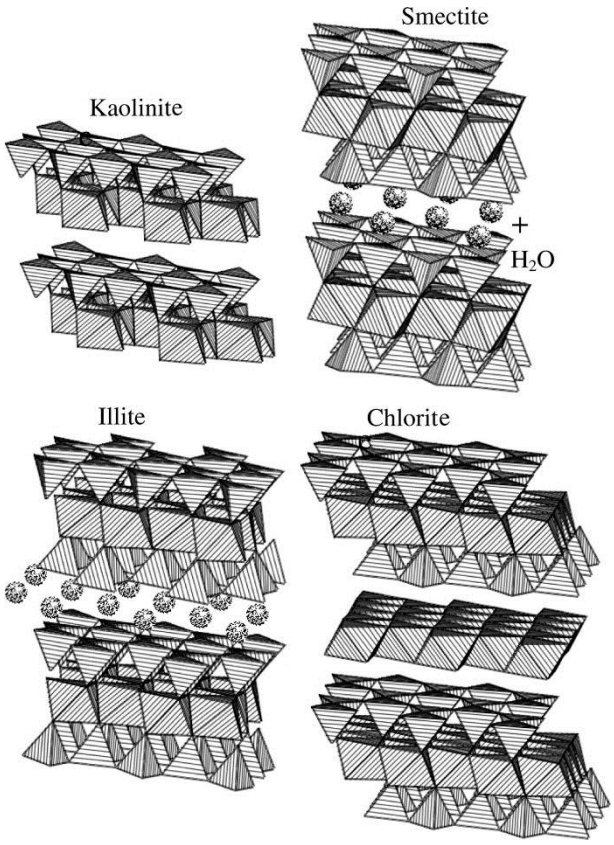

Figure 1. 20. Crystal structure of some clay minerals [96].

Clay minerals are finely-divided layered silicates encompassing various crystal structures (see Figure 1. 20). Their structure is not modified by ionizing radiations (alpha particles, beta, gamma rays) with moderate (MeV) energy, in a dose range reaching 10^9 Gy [97,98].

Recently, the study of the H_2 production of water confined in swelling clays (saponite and montmorillonites) (Figure 1. 21) [99] has shown that the H_2 radiolytic yield in the dry systems are very similar to that measured in a non-swelling clay minerals. The yied are 2-3 times higher with one water layer in the interlayer space, evidencing very efficient energy transfer and efficient recombination reactions due to a high confinement. With two water layers, the H_2 yields decrease as compared to the previous case (see Figure 1. 21), but remain higher than in bulk water, proving the recombination reactions of hydrogen atoms are less efficient.

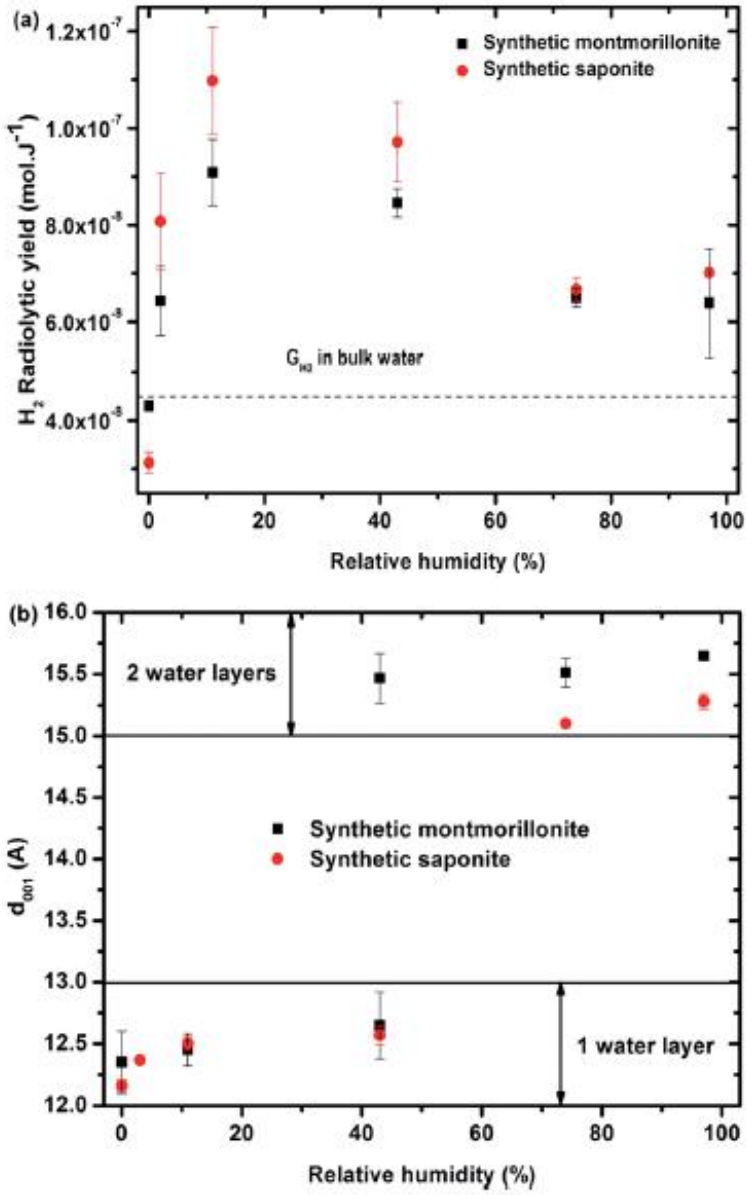

Figure 1. 21. H_2 radiolytic yields as a function of the relative humidity for synthetic montmorillonite (black square) and saponite (red circle). The value obtained in liquid bulk water is given as a comparison (4.5×10^{-8} mol.J^{-1}) to unravel the specific behaviour of confined water. (b) d001 distance as a function of the relative humidity obtained for synthetic montmorillonite (black square) and saponite (red circle). No value for montmorillonite at 3% RH is given here, as the assignment of the peaks was unlikely in this case. For the montmorillonite at 43% RH, two peaks were obtained that account for the simultaneous presence of 1 and 2 water layer(s) in the interlayer space [99].

1.2.8.5. Cement based materials

Recently, cement pastes have been studied as a function of relative humidity under electron irradiation [18]. The results showed that H_2 production in cement, the main effect of water radiolysis, depends strongly on the composition and relative humidity. First-principle calculations indicate that the water-rich interlayer regions with Ca^{2+} ions may act as electron traps that promote the formation of H_2. They also show that holes localize in water-rich regions in low Ca contents samples and are then able to participate in H_2 production. They evidence that H_2 can be produced from the chemically bound water molecules in the C-S-H interlayer pores.

Moreover, D. Chatier et al. studied cement based materials under gamma irradiation. The results (Figure 1. 22) show chemically bound water in cement hydrates (C-S-H or $Ca(OH)_2$ mostly) could produce dihydrogen as efficient as water trapped within the nanoporosity. The measured yield are typically in the order of 0.4×10^{-7} mol/J, suggesting that no energy transfer occurs in these material [23].

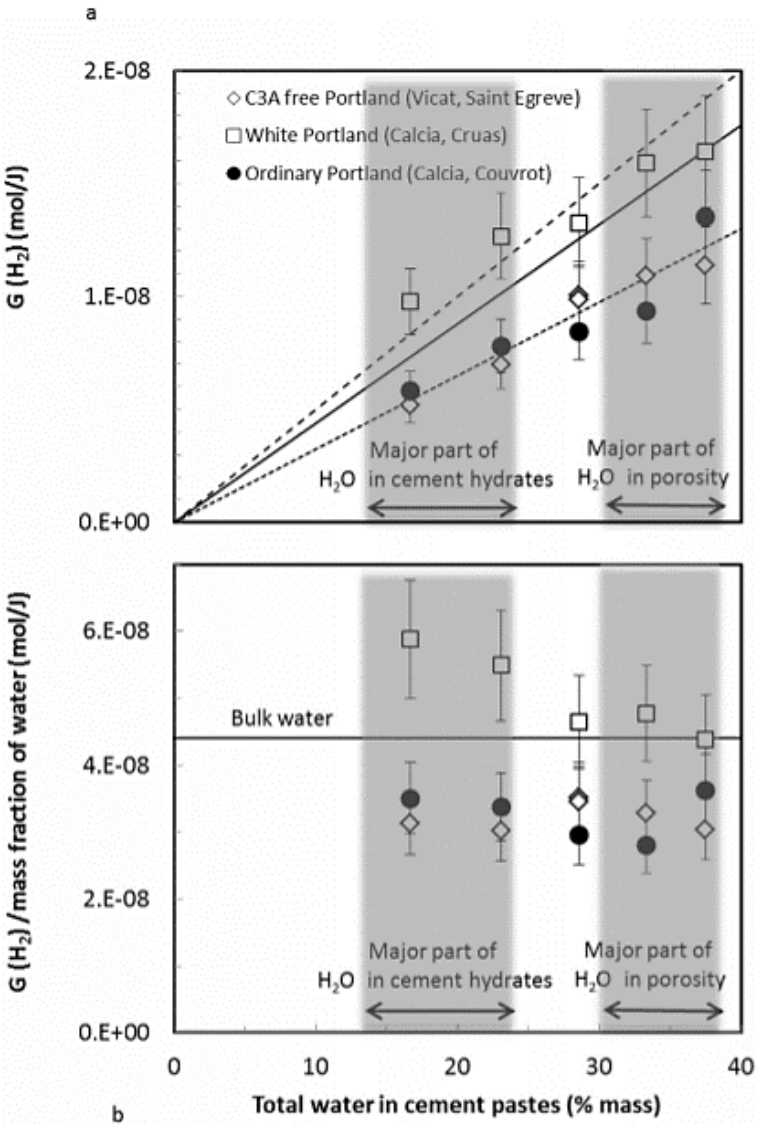

Figure 1. 22. Radiolytic hydrogen yields of Portland cement pastes as a function of the total amount of water. (Figure a: radiolytic yields of materials; Figure b: radiolytic yields normalized with regard to the amount of water of materials) [23].

1.2.8.6. Radiation induced defect (RID)

The effect of ionizing radiation on solid materials and the characterization of radiation-induced defects have been investigated more than 45 years ago. Nevertheless, there are only few studies interest us, the phenomenon on hydrates remains unexplained. Then we limited ourselves to the following materials that are close in composition to the C2S, C3S hydrates and C-S-H:

Zeolites,

Aluminosilicates glasses,

Clay minerals,

Alkaline hydroxides.

1.2.8.6.1. Zeolites

The effect of radiation on zeolites has mainly been investigated in context with radioactive waste management, where zeolite might be used as getter materials [100].

Wang et al. studied Y-type zeolite [101]. Three paramagnetic centers were formed after extensive gamma irradiation under vacuum: two were identified as V-type centers (positive-ion vacancies whose neighbors contain the same number of holes as the charge of the normal lattice ion that is missing) and the other as an F-type center (negative-ion vacancies containing the same number of electrons as the charge of the normal lattice ion, that can be described formally as a trapped electron). Verine et al. studied γ-irradiated decationated HY and HZ zeolites [102] and identified two types of V-type centers (electron hole in a p oxygen orbital) with the following structure (see Figure 1. 23):

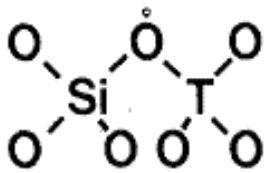

Figure 1. 23. The structure of V-type centre (electron hole in a p oxygen orbital) [102].

T is either an aluminum (V_1 center) or a silicon (V_2 center) [103].

The signal of these centers appears as a broad band center at g_{av}=2.017 (g is here the electron spin resonance g factor, not a radiolytic yield) with a broad and unresolved shoulder at g≈2.045 with a six lines hyperfine pattern (A≈0.75 mT).

After exposure to oxygen at 77 K, the signals disappear and are replaced by two new signals with the following parameters:

For HY zeolite (decationated faujasite), gzz≈2.032, gyy≈2.0015, and gxx≈1.9995 and gzz≈2.022, gyy≈ 2.0015, gxx≈ 1.9975.

For HZ zeolite (the H mordenite), gyy≈2.0005 and gxx≈1.9985 and gyy≈2.0005 and gxx≈1.9965.

The V centers can be restored by outgassing at room temperature. As a consequence the new signal is attributed to the absorption of oxygen molecules on the V centers.

Abou-Kais et al. studied γ-irradiated at liquid nitrogen temperature Mg-Y and CaY zeolites [103]. For MgY samples, they identified a classical broad signal associated to V center. Two signals (I and II) with weak intensity at g value=2.0008 were attributed to surface F-centers (electrons trapped in lattice oxygen vacancies). For CaY samples, F-centers were identified at g value=2.0004 and g value=1.9967.

1.2.8.6.2. Aluminosilicates glasses

Irradiation of alkali silicate glasses results in the formation of different kind of oxygen-related defects: oxygen hole center, silicon peroxy radicals, interstitial O_2^- ions, interstitial ozonide ions O_3^- [104,105].

Two types of oxygen hole centers (called OHC1 and OHC2) have been identified and extensively studied [106]. Figure 1. 24 presents a model representation of these centers. The spin-Hamiltonian parameters used in the simulations for these two centers are given in Table 8.

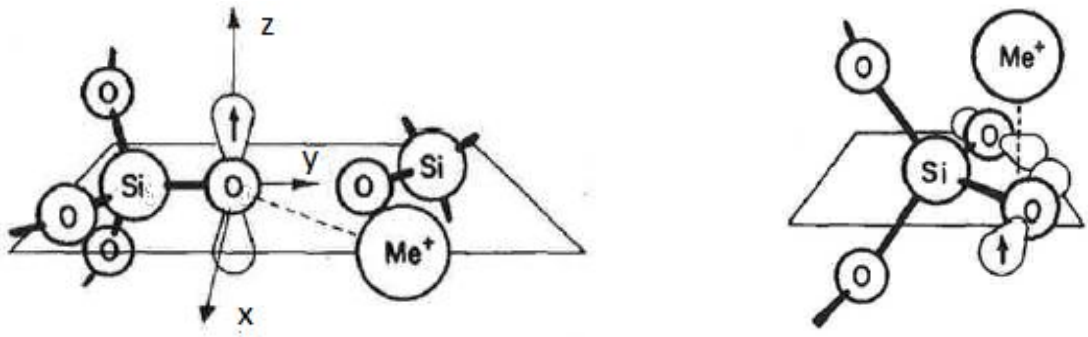

OHC1 OHC2

Figure 1. 24. Model representation of OHC1 and OHC2. The configuration of OHC2 changes with temperature. In the figure, the only low temperature configuration is presented [106].

D.A. Dutt et al. studied gamma-irradiated calcium aluminosilicates glasses at 77K [107], the defect with $<g_{zz}>$=2.072 g_{yy}=2.0087 and g_{xx}=2.0020 was attributed to an O_2^- radical.

1.2.8.6.3. Clays minerals

Clay minerals are known to contain paramagnetic defects produced by natural and artificial radiations (Ikeya 1993; Clozel et al. 1994). Some defects related to H° at low temperature (77 K) in the structure of kaolinite have been showed by [108]. They form a doublet centered at g=2.002 with a hyperfine constant around 510 gauss. A natural montmorillonite containing radiation-induced defects was studied with EPR [109]. Different defects were identified: a dominant native defect which gives rise to an orthorhombic spectrum with gx=2.004±0.005 gy=2.010±0.003 gz=2.065±0.002; another native defect 2 with isotropic spectrum at g=2.019±0.005. In addition RID were observed which are holes trapped on oxygen atoms of structure. The spin parameters of these defects are given in Table 8.

1.2.8.6.4. Alkaline hydroxides

Holuj and Wieczorek [110] studied X-ray irradiated $Ca(OH)_2$ by EPR method and identify a O^- (also called V^-) center. The spin parameters are:

gx= gy=2.0759 and gz=2.0009

In a series of papers, Barsova, Yurik et al. [111-113] presented the results they obtained on Mg, Ca, Sr, Ba hydroxides and their hydrates after irradiation. They identified:

H atoms. Three different types of H° having different hyperfine constants A_{iso} were observed.

F electron centers (in contrast to the oxides, an electron center in the hydroxides is not charged with respect to the lattice).

O^- ion-radical. The authors proposed the following reactions:

$$OH^- \rightarrow OH + e^- \quad (14)$$

$$OH^- + OH \rightarrow O^- + H_2O \quad (15)$$

$$OH^- \rightarrow O^- + H \quad (16)$$

O_2^- ion-radical

O_3^- ozinide radical

Kadissy et al. [22] studied electron irradiated $Al(OH)_3$ and AlOOH by EPR and identify H radicals, F centers, O^- and O_3^- centers.

Table 8 presents a summary of the major radiation induced defects explained above in different irradiated samples. g values are given as encountered in the literature.

However, no information is available about defects on irradiated C-S-H, therefore, the purpose of the present work is to identify the defects on irradiated C-S-H samples.

Table 8. Characteristic g-values of RID in irradiated materials.

Defects	g3	g2	g1	Material	Reference
OHC1	2.0353	2.0182	2.0023	Aluminosilicates glasses	[112]
OHC2	2.0186	2.0106	2.0025	Aluminosilicates glasses	
O_2^-	2.072	2.0087	2.0020	Calcium Aluminosilicates glasses	[106]
Native defect 1 (ND1)	2.065	2.01	2.004	Natural montmorillonite	[109]
Native defect 1 (ND2)	2.019	2.019	2.019	Natural montmorillonite	
Irradiation defect (ID1)	2.055	2.008	2.007	Natural montmorillonite	
Irradiation defect (ID2)	2.037	2.001	2.001	Natural montmorillonite	
Defect 3	2.002	2.002	2.002	Natural montmorillonite	
V centers		2.0005	1.9985	HZ zeolite	[102]
		2.0005	1.9965	HZ zeolite	
V centers	2.032	2.0015	1.9995	HY zeolite	
	2.022	2.0015	1.9975	HY zeolite	
O^-	2.0759		2.0009	$Ca(OH)_2$	[109]
O^-	2.0759		2.0019	$Ca(OH)_2$	[113]
O^-	2.0480		2.0020	$Mg(OH)_2$	
O^-	2.0754		2.0012	$Ca(OH)_2$	
O^-	2.0468		2.0036	$Ba(OH)_2.4H_2O$	
O^-	2.0810-2.0710			$Ba(OH)_2.4H_2O$	
O^-	2.024-2.015		2.003	$Ba(OH)_2.7H_2O$	
O^-	2.024-2.015		2.003	$Ba(OH)_2$	
O_2^-	2.3101	1.9719	1.9664	$Ca(OH)_2$	[114]
O_3^-	2.0170	2.0060	2.0010	$Sr(OH)_2/Sr(OH).2H_2O$	[115]
O_2^-	2.0510		2.0020	$Ba(OH)_2.4H_2O$	[116]
F centers	1.9919			$Sr(OH)_2$	[116]
F centers	1.999			$Mg(OH)_2$	[113]
F centers	1.9998			$Ca(OH)_2$	

1.2.9. Conclusion of irradiation part

From this quick review including some analogue materials to ordinary Portland cements and their hydrates, it has been shown that water content, water adsorption form, pore size, counter ions and dose can influence radiolytic hydrogen production. Then, same parameters should be investigated to understand radiolytic mechanisms in C-S-H. Finally, the electron paramagnetic resonance (EPR) spectroscopy experiments should be used to reveal the reaction mechanisms involved.

1.3. Conclusion

This bibliographic chapter aims to introduce the main concept related to the hydration of Portland cement, the composition and structure of its main hydrated phase, the Calcium silicate Hydrates (C-S-H), but also to establish the state of the art on the radiolysis of absorbed and confined water in cement based materials and their analogues.

Limited data are available on the influence of the nature of C-S-H on the hydrogen production under ionizing radiation. Hence, the objectives of this thesis are the following:

- ✓ Investigation of how the nature (water content, structure and composition) of C-S-H influence the hydrogen production under ionizing radiation.
- ✓ To study the hydrogen production of a mixture of portlandite and C-S-H.
- ✓ Improvement of the understanding of desired impurities (alkali ions or nitrates ions) effect on C-S-H.
- ✓ To characterize the radiation induced defects associated with molecular hydrogen using EPR.

The content presented in the next section is to describe the materials and techniques which were applied in this study.

CHAPTER 2: Materials and methods

Experiments were carried out on cement hydrates (C-S-H, C2S/C3S hydrates, portlandite and alkali-C-S-H) using different techniques. This section aims to describe the experimental procedures and parameters that led to the results presented. The radiation sources, radiation induced defects characterization and gas analysis are described.

2.1 Samples preparation

Different types of samples are synthetized:

- C-S-H, to study the effect of C/S ratio and water content on radiolytic molecular hydrogen production.- portlandite, C2S and C3S hydrates, to determine the effect of C-S-H and portlandite mixture on radiolytic hydrogen production.

- alkali C-S-H/ alkali-nitrate-C-S-H, to explore the effect of alkali cation/ nitrate ions uptake on the radiolytic dihydrogen gas production.

2.1.1 C-S-H

C-S-H samples were synthesized from pozzolanic reaction of amorphous silica (SiO_2, AEROSIL 380, Degussa) and quicklime, CaO, in excess of water. Reagent grade calcium carbonate ($CaCO_3$, VWR Company) was calcined at 960 °C for 24 hours to obtain calcium oxide, then it is stored in vacuum desiccator. Stoichiometric amounts of CaO and SiO_2 were mixed in order to produce C-S-H samples having C/S ratio of 0.8, 1.0, 1.2, 1.4 and 1.6. The materials were mixed with deionized water (Milli-Q, resistivity of 18 MΩ) at a water / solid mass ratio of 50 in 1 Liter high-density polyethylene (HDPE) bottles. The high water to solid ratio was used to obtain homogenous samples.

The bottles were shaken on a rotating rack for 1 month, placed at room temperature (i.e., 25°C). Once the desired time was reached, the remaining calcium and silicon ions concentrations in the solution were determined by ICP-AES (inductively coupled plasma-atomic emission spectrometry).

Table 9 presents the different C-S-H samples synthetized.

Table 9. Notations of the C-S-H samples with different C/S ratio and cured at different relative humidity (RH).

	C/S = 0.8	C/S = 1.0	C/S = 1.2	C/S = 1.4	C/S = 1.6
3% RH (using silica gel)	0.8 CSH dry	1.0 CSH dry	1.2 CSH dry	1.4 CSH dry	1.6 CSH dry
30% RH	0.8 CSH 30% RH	1.0 CSH 30% RH	1.2 CSH 30% RH	1.4 CSH 30% RH	1.6 CSH 30% RH
60% RH	0.8 CSH 60% RH	1.0 CSH 60% RH	1.2 CSH 60% RH	1.4 CSH 60% RH	1.6 CSH 60% RH
75% RH	0.8 CSH 75% RH	1.0 CSH 75% RH	1.2 CSH 75% RH	1.4 CSH 75% RH	1.6 CSH 75% RH
85% RH	0.8 CSH 85% RH	1.0 CSH 85% RH	1.2 CSH 85% RH	1.4 CSH 85% RH	1.6 CSH 85% RH

2.1.2 Alkali uptake in C-S-H

C-S-H samples with 0.8 and 1.6 C/S ratio (these C/S ratios were chosen as explained in literature review) were prepared by adding a total of 20 g of (CaO and SiO_2) to 1000 ml of Milli-Q water (water/solid = 50) in a high-density polyethylene (HDPE) bottle. The high water to solid ratio was used to obtain homogenous samples. The proportions of CaO, SiO_2 varied to obtain C-S-H with different Ca/Si ratios as indicated in Table 10. To study the alkali uptake, KNO_3, $NaNO_3$, KOH and NaOH solutions were used instead of Milli-Q water at concentrations indicated in table 10. NO_3^- is a well-known scavenger to react with solvated or presolvated electron, so OH^- is used for comparison. The bottles were shaken on a rotating rack for 5 months. The synthesis was conducted at room temperature (i.e., 25°C).

Table 10. Ca/Si ratio and alkali concentrations used to prepare C-S-H at 20°C.

Ca/Si ratio	[KOH] (mol/L)	[NaOH] (mol/L)	[KNO_3] (mol/L)	[$NaNO_3$] (mol/L)
0.8	0.01 0.05	0.01 0.05	0.01 0.05	0.01 0.05
1.6	0.01 0.05	0.01 0.05	0.01 0.05	0.01 0.05

2.1.3 C2S and C3S hydrates

Synthetic C3S and C2S hydrates were prepared by mixing the commercial powder C3S and C2S (Mineral Research Processing) with Milli-Q water (water/solid = 50) in 1 Liter high-density polyethylene (HDPE) bottle. A high water to solid ratio was used to obtain homogenous samples. The bottles were shaken on a rotating rack for 45 days in order to obtain fully hydrated materials. The synthesis was conducted at room temperature (i.e., 25°C).

2.1.4 Portlandite

Synthetic portlandite was prepared by mixing 20 g of CaO with Milli-Q water (water/solid = 50) in 1 Liter high-density polyethylene (HDPE) bottle. Previously, reagent grade calcium carbonate ($CaCO_3$, VWR Company) was calcined at 960 °C for 24 hours to obtain calcium oxide, then it was stored in vacuum desiccator. The high water to solid ratio was used to obtain homogenous samples. The synthesis was conducted at room temperature (i.e., 25°C).

2.2 Filtration and curing procedure

For each synthesis, samples were filtered using a Büchner funnel and a filter paper: 0.22 µm for C-S-H and 0.45 µm for other samples (Millipore). The filtration with 0.45 µm filter paper (Millipore) is sufficient for the filtration, so it was used for other samples to speed up filtration process. After filtering, samples were rinsed with water. It should be noted that the use of organic solvent (usually, isopropanol) to stop the hydration was not applied because of its contribution to radiolytic hydrogen production.

The use of water could imply for the further reactions, the continuous hydration process which lead to the formation of portlandite and carbonation (the samples exposure to the atmosphere during analysis). Therefore, the quantities of portlandite and calcite are necessary to be determined by TGA analysis.

Then, the solids were dried for characterizations and irradiations. The samples were freeze-dried during four days and then cured in desiccator chamber with the desired 3%, 30%, 60%, 75%, and 85% relative humidity (RH) under a nitrogen atmosphere at room temperature for 4 weeks until their weight stabilized.

The relative humidity was controlled by the following saturated salts: 3% RH with Silica gel, 30% RH with Magnesium Chloride, 60% RH with Sodium Bromide, 75% RH with Sodium Chloride and 85% RH with Potassium Chloride.

For C-S-H with alkali uptake, the cure was only made at 3% RH dessicator chamber.

For C2S and C3S hydrates, the samples were cured for 8 weeks in desiccator chamber with 30% and 85% relative humidity.

For synthetic and commercial Portlandite, the samples were cured for 8 weeks in desiccator chamber with 30% and 85% relative humidity, but only cured at 85% RH samples were used because portlandite is hardly to absorb water.

The Table 11 resumes the conditions of curing for all samples.

Table 11. Conditions of curing for samples.

RH	C-S-H	Alkali uptake C-S-H	C2S and C3S hydrates	Commercial and synthetic portlandite
0%	x	x		
30%	x		x	
60%	x			
75%	x			
85%	x		x	x

2.3 Analysis of filtrates

The analysis of filtrates was important in order to verify the complete reaction and to determine the elemental concentrations of calcium, silica in the solution then obtained the real C/S ratio in C-S-H based on the mass balance. The quantity of alkali introduced in C-S-H was determined as well.

2.3.1 ICP-AES analysis

Inductively coupled plasma atomic emission spectroscopy (ICP-AES, ICAP 6000 SERIES, Thermo Scientific) was used for the determination of the elementary concentration of calcium and silica in the filtrates. The principle of ICP-AES is described in ANNEX 1.

Each sample was acidified and diluted with 3% nitric acid with a factor 1, 10 and 100 depending on the ion concentration. Standards from 1 to 20 mg/L were used for calibration. The relative error of the measurements was about 10%.

2.3.2 Measurement of pH

The pH measurement is necessary to check if the reaction reaches the thermodynamic equilibrium. The pH of the filtrates was measured by a METTLER TOLEDO system equipped with a combination pH electrode Consort C931 for simultaneous determination of pH and temperature of the solution. The pH-meter was calibrated with a 2-points calibration with pH buffers at 9.18 and 12.56 (at 25°C). A temperature correction was automatically made on the final pH value. To minimise carbonation effects, the pH was measured immediately after filtration of the sample solutions.

2.3.3 Ion chromatography (IC)

For C-S-H with alkali uptake, the concentrations of sodium and potassium ions in the filtrates were determined with a Dionex DP ICS-3000 ion chromatograph with a dionex-CS17 column at an eluent flow rate of 1 ml / min. The eluent is MSA (methylsulfonic acid). Each sample was diluted by a factor 1, 20 or 100 depending on the ion concentration. The relative error of the measurements was $\approx$ 10%.

2.4 Characterization before irradiation

Before irradiation, samples were characterized by XRD, TGA and gas sorption techniques to check the purity, water content and specific surface area.

2.4.1 Purity

To check the purity of samples, X-Ray diffraction experiments (the principle is described in ANNEX 2) were performed on a Panalytical X'Pert Pro diffractometer (Bruker) with an X-Ray tube using a copper anticathode ($\lambda(K_{\alpha 1})$ = 1.54 Å). The diffractometer was operated at 45 kV and 40 mA. Measurements were made at a 2θ range from 5° to 70° with steps of 0.017° and a measurement time equivalent to 80 seconds per step. The detector is an X-celerator (linear detector with 120 points aligned detectors). The diffraction patterns were analysed using the Eva 21.0 software (Bruker).

2.4.2 Water quantification

Thermogravimetric analysis was performed to describe the dehydration process of C-S-H using a STA 409 PC Luxx® (Netzsch) from 25°C to 1000°C at a heating rate of 10 °C/min, with two hours at 300°C and two hours at 500°C (Figure 2. 1), in order to make sure the complete decomposition of different phases: water (ambient to 300°C), portlandite (410°C to 500°C) and calcite (550°C to 750°C). The analysis was conducted under nitrogen flux at 50 mL/min. Alumina crucibles were used and the sample weight was approximately 50 mg. Data were processed using Proteus Thermal Analysis (Netzsch). The derivative thermogravimetric (DTG) curve permits to determine the different loss of weight over the range of temperature.

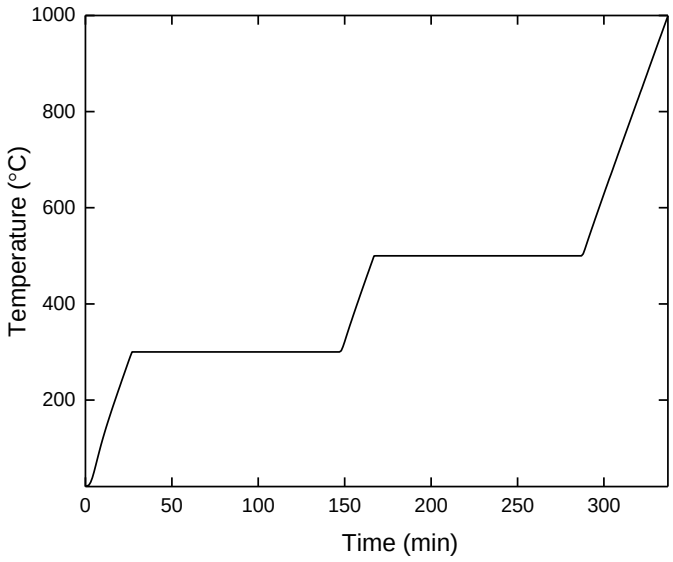

Figure 2. 1. The evolution of temperature with time.

2.4.3 Porosity and specific surface area determination

Nitrogen gas adsorption-desorption isotherms at 77K were determined using a Micromeritics ASAP 2020 surface area and porosity analyser. Freeze-dried samples were initially outgassed by using 0.3 g of each material under vacuum at 100 °C for 48 h to obtain the dry sample before analysis.

The specific surface area data were obtained after using Brunauer-Emmett-Teller (BET) [117] between 0.05 and 0.3 of relative pressure P/P_0. Linearity for the BET plot range (0.05 to 0.3 P/P_0) is verified for all tested samples in order to apply BET theory. The principle of Nitrogen gas adsorption-desorption is described in ANNEX 3.

For 1.40 CSH dry sample, the results were compared to those obtained using water vapor adsorption and desorption.

The dynamic vapor sorption apparatus used was from Surface Measurement Systems, London, UK. The RH levels at which samples (about 15 mg) were subsequently equilibrated at 25 °C included 0-2-4-8-10-15-20-25-30-40-50-60-70-75-80-85-90-95-100-95-90-85-80-75-70-60-50-40-35-30-25-20-15-12-10-8-4-2-0% RH. Wet samples underwent two desorption–adsorption cycles. For all other relative humidity steps, a time criteria of t=600 mins was applied for each step. The total measurement time was about 30 days because of the slow equilibrium kinetics. By measuring the mass change as a function of time with changing relative humidity (RH) of the sample versus an empty reference, sorption isotherms can be calculated.

The two adsorbates (N_2 and water) were used to describe the texture of solids.

2.5 Irradiation experiments

2.5.1 Gamma-rays irradiations

The samples (around 150 mg) are placed in a 10 mL glass ampoule (Figure 2. 2) and are sealed under an argon atmosphere up to 900 mbar to avoid oxygen presence. Attention has been paid to not modify the water content of the samples during the sealing which has been confirmed by TGA measurements.

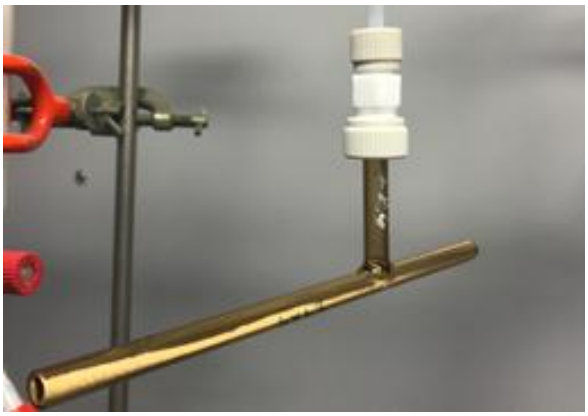

Figure 2. 2. 10ml glass ampoule after gamma irradiation.

Each sample was separated into at least two separate ampoules to verify the repeatability and validity of the measurement.

Gamma-rays irradiations were carried out at the Gammatec facility (Steris, Marcoule site, France) in the experimental irradiator equipped with a ^{60}Co source.

The radiation source was placed in the center of the irradiation chamber. It is surrounded by rails on which are mounted several rotating plates to accommodate the sample holders (Figure 2. 3). The rotation of the plates ensures the homogeneity of the absorbed dose in the samples. The temperature within the chamber was maintained between 20 and 25 °C.

Figure 2. 3. Sample holder for irradiation of ampoules.

Dosimetry was performed with red Perspex dosimeters and the absorbed dose was known with a 10 % standard deviation. The measurement of the dose rate was performed at the same place of the samples in order to take into account the screening effects between the source and the sample. In our case, the experiments were carried out with a dose rate around 600 Gy/h. We were well aware that the dose rate used was of one or two magnitudes higher than the real dose rate of the waste packages were subjected to. However, it is necessary to cumulate enough hydrogen to reach the limitation of analysis in a short time of irradiation and using a reasonable amount of sample during the thesis. Moreover, we are not interested in the degradation of materials, so we didn't go until MGy/ GGy.

In general, the absorbed doses were 100 and 200 kGy, which corresponds to one and two irradiation weeks respectively.

2.5.2 Swift Heavy ions irradiations

Heavy ion beams are used to simulate the effect of alpha particles on C-S-H. They are chosen in order to induce a LET (linear energy transfer) close to that of alpha particles emitted by alpha emitters at the Bragg peak. The ions used in these experiments were $^{36}Ar^{18+}$ at 95 MeV/nucleon (i.e. 3 GeV). The mean LET values were evaluated using SRIM/ ESTAR program [118]. The LET values were estimated to 546 keV/µm for C-S-H under 3 GeV $^{36}Ar^{18+}$ irradiation which is close to LET value of 416 keV/µm with 5 MeV α particles in C-S-H (Figure 2. 4). Besides, for sample with very thin thickness (below 1.5 mm), the LET change only slightly between the entrance and the exit of sample. As a result, the deposited dose could be estimated as homogeneous in the entire sample.

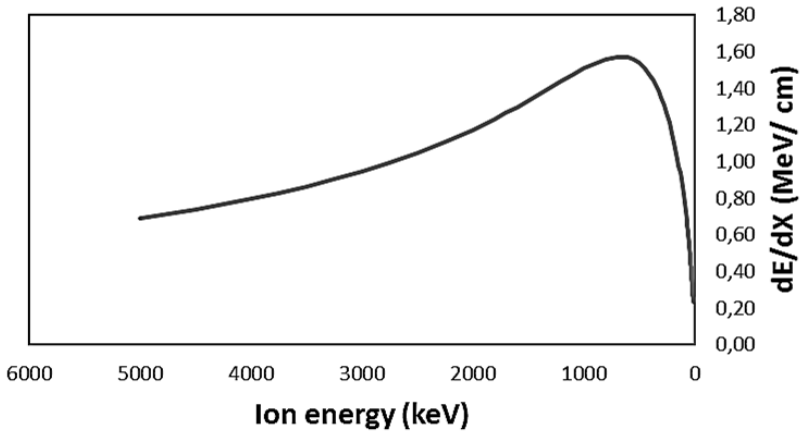

Figure 2. 4. The bragg curve of 5 MeV α particles in C-S-H.

50 mg of samples placed in thin wall Pyrex ampoules (10 mm diameter) (Figure 2. 6) were irradiated using swift heavy ions at GANIL (Grand Accélérateur National d'Ions Lourds, Caen, France) and the IRRABAT device (Figure 2. 5). During irradiation, the chamber was under vacuum and the temperature of the samples was comprised between 20 and 25°C. The samples were irradiated at two fluences: $1.14\text{-}1.31\times10^{12}$ and $2.27\text{-}2.28\times10^{12}$ ions.cm^{-2} and the flux was comprised between 2.65 and 3.68×10^{8} ions.cm^{-2}.s^{-1}. The approximate water equivalent doses corresponding to these fluences are 500 and 1000 kGy respectively.

Figure 2. 5. IRRABAT device.

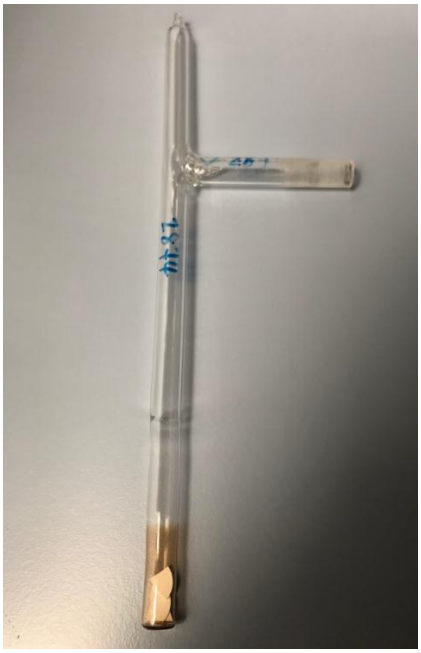

Figure 2. 6. 10ml ampoule after heavy ions irradiation.

2.5.3 The linear accelerator LINAC

The materials were irradiated with electron beam, which was intended to identify and quantify the radiation-induced defects formed under ionizing radiation.

The samples were placed in glass EPR tubes (Figure 2. 7) under argon atmosphere at 900 mbars. The mass of samples was around 20 mg. The irradiation was conducted in a sealed EPR tube to permit the irradiation of the sample with the electron beam (the surface of irradiation is 1 cm^2).

Irradiations were performed using the electron pulses of a Titan Beta, Inc. linear accelerator (Laboratoire Interdisciplinaire sur l'Organisation Nanométrique et Supramoléculaire LIONS, CEA Saclay, France). Electrons of 10 MeV with a pulse length of 10 ns were used. All experiments were done at a pulse frequency of 5 Hz, with a dose per pulse estimated to 6 Gy/pulse. Glass ampoules containing the materials were directly placed in a holder filled with liquid nitrogen in order to keep the samples at 77 K during irradiation, in front of the window from where electron beam goes out. The dose rate was estimated using Fricke dosimetry. The samples were submitted to 2500 and 5000 pulses that is correspond to an absorbed dose of about 15 and 30 kGy, respectively.

Figure 2. 7. The EPR tube for electron beam irradiation. The yellow part is kapton tape that protects the name. The external diameter of tube is 4 mm.

2.6 Gas analysis and determination of radiolytic yields

The amount of dihydrogen produced during γ-irradiation was evaluated by using a micro-gas chromatography (490 Micro-GC, Agilent) equipped with a compression system (SRA Instruments) to provide 1 bar of pressure at the input of the μ-GC injector. The channel used for hydrogen analysis contains a Molecular Sieve 5A PLOT column under argon at 28 psi pressure and a micro thermal conductivity detector (μ-TCD). The oven and detector temperatures were respectively 90 and 120 °C, with an acquisition time of 2 minutes.

The hydrogen production yield, denoted as the G-value and expressed in mol/J, corresponds to the amount of dihydrogen produced per amount of absorbed energy. For each C-S-H sample, apparent hydrogen radiolytic yields $G(H_2)$ have been assessed by calculating the slope of the hydrogen production as a function of the absorbed dose. Normalized apparent hydrogen radiolytic yields $G_{norm}(H_2)$, expressed in mol/J, were calculated by normalizing apparent hydrogen radiolytic yields by the experimentally measured initial water mass fraction. Yields standard deviations were estimated to be 15% for all samples, except for samples under heavy ions irradiation were at 20%.

2.7 Characterization after irradiation

After irradiation experiments (gamma rays and heavy ions irradiations) and gas analysis, samples were removed from the glass ampoules and characterized by XRD and TGA.

After electron beam irradiations, samples were analyzed using electron paramagnetic resonance spectroscopy (EPR) in order to detect the transient defects induced by irradiation.

2.7.1 Electron paramagnetic resonance spectrometry (EPR)

Electron paramagnetic resonance (EPR) spectroscopy (see principle in the ANNEX 4) was conducted at the Laboratoire des solides irradiés (LSI, Ecole Polytechnique, France).

Samples were transferred under nitrogen liquid in EPR tube to maintain the temperature at 77 K in order to trap radicals without using spin trapping molecules. Spectra were acquired on an EMX Bruker spectrometer (X-Band) with a 100 kHz field modulation. In most case, microwave power and amplitude modulation were 10 mW, and 1 Gauss, respectively. The microwave frequency was measured with a frequency counter.

Spectra were achieved from 100 K to room temperature at every 10 K in order to follow the evolution of the different signals and to distinguish the contributions of the different transient species which contribute to the observed signal.

From the spectra achieved, quantification of the total radiation induced defects (RID) could be estimated using a mixture of TEMPO (2,2,6,6-Tetramethyl-1-piperidinyloxy, free radical, 2,2,6,6-Tetramethylpiperidine 1-oxyl)(Figure 2. 8) and 1.4 C-S-H dry sample as a standard.

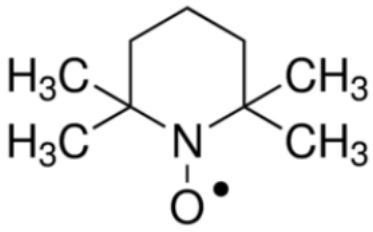

Figure 2. 8. The formula of TEMPO

Here, the weight of TEMPO introduced was equal to 0.21 mg that corresponds to a quantity of free radicals of 8.17×10^{17} molecules.

The integration of TEMPO signal issued from the spectrum analyzed at the same temperature than our spectra (at 100 K) corresponds to a quantity of free radicals N_0 of 8.17×10^{17} molecules / g of sample.

As the intensity of integrated signal I_0 was proportional to the radical quantity, the quantification was possible if the same EPR parameters were remained.

The number of RID (N) should be determined by normalizing the signal by the weight of the sample and using the formula:

$$N\,(molecules/g) = \frac{I_{measured}}{I_0} \times N_0 \qquad (17)$$

With, I measured, the intensity of the area measured after integration of the EPR signal,

I_0, the intensity of the area measured after integration of the EPR signal of TEMPO sample,

N_0, the quantity of free radicals measured in TEMPO sample, expressed in molecules/g.

The error on the quantification was estimated at 25%.

From the quantification, a radiolytic yield of radical formation could be estimated using the absorbed dose by the sample.

$$G = \frac{N}{D} \tag{18}$$

with G, the radiolytic yield of RID, expressed in mol/J,

N, the quantity of RID in mol/kg,

and D, the absorbed dose in Gy.

2.8 Other characterizations

Different characterizations were performed in order to provide supplementary information about the microstructural features (e.g., particle size, shape and specific surface area) using (transmission electron microscopy) TEM and (small/ wide angle scattering) SAXS/ WAXS.

2.8.1 Transmission electron microscopy

The morphology of C-S-H was studied with transmission electron microscopy. Images were obtained using a transmission electron microscope (JEOL JEM 2011 TEM), at Centre Interdisciplinaire de Nanoscience de Marseille, Aix-Marseille Université, France. Sample were dispersed by ultra-sound in the “white spirit” solvent; a drop of the dispersed samples was deposited over a Holey copper grid. The solvent was chosen in order to avoid using water where carbonation could occur.

2.8.2 Wide and Small-Angle X-Ray Scattering (WAXS/ SAXS)

X-rays was used to investigate the structural properties (the number of stacking, the length of particle and the specific surface area) of C-S-H. Photons interact with electrons, and provide information about the fluctuations of electronic densities in C-S-H. A typical experimental set-up was shown on Figure 2. 9. The principle of SAXS was described in ANNEX 5.

The WAXS measurements were carried out at the Marcoule Institute for Separation chemistry (ICSM). The parameters used are: X-ray wavelength at 1.033 0.71 Å, energy of the beam at 17 keV, beam size equal to 700 × 700 µm.

For some samples, complementary SAXS experiments were carried out at the SWING beamline at the SOLEIL Synchrotron source (SOLEIL Synchrotron, Saint-Aubin, Gif-sur-Yvette Cedex, France). The X-ray wavelength used was 1.033 Å. This equipment allows for recording information within the $4.4\times10^{-3} < q < 3.6\times10^{-1}$ $Å^{-1}$ wave vector range. The energy of the beam was 12 keV and the detector to sample distance was 3 m. The C-S-H powder were placed in a capillary of 2 mm.

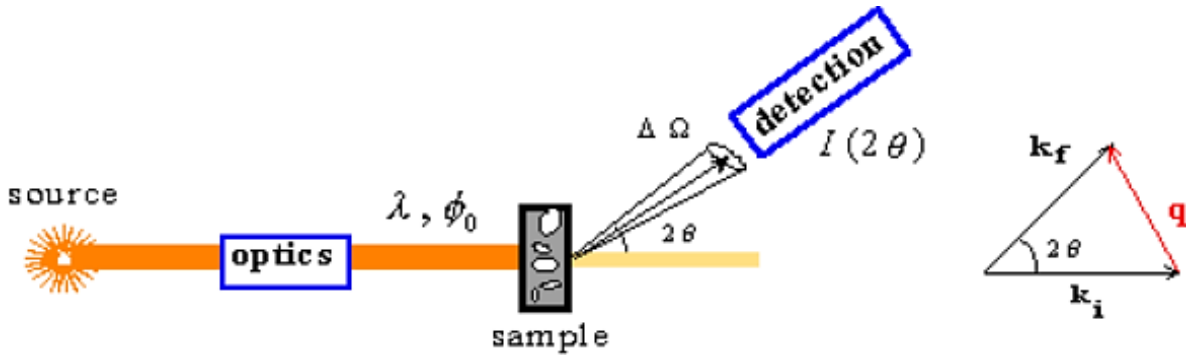

Figure 2. 9. Schematic view of a typical scattering experiment.

CHAPTER 3: Molecular hydrogen production from C-S-H

This section presents results related to the radiolytic hydrogen production from C-S-H. In order to study the influence of the microstructure and the water content of C-S-H on the radiolytic hydrogen production, samples with different C/S ratio and different relative humidity were synthetized. All samples are characterized to ensure the composition of the samples, their water content and their porous network. Then, samples were irradiated with gamma-rays and swift heavy ions in order to specify the radiolytic yields of hydrogen production. Finally, samples irradiated with electron beam were analysed using EPR spectroscopy to identify radiolytic induced defaults (RID) and the associated yields.

3.1. Characterization

3.1.1. Sample chemical composition

The experimental C/S ratios are determined from the chemical composition and the pH of the solutions at the end of the shaking time. The plot of pH of solutions versus the theoretical C/S ratio are presented in Figure 3. 1. The calculated concentrations of CaO and SiO_2 are deduced indirectly from the concentrations of Si and Ca in solutions determined by ICP-AES and are presented in Table 12.

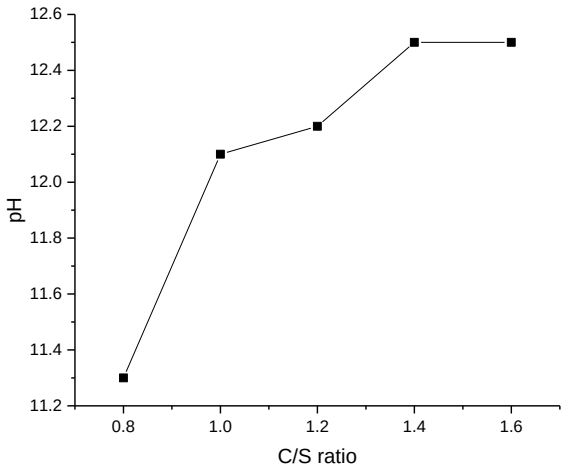

Figure 3. 1. pH values of solutions versus theoretical C/S ratio for the synthesis of C-S-H.

Table 12. pH values and CaO and SiO_2 concentrations of C-S-H synthetic solutions.

Theoretical C/S ratio	0.8	1.0	1.2	1.4	1.6
pH value of the solution	11.3	12.1	12.2	12.5	12.5
[CaO] in the solid (mmol/L)	152	167	180	188	187
[SiO_2] in the solid (mmol/L)	190	172	157	144	134
Experimental C/S ratio	0.80	0.97	1.14	1.30	1.40

Measurement error: aqueous silicon, calcium and concentrations ±10%; pH ±0.1unit.

According to the solubility curve which has been shown in the literature review chapter 1.1.1.1, the samples can be considered at equilibrium state.

3.1.2. The purity of C-S-H samples

The purity of C-S-H samples was controlled by X-Ray powder Diffraction (XRD). The experimental patterns show that all the samples with different RH present the diffraction peaks corresponding to the tobermorite structure [35][37][40][51]. Figure 3. 2 shows the samples cured at 60% RH with C/S ratio from 0.80 to 1.40, as an example. For nominal C/S ratio from 0.80 to 1.14, the diffractograms do not reveal other peaks. Then, the pozzolanic reaction is complete and the C-S-H are considered pure, but it may contain unreacted silica fume. It is noticed that, for samples with C/S ratio at 1.30 and 1.40, additional peaks appear that are attributed to small amount of portlandite and calcite. The presence of portlandite and calcite are quantified by TGA analysis in the following part (see Quantification of water and impurities section).

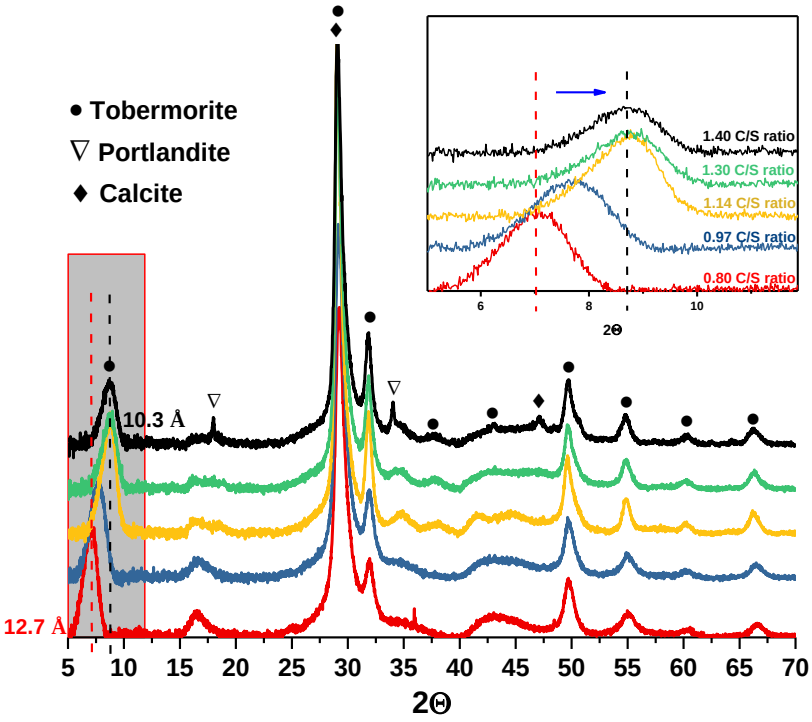

Figure 3. 2. Powder XRD patterns of the different C-S-H samples (From bottom to top: 0.80, 0.97, 1.14, 1.30 and 1.40 CSH RH=60%).

The main differences between the various XRD patterns of C-S-H with different C/S ratio acquired at a 60% RH are the position and the intensity of the peak at 7.2−9.1° and 30° (2θ). The position of the first peak corresponds to the (001) reflection and reveals the interlayer distance using the structural model described by [35][37][40][51]. The Figure 3. 3 indicates the evolution of the interlayer space in function of C/S ratio for samples stored under different RH%. For samples stored at 60% RH, at C/S ratio of 1.40, 1.30, 1.14, 0.97 and 0.80 ratio, the (001) reflection evolves from 10±0.5 to 13±0.5 Å, which is in good agreement with previous study [57][120]. Noticingly, the interlayer distance varies very little between C/S of 1.1 and 1.4 that is in good consistence with previous study [57][120].

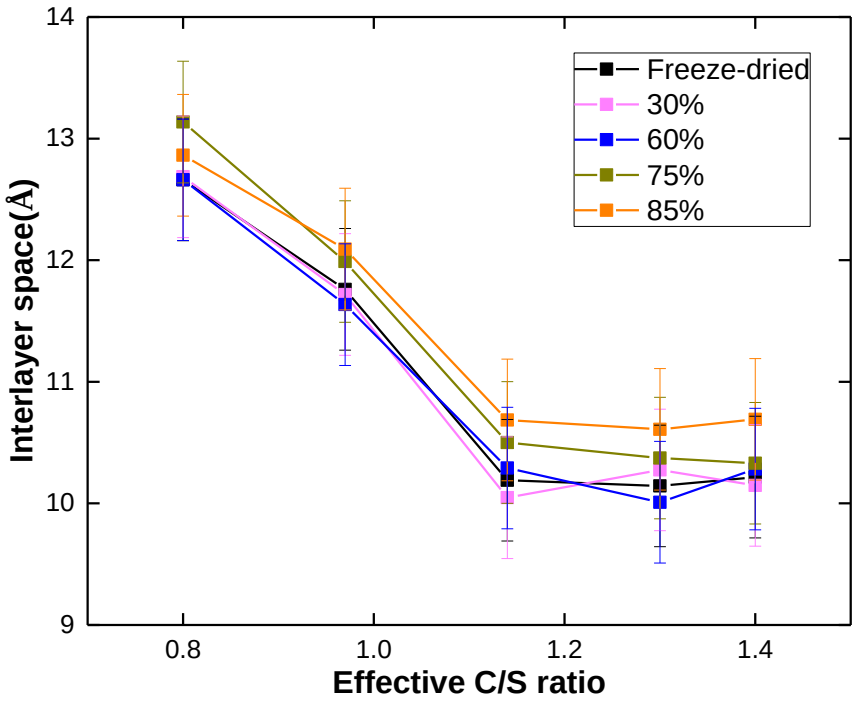

Figure 3. 3. Interlayer space of C-S-H samples deduced from XRD patterns as a function of the C/S ratio at different RH. The error on the d001 value is estimated at 0.5 Å.

Quantification of water and impurities

The thermograms (TG) and their first derivative (DTG) are shown in Figure 3. 4. All the TGA analyses showed similar curves, therefore, only results at RH 60% were presented in this figure. Three steps of decomposition are observed. The first one, from 30 to 300°C, corresponds to the loss of the sum of pore water, crystallization water and hydroxides [122].

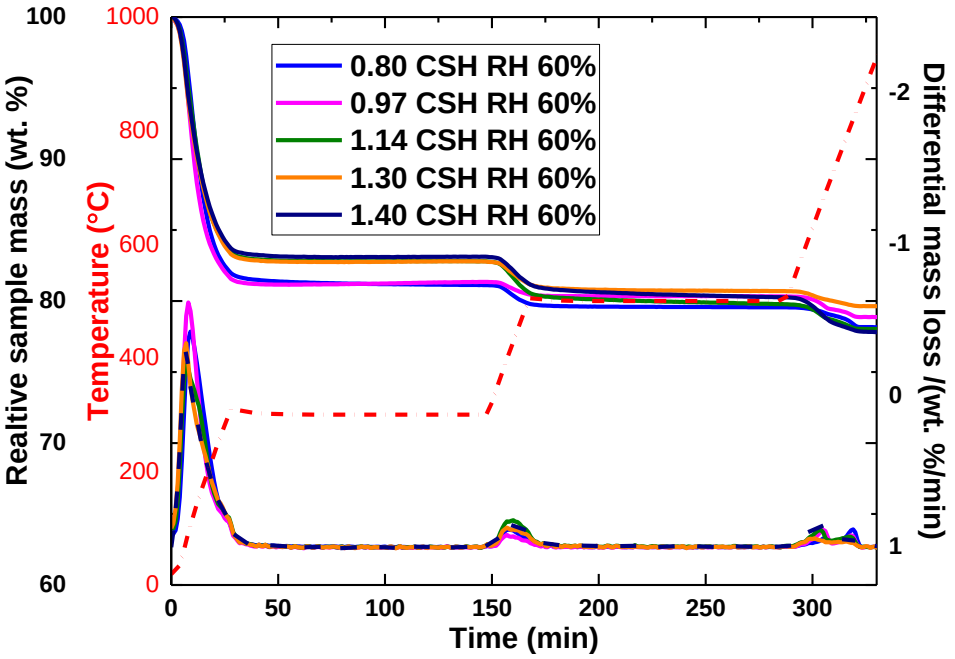

Figure 3. 4. TG (solid line) and DTG (dash line) curves of 0.80, 0.97, 1.14, 1.30 and 1.40 C/S ratio CSH samples at RH 60%. DTG curves are given to illustrate the water loss and the detection of minor phases such as portlandite and calcium carbonate.

The second step, from 410 to 500°C, corresponds to the decomposition of few amounts of portlandite ($Ca(OH)_2$) [123]. In the third step, the weight loss from 550 to 750°C, results from the decomposition of carbonates. Note that temperature boundaries are approximate and depend on the heating rate and on how the water interacts with solid surfaces. The appearance of portlandite is probably due to the further hydration process during the storage, because of possible residual water after lyophilisation. Usually, the hydration process is stopped by rinsing sample with an organic solvent, but this step is prohibited in our study in order to avoid the presence of organic compounds, which would contribute to radiolytic H_2 production with a supplementary source (see Chapter 2.2).

The carbonation could be due to the existence of the atmospheric CO_2. The rate of carbonation of C-S-H is increasing with the pH [24]. As a consequence, the amounts of portlandite and carbonate increase with increasing C/S ratio (Table 13 and Table 14), which is the common observation in the previous literature.

Table 13. Portlandite content determined by TG analysis between 410 and 500°C of C-S-H samples with different C/S ratio and cured at different relative humidity. The relative uncertainty is estimated to be 10%.

		Portlandite content (%)				
		Real C/S ratio				
		0.80	0.97	1.14	1.30	1.40
RH (%)	Freeze-dried	3.2	2.1	6.8	5.8	5.8
	30%	2.3	2.5	6.3	5.0	7.7
	60%	3.1	2.0	4.8	4.4	4.7
	75%	1.6	1.8	2.8	2.9	3.3
	85%	2.3	2.0	3.1	3.2	3.0

Table 14. Calcite *content (550-750°C) calculated from thermogravimetry analysis between 550 and 750°C of C-S-H samples with different C/S ratio and cured at different relative humidity. The relative uncertainty is estimated to be 10%.*

		Calcite content (%)				
		Real C/S ratio				
		0.80	0.97	1.14	1.30	1.40
RH (%)	Freeze-dried	1.5	1.1	2.4	1.9	3.5
	30%	2.1	1.0	2.6	1.8	3.3
	60%	1.5	2.2	2.7	1.7	4.2
	75%	1.3	1.3	1.6	1.6	4.7
	85%	1.5	2.0	1.6	1.9	2.6

The water content is determined on the thermograms for each sample (Table 15).

Table 15. Water content (ambient-300°C) calculated from thermogravimetry analysis of different C/S ratio samples cured at different relative humidity. The relative uncertainty is estimated to be 10%.

		Water content (%)				
		Real C/S ratio				
		0.80	0.97	1.14	1.30	1.40
RH (%)	Freeze-dried	16.1±0.9	14.0±0.7	16.0±0.8	13.5±0.7	14.2±0.7
	30%	16.4±0.8	16.3±0.8	16.0±0.8	15.8±0.8	17.3±0.8
	60%	18.9±0.9	18.7±1.0	17.2±0.9	17.2±0.9	16.9±0.9
	75%	22.5±1.2	21.8±1.1	20.6±1.1	19.1±1.0	18.5±0.9
	85%	23.9±1.3	24.5±1.3	22.3±1.1	22.0±1.1	20.8±1.1

As a result, we found that:

- At a defined C/S ratio: when RH increases, water content increases too (Figure 3. 5)

- At a defined RH: when C/S ratio increases, water content decreases (except 1.40 CSH 30% RH) (Figure 3. 6).

However, the results from freeze-dried samples do not follow the trend. It may be due to the questionable drying efficiency [124], or to the fact that freeze-dried samples are easily hydrated during the short time used to weight the TGA samples.

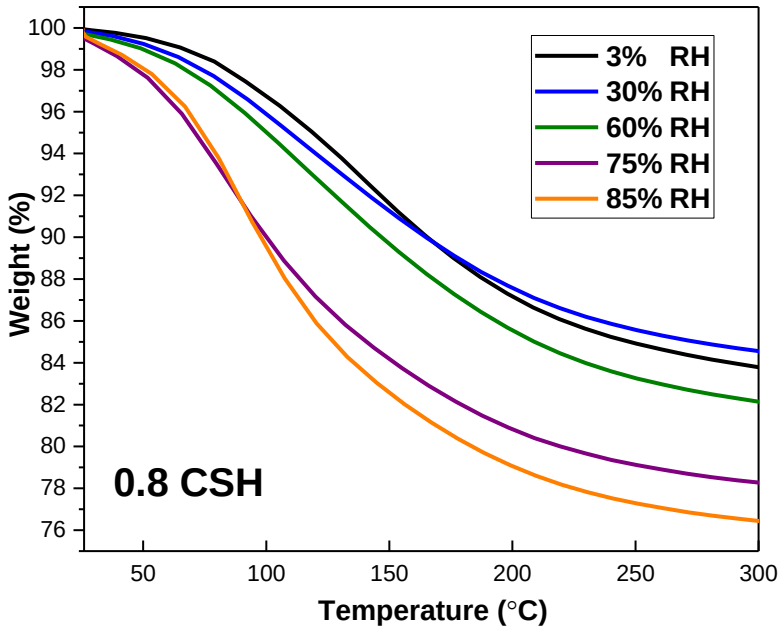

Figure 3. 5. TGA from 25 to 300 °C of 0.8 CSH according to relative humidity.

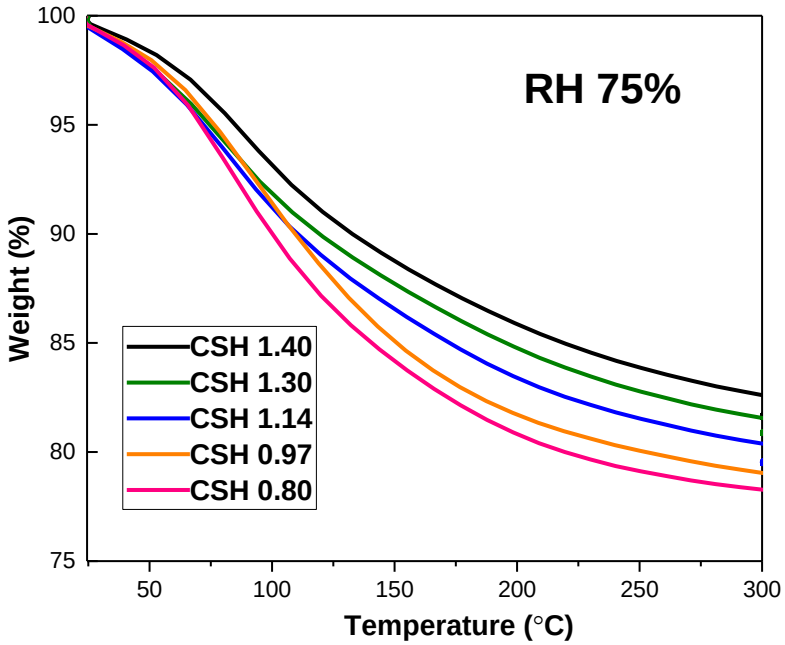

Figure 3. 6. TGA from 25 to 300 °C of CSH (C/S ratio=0.80, 0.97, 1.14, 1.30 and 1.40) cured at RH 75%.

Chemically Bonded Water (CBW, i.e. crystallization water and structural water) and Free Water (FW) that corresponds to water molecules more weakly bonded, were calculated according to [18][99][122]. The sum represents the total water content. As stated in reference roughly, free water weight loss occurs between ambient and 105°C while chemically bonded water weight loss occurs between 105°C and highest temperature (1000°C). But to simplify in our case, its value is only calculated from 105 to 300°C.

The Figure 3. 7 shows the distribution of CBW and FW of C-S-H samples with each C/S ratio cured at different RH.

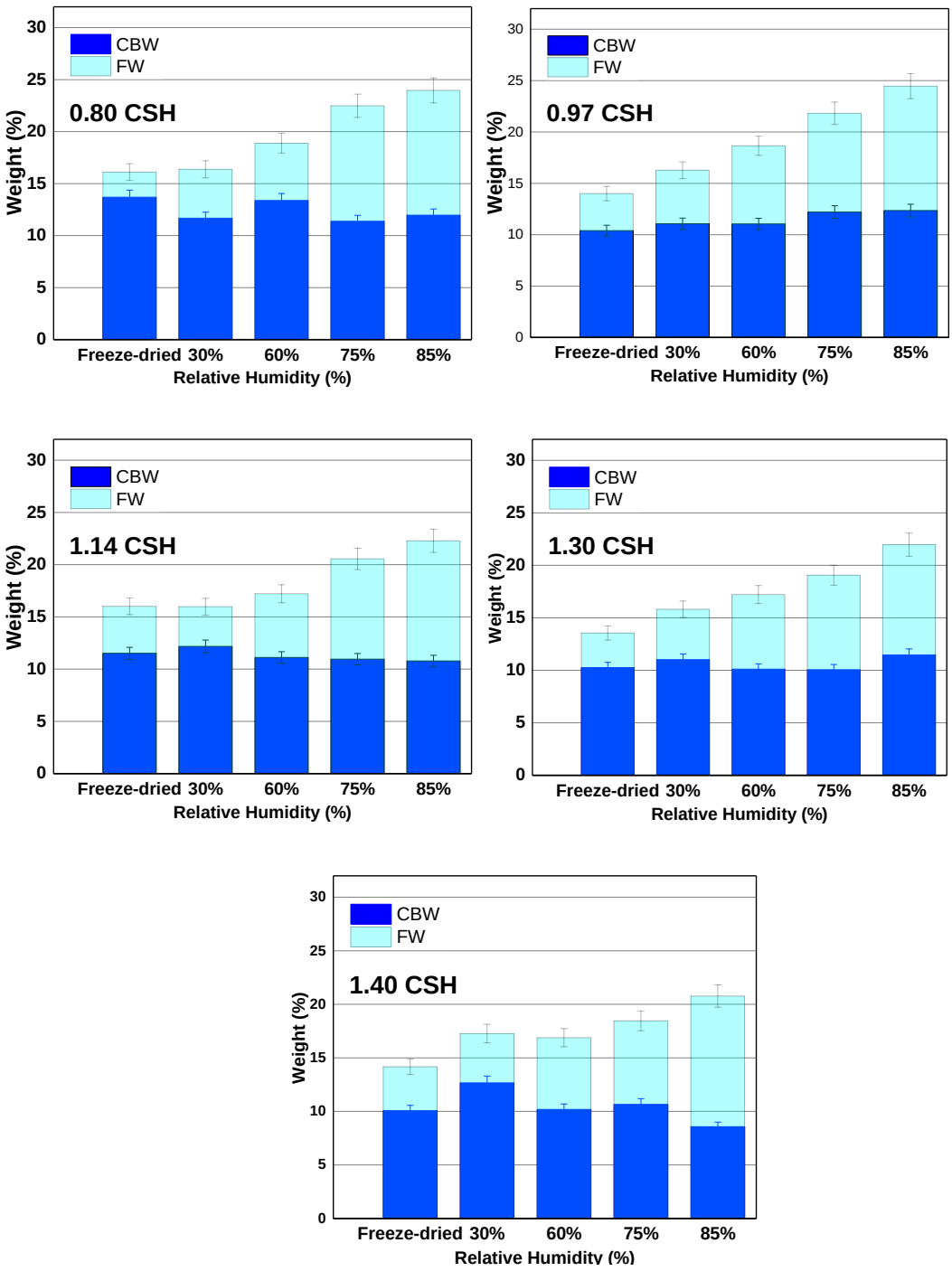

Figure 3. 7. Mass percentage of water (free water, FW; and chemically bound water, CBW) as determined from TGA measurements in samples 0.80, 0.97, 1.14, 1.30 and 1.40 CSH as a function of relative humidity.

As expected, Figure 3. 7 shows that the chemically bonded water content is almost constant, within the error bars, with RH in all systems, whereas free water increases with relative humidity. This validate a posteriori our treatment.

Free water (FW) is also detected for freeze-dried samples, as it was observed in clays [99][146]. This result confirms the fact that freeze-dried samples are very sensitive to the surrounding environment and humidity and could be easily hydrated during the analysis procedure when they are exposed to the atmosphere [127].

3.1.3. Porosity and specific surface area

In order to determine the influence of the porosity and the specific surface area on the hydrogen production, the freeze-dried C-S-H samples were analysed by nitrogen gas adsorption / desorption.

Specific surface areas, noted BET-SSA, were calculated using Brunauer-Emmett-Teller method (BET) where relative pressure P/P0 evolves between 0.05 and 0.3. Pore size distribution was obtained using a Barrett-Joyener-Halenda (BJH) model on the desorption isotherm. From the different C-S-H samples, the isotherms were all type-IV according to IUPAC, which is characteristic of a mesoporous material. Therefore, only isotherms from C-S-H with C/S ratio 0.97 were presented as an example (Figure 3. 8). The shapes of hysteresis loops were of the type H3, which was associated with mesopores formed due to aggregation of plate-like particles [128].

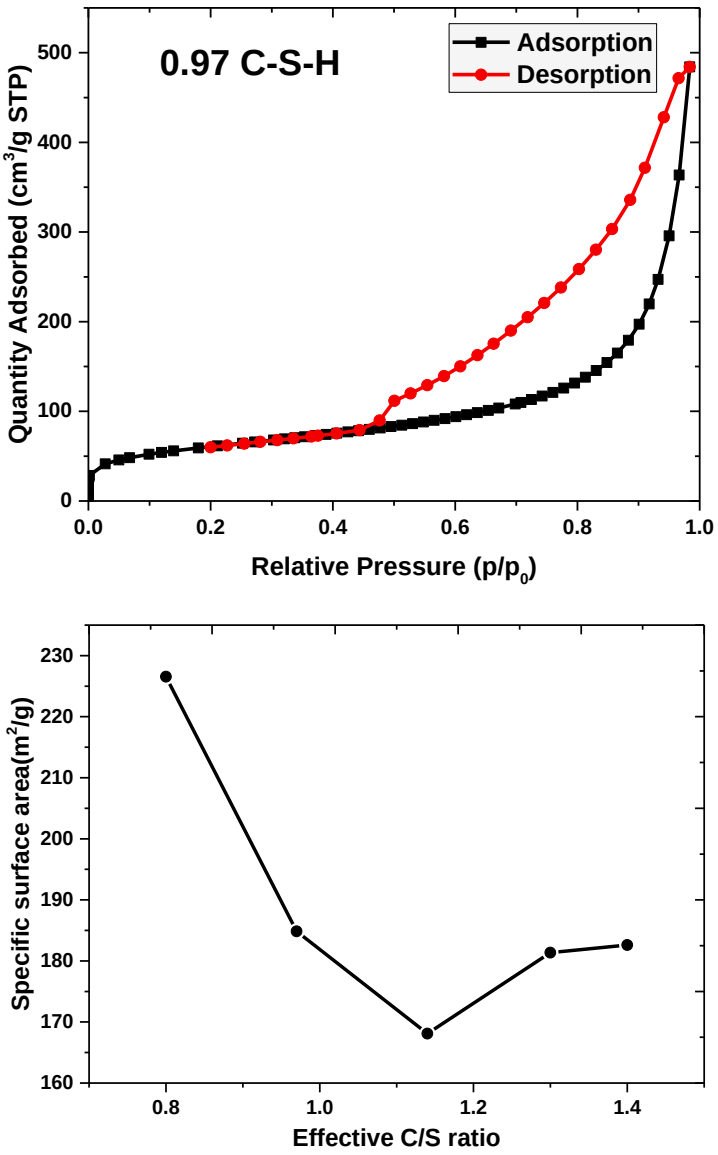

Figure 3. 8. Nitrogen adsorption/desorption isotherms of C/S ratio 0.97 CSH sample and the specific surface area as a function of the effective C/S ratio.

At C/S ratio 0.8, C-S-H has the highest specific surface area which is 226 m^2/g. Then, with increasing C/S ratio from 0.80 to 1.14, the specific surface area decreases from 226 to 168 m^2/g. This could be explained by an increase of the grain size from C-S-H 0.80 to C-S-H 1.14, which has been interpreted by Roosz [53], as an increase of the number of layers stacked along c axis (see chapter 1.1.3). C-S-H 1.40 displays a higher value (183 m^2/g) than C-S-H 1.2, the explanation could be due to the precipitation of portlandite nanoparticles during the drying step, which tends to increase the surface area of CSH, this has been suggested by Roosz [53] and this is in agreement with the detection of portlandite by thermogravimetric analysis.

Figure 3. 9 shows the corresponding PSD (Pore Size Distribution) of the samples. Unfortunately, the figure displays a wide distribution of pore sizes. In this case, it is difficult to explain the pore volume of C-S-H samples. It may be related to the limitation of this technique to analyse powder samples or attributed to the different pore types as it was described in chapter 1.1.4.

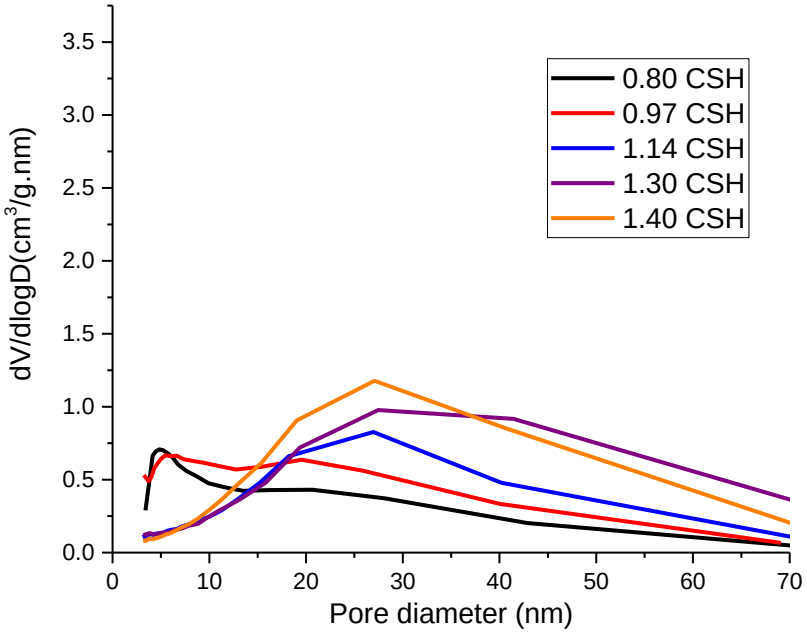

Figure 3. 9. Pore-size distribution curves of the CSH samples.

The calculated values of BET-SSA and BJH-porosity obtained with nitrogen gas adsorption-desorption are conditioned by a lot of hypothesis, noticingly on the pore geometry, and they are used only to compare the different C-S-H samples. In order to appreciate the validity of the SSA and porosity values obtained with nitrogen gas adsorption-desorption, it should be interesting to compare them with those obtained by water vapor adsorption-desorption. As the size of the water molecule is smaller than this of nitrogen molecule, the water vapor should access to smaller pores. Moreover, contrary to nitrogen gas, the water should chemically interact with the material.

The Nitrogen gas and water vapor adsorption-desorption curves of 1.30 CSH samples are presented in Figure 3. 10. In the case of water vapor adsorption-desorption curves: on the adsorption branch, firstly, water is sorbed in surfaces and fill the mesopores until 95% RH. In the desorption branch, the water is removed from the mesopores and the external surfaces. But, as the water could chemically interact with the material, possibly through hydrogen bonding [26] [129], a part of sorbed water could not be desorbed [53], that is why, the change in mass in desorption curve at 0% is higher than in sorption curve.

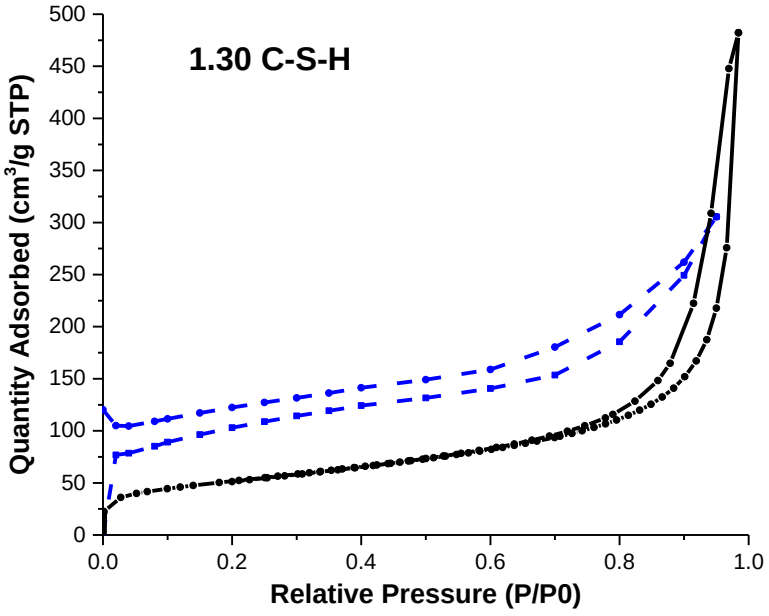

Figure 3. 10. Nitrogen (black solid line) and Water (blue dash line) vapor adsorption/desorption isotherm of 1.30 C-S-H.

The BET specific surface area were deduced from isotherms and compared with those obtained by nitrogen gas isotherms in Table 16. The comparison with BET-SSA values obtained with nitrogen gas isotherm, gives a similar trend, but with higher values except for C-S -H 1.30.

Table 16. Surface area from BET theory of C-S-H sample measured from Nitrogen and Water vapor isotherms.

Samples	S_{BET} (m^2/g)		Reference
	Nitrogen adsorption	Water vapor adsorption	
C-S-H 0.6	408	431	[53]
C-S-H 0.80	227	N.A.	Our results
C-S-H 0.97	185	N.A.	Our results
C-S-H 1.14	168	N.A.	Our results
C-S-H 1.2	194	214	[53]
C-S-H 1.30	181	159	Our results
C-S-H 1.40	183	N.A.	Our results
C-S-H 1.6	231	180	[53]

3.1.4. Wide and Small-Angle X-Ray Scattering (WAXS/ SAXS)

WAXS/ SAXS are particularly useful to investigate divided structures like C-S-H materials. Samples could be studied in their natural saturated state, thus avoiding difficulties associated with drying process and providing information about the microstructural features (e.g., interlayer distance (d-spacing), shape, specific surface area (SSA)…).

Figure 3. 11 presents intensity data (including SAXS, WAXS and XRD) in function of Q(diffusion vector) for 0.80 CSH 60% RH sample. The scattered intensity data obtained by SAXS measurements is fitted by a cylinder-lamellar model [125][126][130] presented in Figure 3. 12. The Figure 3. 11 shows that the applied model enable to describe the SAXS data of C-S-H.

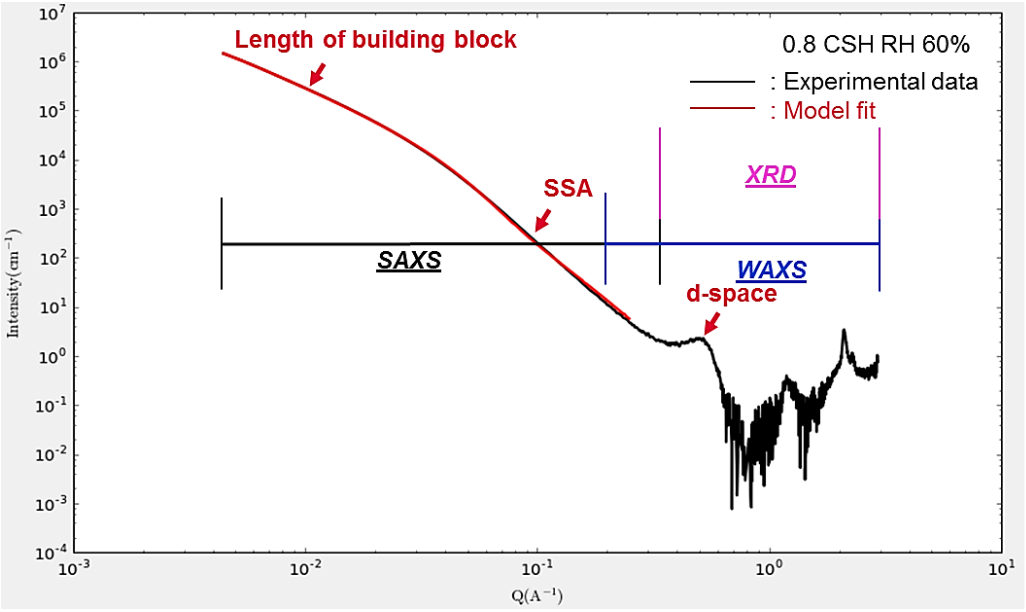

Figure 3. 11. Model fitting result of SAXS data for 0.8 CSH RH 60%.

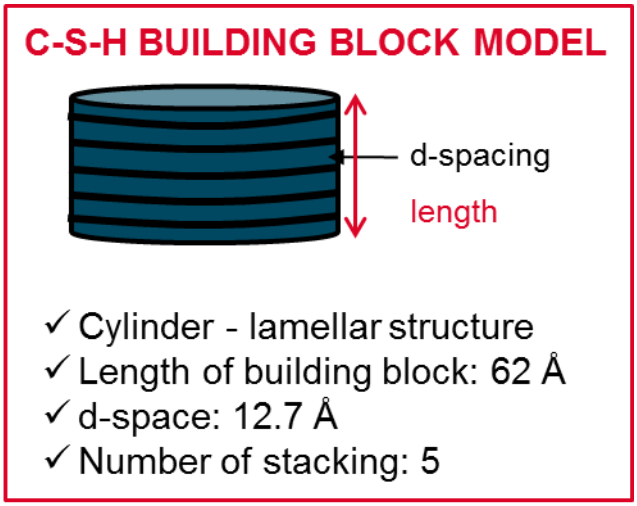

Figure 3. 12. C-S-H 0.8 RH 60% building block model.

From this model, the parameters of the C-S-H building block can be deduced as the length of building block, the d-spacing and the number of stacking.

The determined length of the building block is consistent with direct observation by TEM (see Figure 3. 13). From these observations, the thickness of the C-S-H nanofoils could be estimated. The value of the thickness obtained is between 3 and 6 nm, accordingly to published results [131].

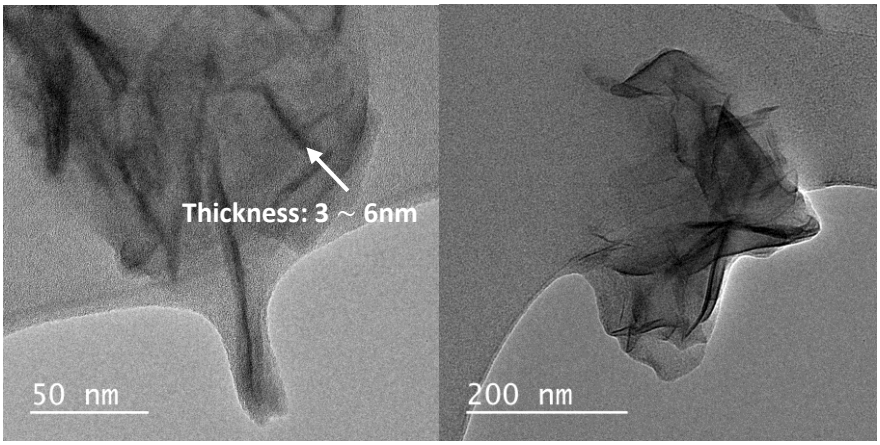

Figure 3. 13. TEM image of CSH 1.40.

The SSA can be calculated from the linear SAXS part using the equation which was discussed before (see ANNEX 5).

The SSA values in Table 17 are 2.5 to 4.4 times lower than those obtained using N_2 adsorption measurements. The reason for these different values are unclear, although it might be related to the difference in thermal treatment and outgassing of the powders before BET analysis. However, we were not interested in the absolute SSA values, we only focused on the trend of the SSA values with various C/S ratio. From Table 17, the trend obtained by SAXS technique is consistent with that obtained by N_2 gas sorption/ desorption experiments.

Table 17. Specific surface area as of C-S-H samples with different C/S ratio.

	SAXS	N_2 gas sorption/ desorption
	S_{BET} (m^2/g)	
C-S-H 0.80 RH 60%	86	227
C-S-H 0.97 RH 60%	42	185
C-S-H 1.14 RH 60%	43	168
C-S-H 1.30 RH 60%	60	181
C-S-H 1.40 RH 60%	78	183

3.1.5. Effect of radiation on the structure

In order to correctly interpret the results on the evolution of radiolytic hydrogen production with C/S ratio, we need to check that gamma and heavy ions irradiations conducted in this work do not induce damages or alterations on the structure. Then, the samples presented in this section are only those irradiated using gamma irradiation at 200 kGy. If no changes are observed, then no alterations would occur on C-S-H samples in the dose range of this study. The characterizations of samples under heavy ions irradiation are not presented here, as the characterizations were made after a long period of radioactive decay of the samples. As the samples were exposed to the atmosphere, then the C-S-H would carbonate.

3.1.5.1. XRD

XRD was conducted on non-irradiated/ irradiated samples to see if any modifications occurred after irradiation in the interlayer distance and mineral phases. The XRD patterns of pristine and 200 kGy irradiated C-S-H samples are compared in Figure 3. 14.

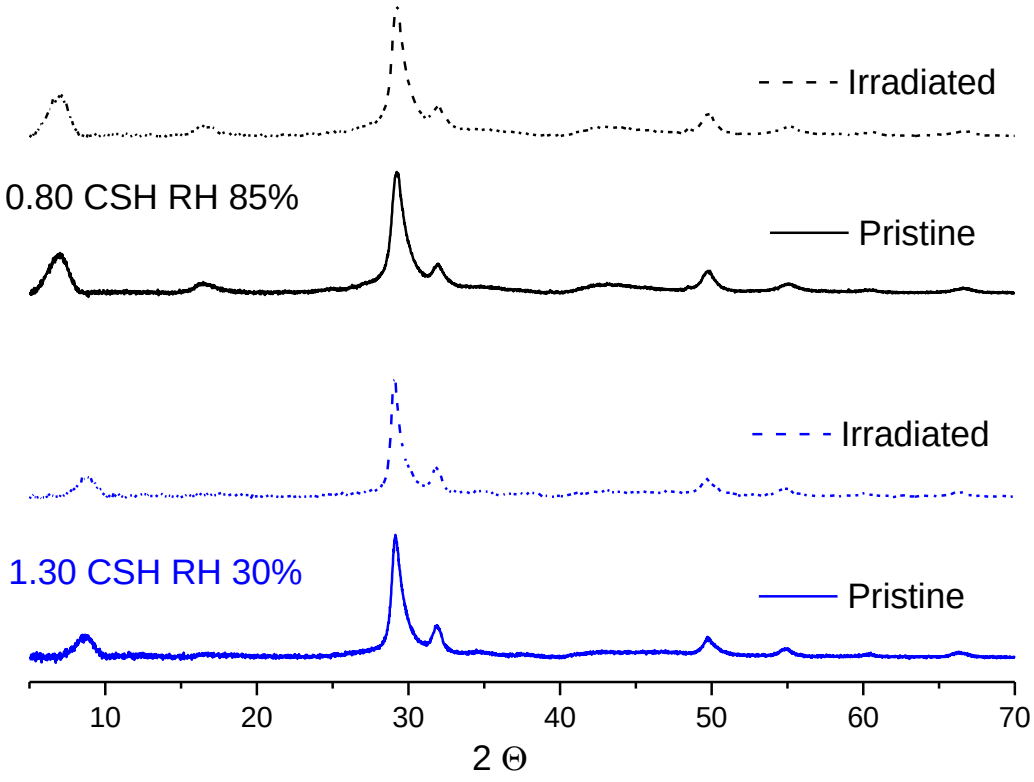

Figure 3. 14. X-ray diffraction patterns of 1.30 CSH RH 30% (blue line) and 0.80 CSH RH 85% (black line) before (solid line) and after (dash line) irradiation at 200 kGy.

No differences in phases and no changes in the interlayer distance were observed when comparing pristine and irradiated samples.

3.1.5.2. TGA

In order to check if water content and carbonation are modified under irradiation, TGA was done on 200 kGy irradiated C-S-H samples. The comparison of the thermograms obtained from the pristine and the irradiated samples is shown in Figure 3. 15.

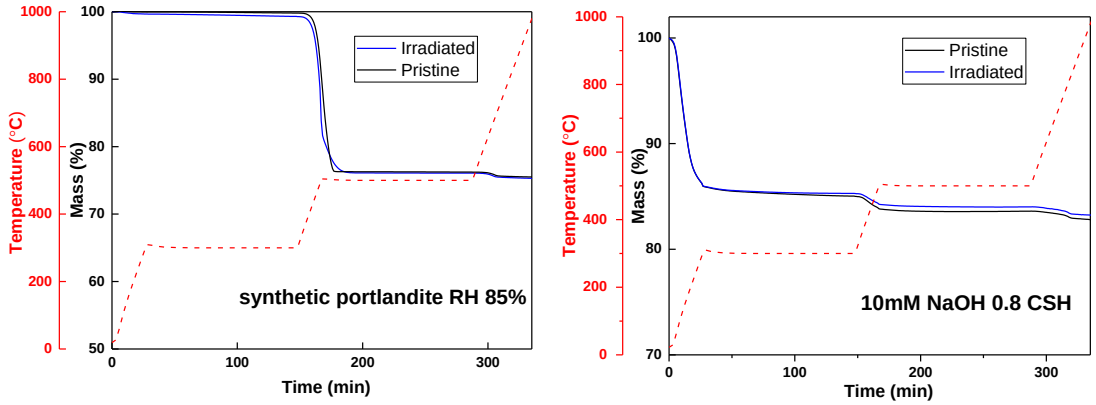

Figure 3. 15. TG thermograms of synthetic portlandite samples RH 85% and freeze dried 10mM NaOH 0.8 CSH samples.

Considering water content (the amount of CBW and EW) and a supposed extent of carbonation under irradiation, no difference is observed between pristine and irradiated samples. This means, in particular, that the global amount of water is not affected by our experimental irradiation conditions and that only a small amount of water is affected by the ionizing radiation.

As a consequence of these experiments, the compositions and the structures remain the same after irradiation.

3.2. Hydrogen production

As explained in Chapter 2, samples of C-S-H were stabilized into desiccator chambers where relative humidities of 3, 30, 60, 75 and 85% at room temperature were maintained using silica gel and different saturated salt solutions under N_2 atmosphere (see Chapter 2.2). The samples have been irradiated using gamma rays and swift heavy ions, in order to examine the effect of LET. The results will be presented and discussed with respect to the amount of sorbed water. Each point is repeated at least 4 times to take into account the risk of leak of the ampoules.

3.2.1. Effect of the water amount and the nature of the C-S-H on gamma rays irradiation

The production of H_2 from freeze-dried and samples hydrated at 30, 60, 75 and 85% RH, irradiated using gamma rays at a dose ranging between 100 and 200 kGy is proportional to the dose. Figure 3. 16 gives an example of molecular hydrogen production from hydrated 1.30 C-S-H. The radiolytic yields deduced from the slope of the different curves are resumed in Table 18. The uncertainties considered are that related to experimental errors.

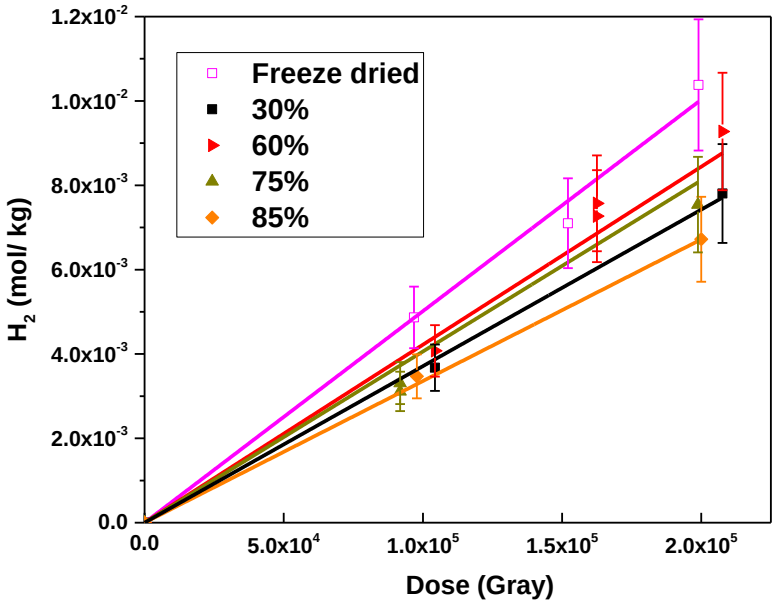

Figure 3. 16. Dose dependence of H_2 production for hydrated 1.30 C-S-H equilibrated in different relative humidity at room temperature (freeze-dried, 30, 60, 75 and 85 % RH).

All the results are summarised in Table 18. At 30%, 60, 75 and 85% RH, hydrogen production decreases in the order (except 0.97 C-S-H at 30% and freeze dried samples):

0.80 C-S-H > 0.97 C-S-H > 1.14 C-S-H > 1.30 C-S-H > 1.40 C-S-H

Table 18. Hydrogen radiolytic yields (10^{-7} mol/J) (calculated with respect to the total energy received by the system) released from Gamma irradiated C-S-H samples with different C/S ratio hydrated at different RH at room temperature. Yields standard deviations are estimated to be 15% for all samples.

$G(H_2)$ (mol/J×10^{-7}) **(calculated with respect to the total energy received by the system)**		**Real C/S ratio**				
		0.80	0.97	1.14	1.30	1.40
RH (%)	3%	0.52±0.08	0.56±0.08	0.46±0.07	0.50±0.08	0.32±0.05
	30%	0.69±0.10	0.39±0.06	0.44±0.07	0.37±0.06	0.35±0.06
	60%	0.61±0.10	0.58±0.09	0.49±0.07	0.42±0.07	0.36±0.06
	75%	0.66±0.10	0.61±0.10	0.44±0.07	0.41±0.06	0.35±0.06
	85%	0.62±0.10	0.62±0.10	0.46±0.07	0.34±0.05	0.35±0.06

The $G(H_2)$ values are presented in Figure 3. 17 as well as the value of primary $G(H_2)$ of bulk water. From this figure, the most striking result to emerge from the data is whatever the water uptake, the $G(H_2)$ is almost constant and C-S-H materials produce the same quantity as an equivalent mass of bulk water. It implies that efficient H_2 production mechanisms take place in C-S-H samples. These mechanisms will be presented in discussion part.

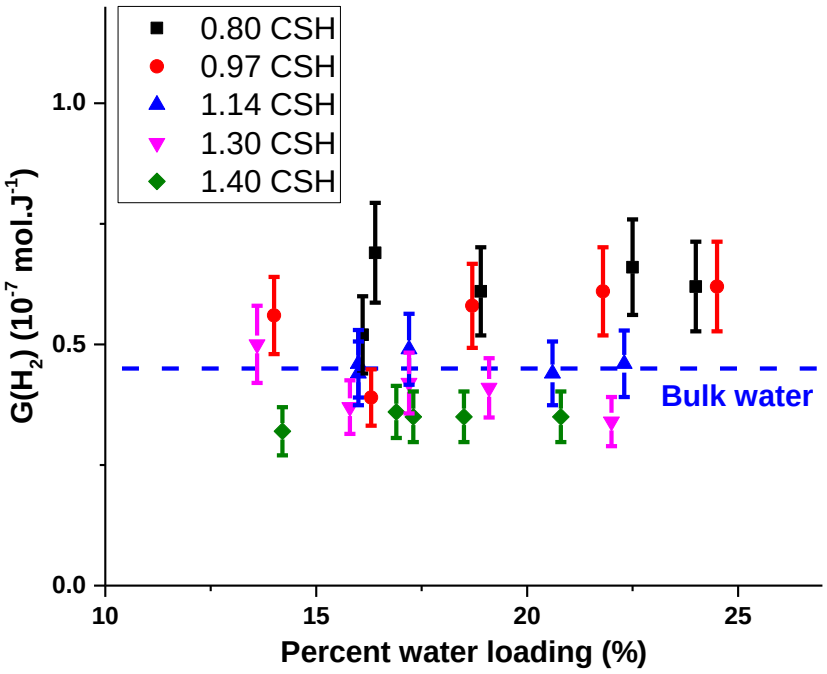

Figure 3. 17. Hydrogen production from C-S-H with respect to water loading. Black dotted line (primary radiolytic yield of liquid water). Yields standard deviations are estimated to be 15% for all samples.

If we consider that radiolytic hydrogen is provided from free and chemically bonded water, the hydrogen production could be easily compared between all the samples by taking into account the total water content measured by TGA of each sample. Then, we could introduce a normalized dihydrogen radiolytic yield calculated by:

$$G_{norm.}(H_2) = G(H_2)/\nu_{H_2O} \quad (19)$$

Where $G(H_2)$ is the radiolytic yield of hydrogen production,

ν_{H2O}, the weight fraction of water in each sample determined by TGA.

Table 19 present the dihydrogen yield with respect to the energy received solely by water for each C-S-H sample.

Except for freeze-dried samples, G_{norm} (H_2) values tend to decrease when C/S ratio increases generally. This result suggests that [Ca^{2+}] do not promote H_2 production in C-S-H, contrary to what it is observed in ref [18].

Table 19. Hydrogen radiolytic yields (10^{-7} mol/J) (calculated with respect to the energy received solely by water) *released from Gamma irradiated C-S-H samples with different C/S ratio hydrated at different RH at room temperature. Yields standard deviations are estimated to be 15% for all samples.*

$G_{norm.}$ (H_2) (mol/J×10^{-7}) (calculated with respect to the energy received solely by water)		**Real C/S ratio**				
		0.80	0.97	1.14	1.30	1.40
RH (%)	3%	3.2±0.5	4.0±0.6	2.9±0.4	3.7±0.6	2.3±0.3
	30%	4.2±0.6	2.4±0.3	2.8±0.3	2.3±0.2	2.0±0.3
	60%	3.2±0.5	3.1±0.5	2.8±0.4	2.4±0.4	2.1±0.3
	75%	2.9±0.4	2.8±0.4	2.1±0.3	2.1±0.3	1.9±0.3
	85%	2.6±0.4	2.5±0.5	2.1±0.3	1.5±0.2	1.7±0.3

3.2.2. Heavy ions irradiations

In order to precise the influence of LET in C-S-H, experiments were conducted using $^{36}Ar^{18+}$ heavy ions. Due to the beamtime limitation, only 85% RH and few 30% RH C-S-H samples were irradiated.

As an example, the production of H_2 from C-S-H hydrated at 85% RH, irradiated at a dose ranging between 400 and 1000 kGy is proportional to the dose (see Figure 3. 18). In Table 20, radiolytic yields of molecular hydrogen were summarized, as well as normalised G(H_2) values and normalised and corrected G(H_2) values. The last ones have been calculated taking into account the LET different in water and entire CSH system using equation:

$$correction\ coefficient = \frac{LET_{water}}{LET_{CSH\ entier\ system}} \quad (20)$$

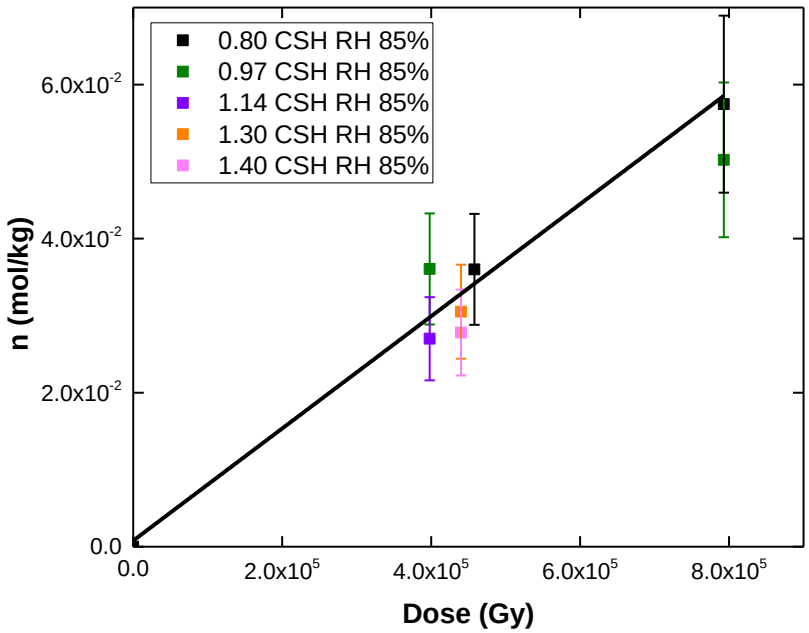

Figure 3. 18. Hydrogen production at RT from C-S-H with different C/S at 85% RH irradiated with $^{36}Ar^{18+}$ as a function of the dose, Yields standard deviations are estimated to be 20% for all samples.

Table 20. Radiolytic yields of irradiated samples using heavy ions.

Samples	**$G(H_2)$ (mol/J×10^{-7})** (calculated with respect to the total energy received by the system)	**$G(H_2)$ (mol/J×10^{-7})** (calculated with respect to the energy received solely by water)	**$G(H_2)$ (mol/J×10^{-7})** (calculated with respect to the energy received solely by water) corrected dose difference deposite in CSH and water
0.8 CSH RH 85%	0.74±0.15	3.1±0.6	2.6±0.5
1.0 CSH RH 85%	0.69±0.14	2.8±0.6	2.3±0.5
1.2 CSH RH 85%	0.68±0.14	3.0±0.6	2.5±0.5
1.4 CSH RH 85%	0.69±0.14	3.1±0.6	2.6±0.5
1.6 CSH RH 85%	0.63±0.13	3.1±0.6	2.6±0.5
0.8 CSH RH 30%	0.56±0.11	3.4±0.7	2.8±0.6
1.2 CSH RH 30%	0.50±0.10	3.1±0.6	2.6±0.5
Bulk water	/	/	1.04 [74]

Surprisingly, by comparing the results obtained using heavy ions (HI) with those obtained with gamma-rays irradiations (Table 21), $G(H_2)$ values obtained with HI irradiations are almost similar with gamma-ray irradiations (for example, for 0.8 CSH RH 85%, $G_{HI}(H_2)$ = 0.74×10^{-7} and $G_\gamma(H_2)$ = 0.62×10^{-7} respectively). Generally, the G values should be different since heavy ion radiations (high LET) can change substantially the H_2 yields by increasing locally the concentration of ionization sites. Indeed, when increasing the excitation and ionization densities through ion beam irradiations, the density of radiation-induced defects increases around the ion track. Due to the high density of reactive species in the track, a quick recombination of primary species can be expected. So, an increase of hydrogen is generally observed.

Table 21. Radiolytic yields of irradiated samples using gamma rays and heavy ions (calculated with respect to the total energy received by the system).

Samples	**$G_{HI}(H_2)$ (mol/J×10^{-7})** **(calculated with respect to the total energy received by the system)**	**$G\gamma(H_2)$ (mol/J×10^{-7})** **(calculated with respect to the total energy received by the system)**
0.8 CSH RH 85%	0.74±0.15	0.62±0.09
1.0 CSH RH 85%	0.69±0.14	0.62±0.09
1.2 CSH RH 85%	0.68±0.14	0.46±0.07
1.4 CSH RH 85%	0.69±0.14	0.34±0.05
1.6 CSH RH 85%	0.63±0.13	0.35±0.05
0.8 CSH RH 30%	0.56±0.11	0.69±0.10
1.2 CSH RH 30%	0.50±0.10	0.42±0.06
Bulk water	1.04	0.44

Figure 3. 19 presents the H_2 yields calculated respected to the energy directly received solely by water (the normalized $G(H_2)$) obtained by gamma irradiation and obtained by heavy ions irradiation from C-S-H with various C/S ratio at RH 85%. The results show the trends are totally different. Under gamma rays, $G_\gamma(H_2)$ values tend to decrease when C/S ratio increases. In contrast, the normalized $G_{HI}(H_2)$ values are constant with various C/S ratio.

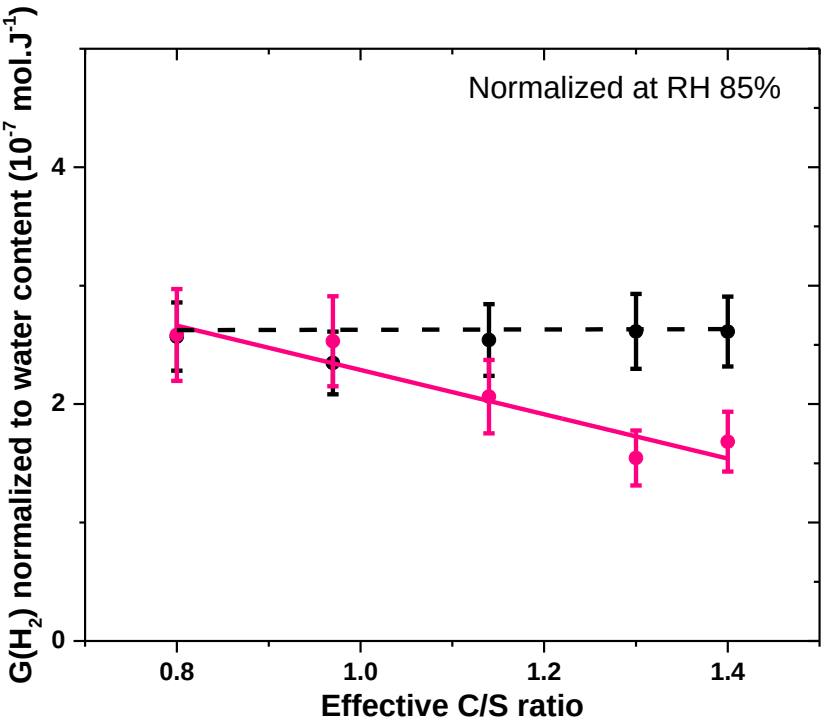

Figure 3. 19. The normalized H_2 radiolytic yields obtained by gamma irradiation (in solid pink colour) and obtained by heavy ions irradiation (in black dash colour) (calculated with respect to the energy received solely by water) corrected different dose deposite in CSH and water at 85% RH as a function of the experimental C/S ratio.

3.3. Radiation-induced defects

In this section, EPR spectra of C-S-H samples from electron beam irradiation have been measured and will be discussed. The study of Radiation-induced defects (RID) is developed. The aim of this section is to identify the defects, to investigate the effect of the C/S ratio, water content, and temperature on RID in C-S-H.

3.3.1. C/S ratio effect in C-S-H

Figure 3. 20 presents the EPR spectra of electron irradiated at 77 K C-S-H with different C/S ratio. All the samples were freeze-dried before irradiation.

A doublet separated by 50 mT assigned to H radicals is observed in all C-S-H samples [132,133]. The hyperfine constant is very close to that for free H atom (50.8 mT) and for H atoms in frozen aqueous solutions. This suggests that H atoms are surrounded by water molecules. From a comparison of our spectrum and the literature [132,133], we suggest there is only one site of H atoms that can be observed in the spectrum.

Note: Figure 3. 20 presents only the low field part of the H atoms signals. The dotted lines are a zoom of this zone. The factor of magnitude is 10.

Regardless of the material, the EPR spectrum is composed of a central line centered around g=2.010. It is the superposition of different signals and its deconvolution is not straightforward. Nevertheless, some features can be identified:

A broad shoulder whose maximum is located around g=2.065 for C-S-H 0.80, 0.97 and 1.30. The maximum is shifted around g=2.044 for C-S-H 1.14 and 1.40. This shoulder reveals a broad distribution of g value. Similar distributions have been reported for hole centers trapped in alkali aluminosilicate or silicate glasses. We assign this to a $O^{\circ -}$centre.

A narrow singlet line with g=2.0029. This signal is more intense for C-S-H 1.30. In glasses, a similar spectrum was attributed either to carbon contamination [134] or to different type of oxygen hole center [107].

The high field signal corresponding to g=1.994 reveals an anisotropic signal (called RID I in the following). From the comparison with various published results, this signal is attributed either to O_2^- or peroxy radical (see Chapter 1.2.8.6). It can come from the following reactions

$$O^{\circ -} + O^{\circ -} \rightarrow O_2^{2-} \quad (21)$$

$$O_2^{2-} + hole^+ \rightarrow O_2^- \quad (22)$$

$O^{\circ -}$ center associated with portlandite is observed in high C/S ratio (signal at $g_x = g_y$ =2.074).

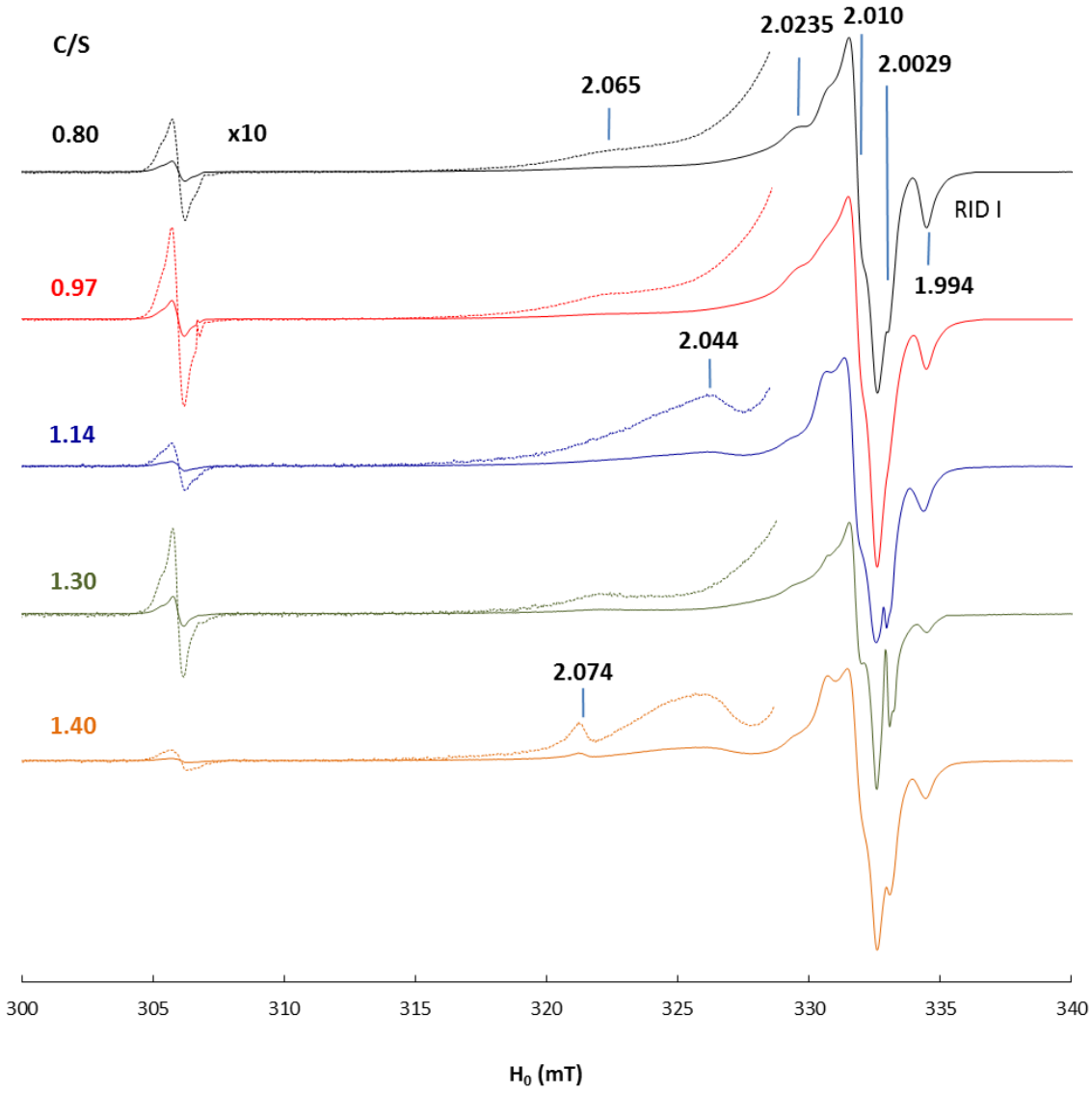

Figure 3. 20. The EPR spectra of electron irradiated at 77 K C-S-H with different C/S ratio.

In order to estimate the total number of RID, we performed a numerical integration of the different signals. Taking into account the complex shape of the spectra, the accuracy of the numerical integration is not precise and the errors tentatively evaluated at ±20%. Considering the quantification conversion uncertainty, the total errors are fixed at ±35%. The results are summarized in Table 22.

The concentration of H atoms and the hydrogen yield seem to have the same variation with the C/S ratio: the highest value was measured for C/S=0.97 and the lowest for C/S=1.40.

The concentration of RID is nearly the same in all the samples except 1.30 C-S-H that presents a weaker concentration. As this sample was irradiated at a dose of 15 kGy instead of 30 kGy, this difference can be attributed to a dose-effect. Then we suppose that the data suggest that radiolytic yield of RID formation is independent of the C/S ratio.

We notice that the ratio of mean values G(RID) and $G(H_2)$ varies by less than a factor 2. This close relationship is compatible with the hypothesis that RID represents the radiative oxidative counterpart of hydrogen. As the creation of RID seems independent of the C/S ratio, we suppose that the difference observed for hydrogen production can be attributed to a difference in recombination process or to back reaction of H_2 with RID for example.

Table 22. The concentration of H atoms and RID and the corresponding radiation yields in different electron irradiated samples at doses 30 kGy (except 1.4 CSH, at dose 15kGy) at 77K, the experimental accuracy is estimated to be ±35%.. Hydrogen radiolytic yields released from Gamma irradiated CSH samples at room temperature are recalled, the experimental accuracy is estimated to be ±15%.

C/S ratio	**0.80**	**0.97**	**1.14**	**1.30**	**1.40**
H atoms (/g)	$1.3\ 10^{16}$	$2.0\ 10^{16}$	$5.4\ 10^{15}$	$8.5\ 10^{15}$	$4.4\ 10^{15}$
RID (/g)	$1.4\ 10^{18}$	$1.6\ 10^{18}$	$1.5\ 10^{18}$	$5.4\ 10^{17}$	$1.4\ 10^{18}$
G(RID) (mol/J×10^{-7})	0.81	0.89	0.82	0.60	0.81
G(H_2) (mol/J×10^{-7}) **(calculated with respect to the total energy received by the system)**	0.52	0.56	0.46	0.50	0.32

3.3.2. Effect of water content

Now we examine the effect of water on the RID. Figure 3. 21 presents the EPR spectra of electron irradiated at 77 K of C-S-H with C/S=0.80. These materials were freeze-dried or equilibrated in different humidity. The results evidence that there is no significant differences when the relative humidity varies from 3% (freeze-dried) to 60% considering the uncertainty. This result is in accordance with hydrogen gas production measurements.

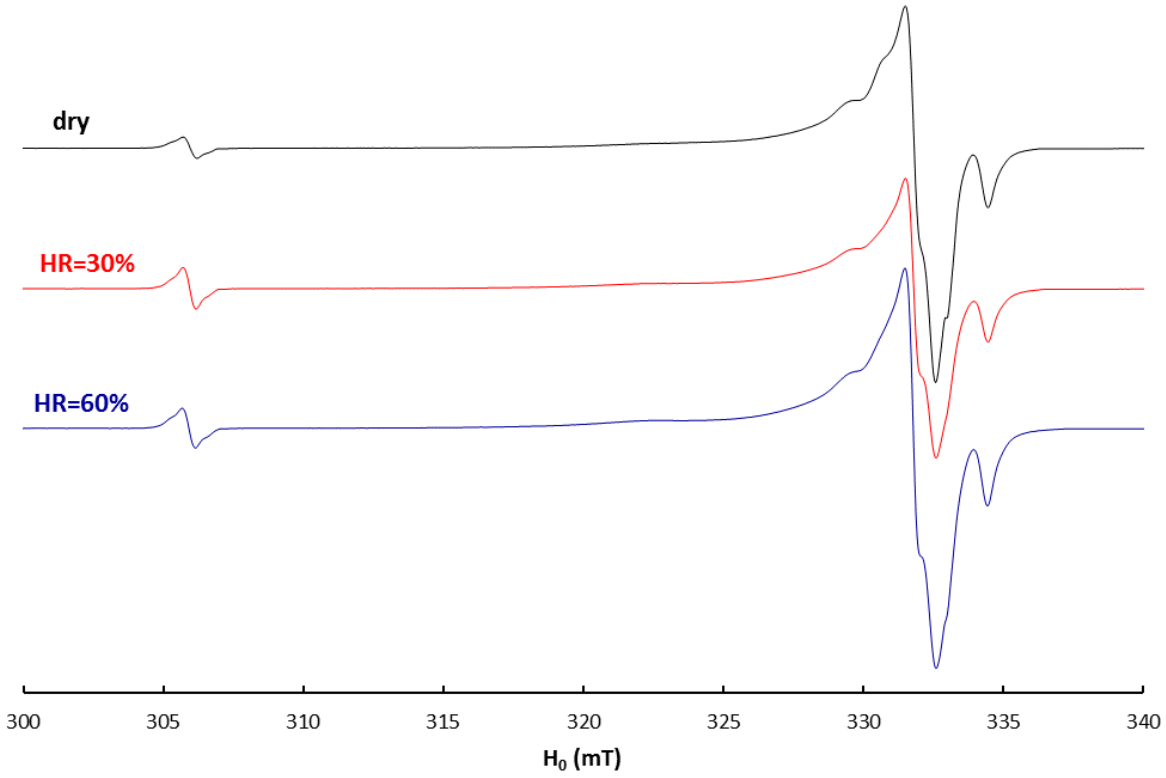

Figure 3. 21. The EPR spectra of electron irradiated at 77 K of 0.80 C-S-H with different relative humidity.

3.3.3. Effect of Temperature

As the temperature increases, the signal of H atoms decreases with temperature. It also becomes dissymmetric. Above 140K, we did not succeed to adjust or numerically integrate the signal. Unfortunately, it is not possible to discuss the mechanism of destruction of the H atoms.

Figure 3. 22 presents the effect of annealing at the different temperature on the EPR spectrum of dry 1.30 C-S-H irradiated at 77 K. All the spectra were recorded at 100 K after annealing.

Note: The dotted lines represents a zoom of the low field zone. For each curve, the factor of magnification is specified on the graph.

Important changes are observed with the temperature:

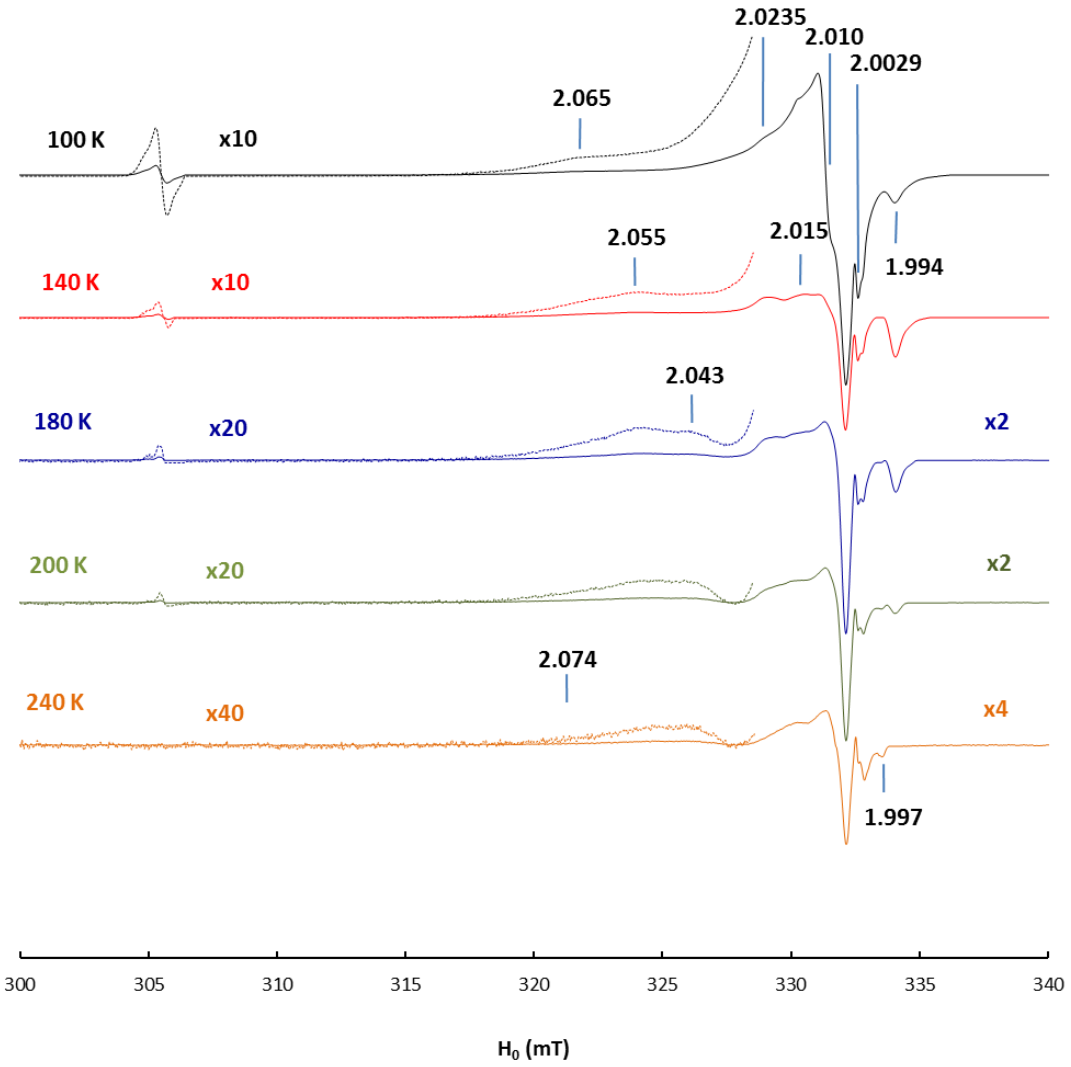

Figure 3. 22. EPR spectra of electron irradiated at 77 K of C-S-H with C/S=1.30 and annealed at different temperatures. All the spectra were recorded at 100 K. The dotted lines represent a zoom of the low field zone. For each curve, the factor of magnification is specified on the graph.

The main changes are the following:

- Above 100 K, the single line disappears that let appearing an anisotropic signal. The evolution with the temperature of spectra shows the signal is a superposition of different lines (see below).
- The low field broad shoulder also undergoes change with temperature (a zoom of this region is presented in Figure 3. 23).
- At 140 K, the concentration of RID I (g_z=1.994) increases by a factor 2 approximatively. This enhancement may be related to the growth of a new shoulder centered at g=2.055 (see Figure 3. 23).

- The signal of RID I disappears above 200 K.
- A new signal (axial or rhombic symmetry) with g_z=1.997 grows above 200 K (it is clearly observed at 240 K, see Figure 3. 23).

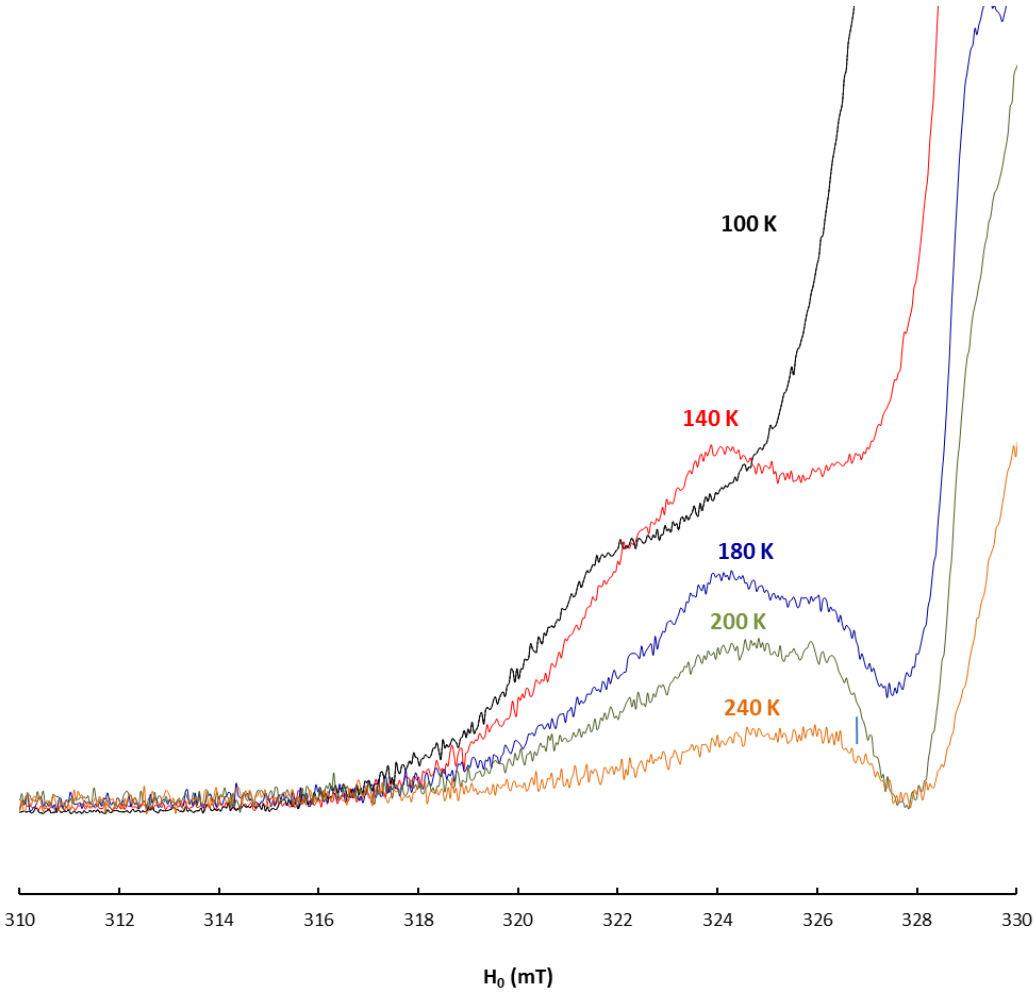

Figure 3. 23. Evolution with the temperature of the low field region of EPR spectra of electron irradiated at 77 K of C-S-H with C/S=1.30.

Figure 3. 24, the total intensity of RID EPR signal calculated by numerical integration is presented as a function of temperature. On the same figure, we plot the evolution of the height of RID I signal.

Note: The value (intensity and height) were divided by the value determined at 100 K and multiplied by the temperature (the intensity of the EPR signal is inversely proportional to the temperature).

We notice that the destruction of centers begins already at 100 K. At the same time, an increase of RID I concentration is observed. This rise continues until 140 K then the number of RID centers starts to decline. An important drop in the total concentration is also present at this temperature.

If we suppose that the destruction of RID is due to recombination of $O^{\circ-}$ centers and that RID I is attributed to O_2^- then the following mechanism has to be hypothesized:

$$O^{\circ-} + O^{\circ-} \rightarrow O_2^{2-}$$
$$O_2^{2-} + hole^+ \rightarrow O_2^-$$

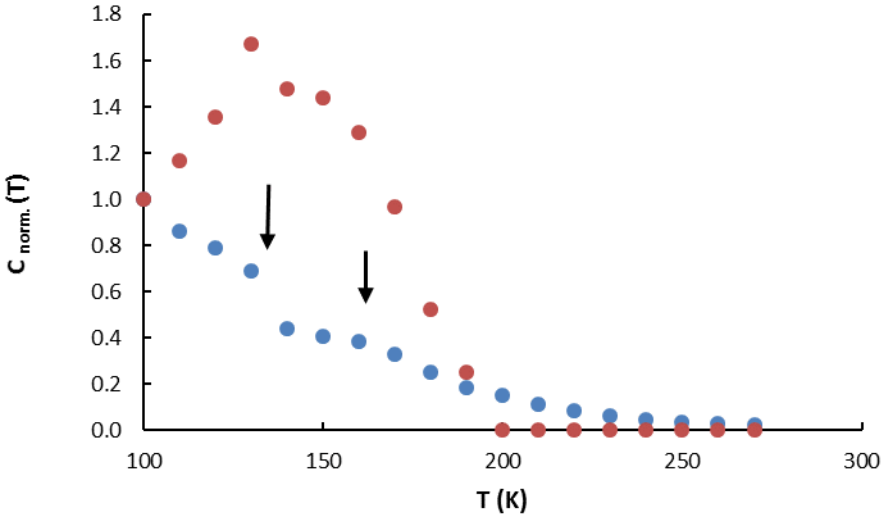

Figure 3. 24. Temperature evolution of the total intensity of the RID signal (blue points) and the height of the RID I signal (red points).

Above 160 K (see Figure 3. 25), the decay of RID can be interpreted by thermal activated recombination. The estimated activation energy is ~11 kJ/mol.

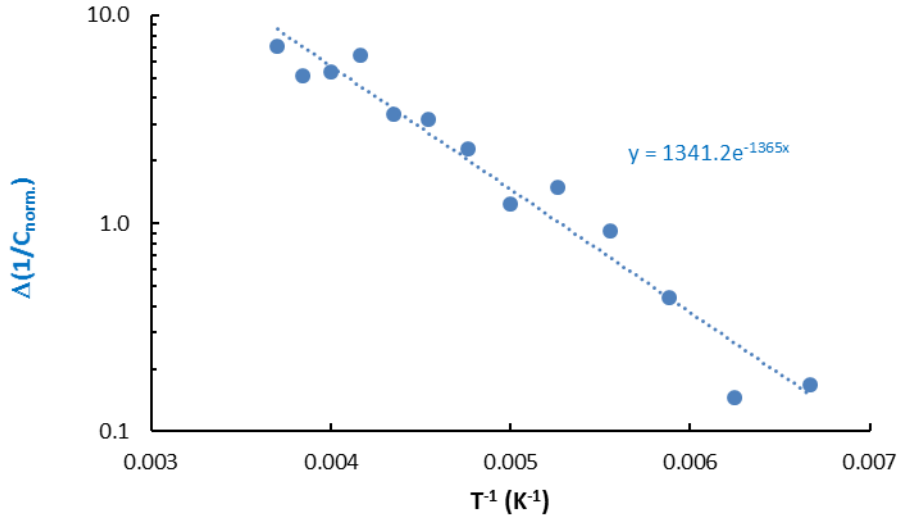

Figure 3. 25. A plot of $\Delta(1/C_{norm.})$ as a function of T^{-1}

After annealing at 280 K (Figure 3. 26), the shape of the signal is very close to those observed in portlandite in the same condition, but with an intensity 10 times smaller. The remaining signal can be attributed to residual portlandite.

The signal is tentatively attributed to the superposition of:

O_2^-: $\langle g_z \rangle$=2.05, g_y=2.0079, g_x=2.0018 (g_y and g_x were calculated using W. Känzing and M.H. Cohen theory assuming $\lambda/E = 0.0031$)

O_3^-: g_z=2.017, g_y=2.006, g_x=2.001

CO_2^-: g_z=2.002, g_y=2.0017, g_x=1.9974 [135]

Further investigations are needed to support this decomposition.

The signal attributed to O_2^- has the characteristics of the centers observed only in disordered materials such as glasses. Moreover, the spin parameters are very different from those measurements for O_2^- trapped in bulk $Ca(OH)_2$ [114]. This discrepancy leads us to suppose that this center is trapped near the surface or in a less crystalline zone.

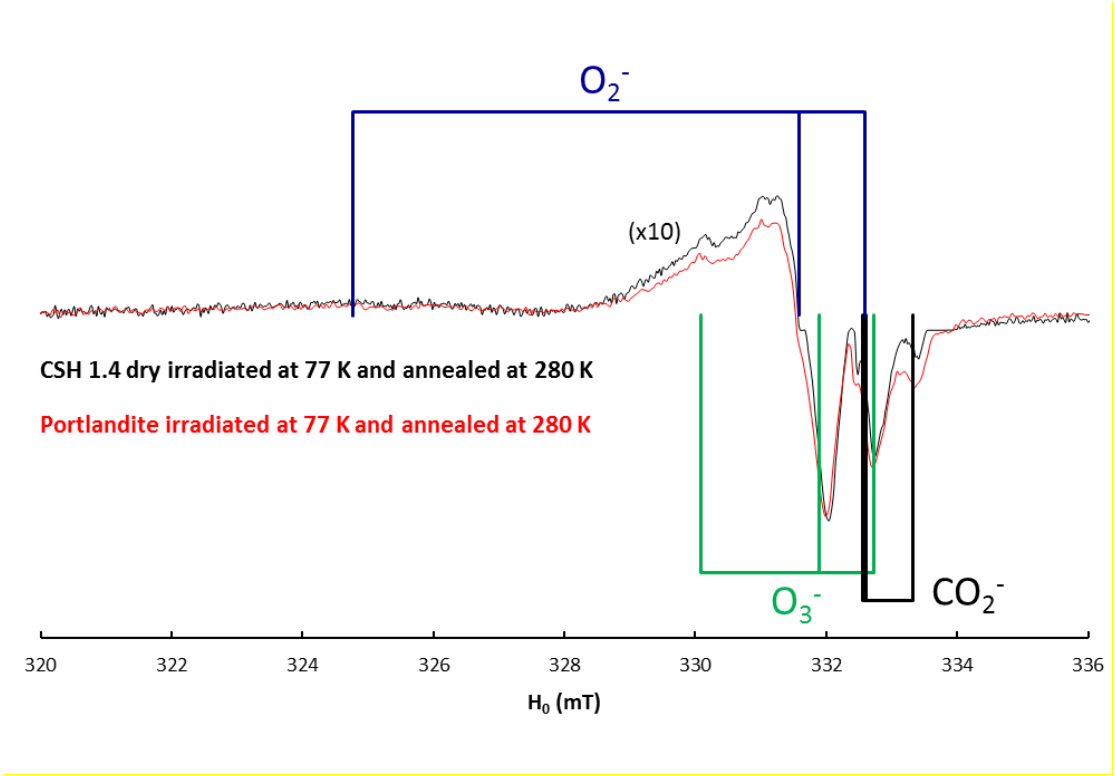

Figure 3. 26. Comparison of the EPR spectra of 1.30 C-S-H (blue curve) and portlandite (red curve) irradiated at 77 K and annealed at 280 K. The spectra were recorded at 100 K.

CHAPTER 4: Molecular hydrogen production from C2S/ C3S hydrates and synthetic portlandite

This section presents preliminary results of radiolytic hydrogen yields from irradiated. In the presence of water, the silicates (C2S and C3S) form products of hydration: C-S-H and portlandite. The purpose of this section is to compare the H_2 gas production of C-S-H and synthetic portlandite with that obtained in C2S and C3S hydrates, mainly to examine if energy transfers exist between different phases in cement matrix. Finally, samples irradiated with electron beam were analysed using EPR spectroscopy to identify radiolytic induced defaults (RID) and the associated yields.

4.1. Characterization

4.1.1. Sample chemical composition

The pH and Ca^{2+} concentration of the solutions (Table 23) indicate the final C/S ratio is around 1.6, as suggested in the literature review chapter (see Figure 1.4 and Figure 1.12).

Table 23. Calcium concentrations and pH in solution of C2S and C3S samples.

Samples	$[Ca^{2+}]$ in solution (mmol/L)	pH
C2S hydrates	26.1	12.64
C3S hydrates	24.4	12.53

4.1.2. The purity of C2S/C3S hydrates and synthetic portlandite samples

The XRD pattern of the synthetic portlandite at RH 85% is shown in Figure 4. 1. The result shows that portlandite is the only phase present in synthetic portlandite, while commercial portlandite contains calcite.

The results of XRD analysis of the C2S hydrates sample are shown in Figure 4. 1. Portlandite crystals ($Ca(OH)_2$), tobermorite and unhydrated C2S can be observed. The amount of portlandite and C-S-H is deduced from the combination of solution analysis and theoretical calculation, which is presented in the ANNEX 6.

In the case of C3S hydrates, XRD results suggest the presence of portlandite and C-S-H. Unhydrated C3S no longer exists or maybe present just little amounts, consequently complete reaction is assumed.

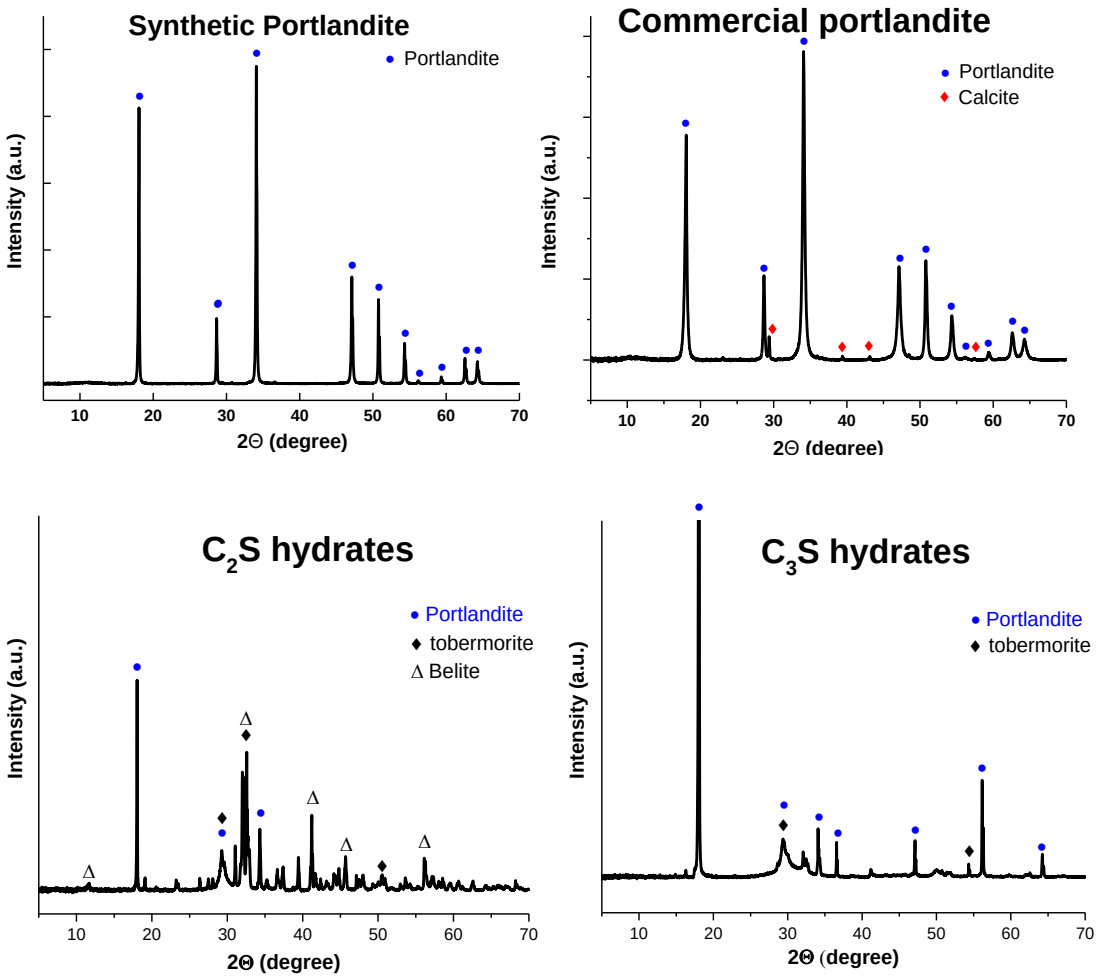

Figure 4. 1. Powder XRD patterns of the synthetic/ commercial portlandite and C2S/ C3S hydrates at RH 85%.

Quantification of water and impurities

Figure 4. 2 shows the thermogram of C2S hydrates. The thermograms of other samples are not presented because all the TGA analyses showed extremely similar curves as C-S-H. Quantification of the different components in C2S, C3S, portlandite and C-S-H is summarized in the Table 24.

.

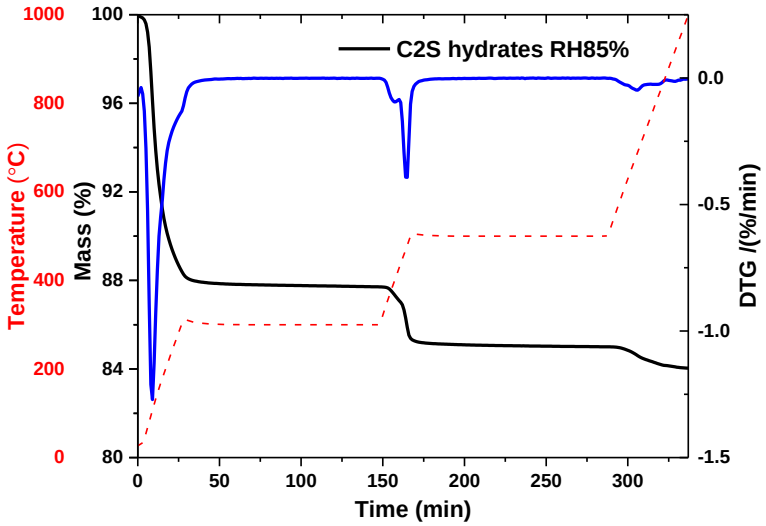

Figure 4. 2. TG and DTG curve of C2S hydrates at RH 85%.

Table 24. Summary of water content, portlandite, calcite, unreacted reactant and CSH content in the case of C2S/ C3S hydrates, synthetic/ commercial portlandite and 1.40 CSH at 85% RH. The relative uncertainty of water content, portlandite and calcite is estimated to be 10%.

Samples	RH	Water content (%)	Portlandite (%)	Calcite (%)	Unreacted reactant (%)	CSH content (%)
C2S hydrates	85%	11.5	6.2	1.7	31	61.1
C3S hydrates	85%	18.6	27	2.8	0	70.2
Synthetic portlandite	85%	0.4	98	1.3	0	0
Commercial portlandite	85%	2.0	95.0	3.1	0	0
1.40 CSH	85%	20.8	3.0	2.6	0	94.4

4.1.3. Porosity and specific surface area

For different samples, the isotherms were all type-IV according to IUPAC, which is characteristic of a mesoporous material [136]. Therefore, only isotherms from C3S hydrates were presented as an example (Figure 4. 3). The type H3 hysteresis loops are typically given by non-rigid aggregates of plate-like particles (e.g., certain clays).

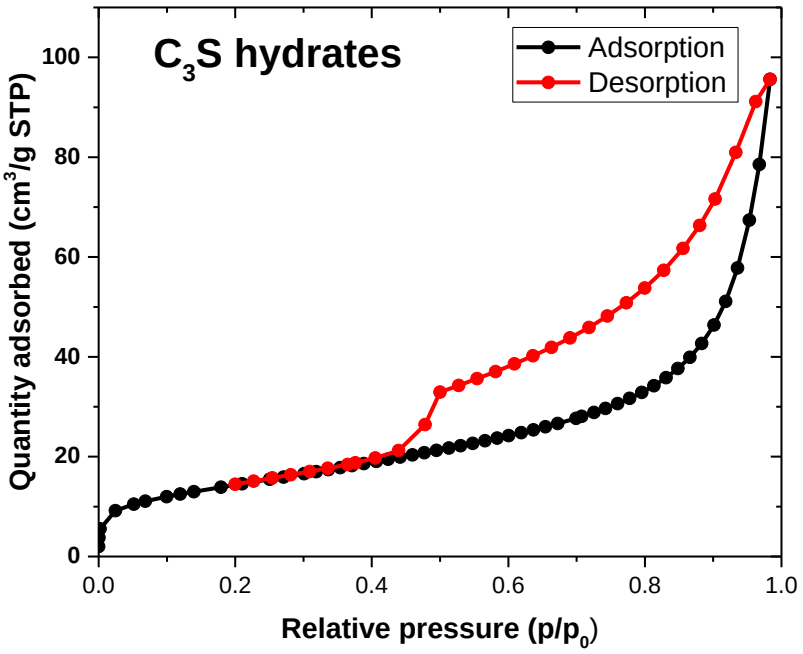

Figure 4. 3. Nitrogen adsorption/desorption isotherms of C3S hydrates sample.

Table 25. Surface area from BET theory of Analysed C2S/ C3S samples and synthetic portlandite measured from Nitrogen adsorption volumetry.

Samples	S_{BET-N2} (m^2/g)
C2S hydrates	58.1
C3S hydrates	52.0
Synthetic portlandite	8.9
1.40 CSH	183

Synthetic portlandite has the lowest specific surface area which is 8.9 m^2/g. From the previous reports, the BET surface areas of $Ca(OH)_2$ was 5.5 m^2/g [137] and 16 m^2/g [138]. The variations in the values could be according to individual differences in material source and treatment.

4.2. Hydrogen production

The radiolytic yields deduced from the slope of the curves of the gas production as a function of dose, for each sample (C2S hydrates RH 85%, C3S hydrates RH 85%, 1.40 C-S-H RH 85%, Commercial portlandite ($Ca(OH)_2$) RH 85% and Synthetic portlandite ($Ca(OH)_2$) RH 85%), are summarized in Table 26. The yields are calculated with respect to the total mass of material and water, which corresponds to the fact that energy is deposited in the whole system.

For comparison, Möckel [139] obtained a yield varying from 0.13 to 0.33 10^{-7} $mol.J^{-1}$ for a pure Portland cement paste. Our yield values of C2S/ C3S hydrates are in good consistency with his results.

The comparison of our results obtained on commercial portlandite sample with those reported by Laverne [90] shows a good agreement.

Table 26. Hydrogen radiolytic yields released from Gamma irradiated samples at room temperature. The error bars of samples are estimated to be 15%. Comparison with the literature.

Samples	**Water content (from ambient to 300°C) (%)**	**$G(H_2)$ ($mol/J\times10^{-7}$) (calculated with respect to the total energy received by the system)**
C2S hydrates RH 85%	11.5	0.19±0.03
C3S hydrates RH 85%	18.6	0.29±0.04
1.6 C-S-H RH 85%	20.8	0.35±0.05
Commercial portlandite ($Ca(OH)_2$) RH 85%	2.0	0.23±0.03
Synthetic portlandite ($Ca(OH)_2$) RH 85%	0.4	0.09±0.01
Portland cement paste	Not known.	0.13-0.33 [139]
$Ca(OH)_2$	Not known. (Baked at 100°C for 24 hours)	0.21 [90]

For comparison, the expected H_2 radiolytic yield of C2S and C3S hydrates is given by the equation considering if there is no interaction (energy transfer) between different phases in C2S and C3S hydrates.

The additive law is given by the relation:

$$G(H_2)_{calc} = \sum_i G_i\,(H_2) \times \nu_i \qquad (23)$$

Where i represents each phase of C3S and C2S and ν, the mass fraction.

The theoretical results (see Table 27) were obtained using the values presented above.

From Table 27, it is noticeable that the calculated values are quite close to the experimental results, below the uncertainty. This is an interesting outcome; these results infer that there are no energy transfer between portlandite and C-S-H in C3S and C2S hydrates.

Table 27. Experimental and theorical hydrogen radiolytic yields of C2S and C3S hydrates at room temperature.

Samples	**Experimental $G(H_2)$ (mol/J×10^{-7})**	**Calculated $G(H_2)$ (mol/J×10^{-7})**
C2S hydrates RH 85%	0.19±0.02	0.22±0.03
C3S hydrates RH 85%	0.29±0.03	0.27±0.03

4.3. Radiation-induced defects

In this section, EPR spectra of C2S/C3S hydrates and portlandite samples from electron beam irradiation have been measured and will be discussed. The study of Radiation-Induced Defects (RID) is developed.

4.3.1. C2S/ C3S hydrates

In order to give a general idea of paramagnetic centers formed after irradiation, EPR spectra of irradiated C3S/ C2S were done at 30 kGy.

4.3.1.1. C3S hydrates

The ESR spectrum of C3S irradiated at 77K and recorded at 100 K displays a doublet due to H atoms and two signals attributed to RID. From a comparison of our spectrum and the literature [132] [133], we suggest there is are several site of H atoms that can be observed in the spectrum. Therefore, the stability of H radicals is discussed in the following part.

4.3.1.1.1. H signal

Figure 4.4 presents the evolution of the EPR signal as a function of temperature. At 100 K, an anisotropic signal is observed and disappeared at 110K. At this temperature, a narrow component is superposed to an isotropic signal. Finally, another signal is observed at high field. The spin parameters are as followed:

H_I : g=2.024 ; A_{zz}=1418 MHz ; A_{yy}=1386 MHz ; A_{xx}=1353 MHz

H_{II} : g=2.028; A=1444 MHz

H_{III} : g~2.02 ; A=1429 MHz

H_{IV} : g~2.02 ; A=1287 MHz

The H atoms are trapped at least at four different sites. From literature [132] [140], H atoms trapped in tetragonal interstitials and hydroxyl groups and cations would be present in their nearest surrounding. The surrounding molecules are different. The hyperfine constant decrease when cations are present.

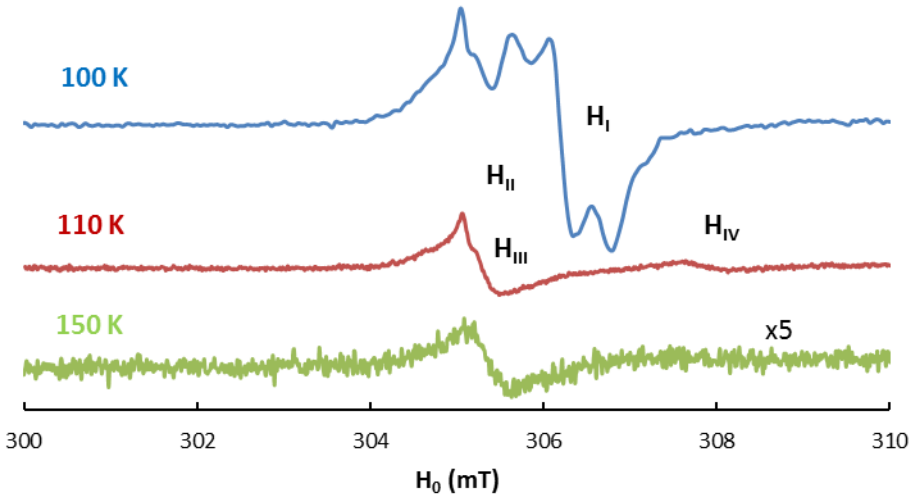

Figure 4. 4. EPR spectra of H signal of electron irradiated C3S hydrates at 77K and 30kGy recorded at 100K (blue), 110 K (red) and 150K (green).

In order to know the thermal stability of the H_{III} signals, isochrone annealing experiments were performed. Figure 4. 5 presents the evolution of the intensity of the signal as a function of the temperature. The intensity was corrected by temperature and normalized at 100 K:

$$C_{norm.}(T) = \frac{T \cdot I(T)}{100 \cdot I(100)} \tag{24}$$

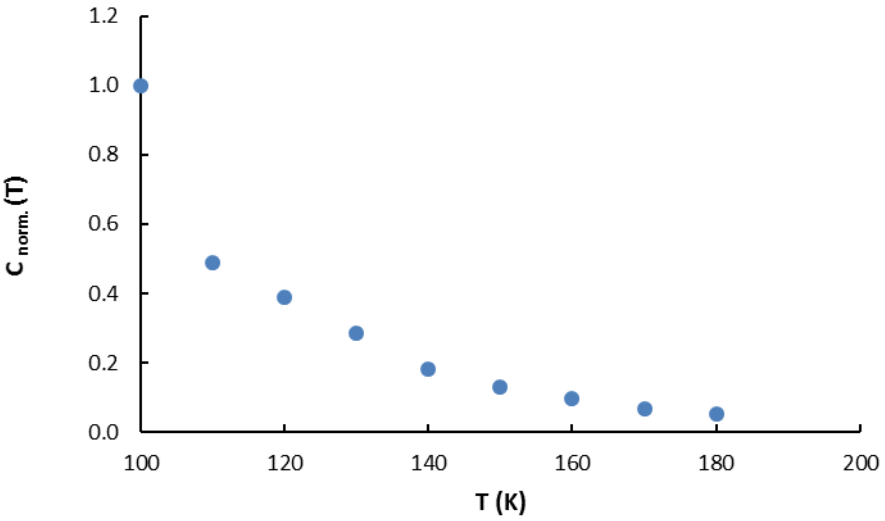

Figure 4. 5. The evolution of the intensity of the signal as a function of the temperature.

To interpret these results, we suppose that the disappearance of H_{III} follows either an order 1 law or an order 2 law. Let suppose that the initial and final temperature is T_1 and T_2 respectively, Δt represents the duration of the annealing. Moreover, we suppose this time is constant for all the temperature and we neglect the heating time to reach. Then we have:

$$C_{norm.}(T_2) = C_{norm.}(T_1) \cdot exp(-k \cdot \Delta t) \; or \frac{1}{C_{norm.}(T_2)} = \frac{1}{C_{norm.}(T_1)} + k \cdot \Delta t \qquad (25)$$

A typical Arrhenius plot of $-\Delta \ln\left(C_{norm.}(T_2)\right)$ and $\Delta(1/C_{norm.}(T_2))$ is presented in Figure 4. 6.

$$-\Delta ln\left(C_{norm.}(T_2)\right) = -ln\left(\frac{C_{norm.}(T_2)}{C_{norm.}(T_1)}\right) \qquad (26)$$

$$\Delta(1/C_{norm.}(T_2)) = \frac{1}{C_{norm.}(T_2)} - \frac{1}{C_{norm.}(T_1)} \qquad (27)$$

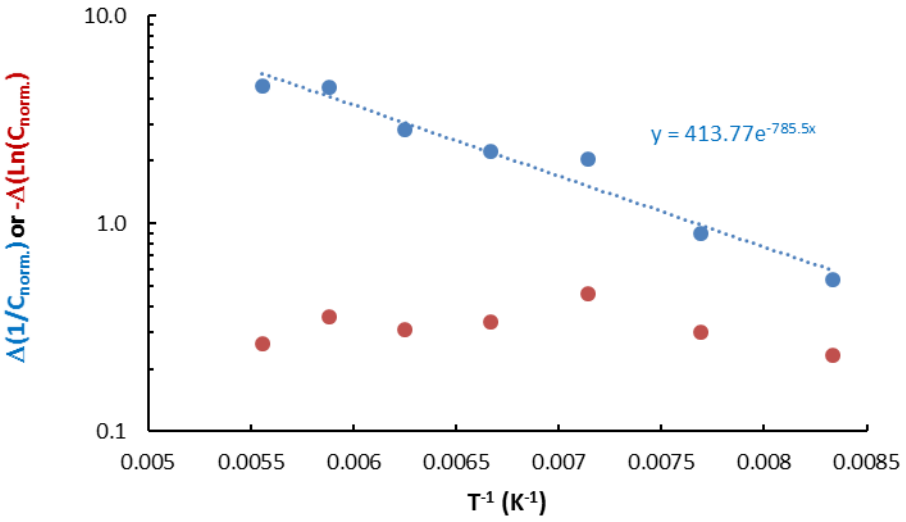

Figure 4. 6. Arrhenius plot of -Δln($C_{norm.}$ (T_2)) and Δ(1/($C_{norm.}$ (T_2)).

The Arrhenius equation is only valid in the case of an order 2 law (see Figure 4. 6). Then it suggests that the destruction of HIII is due to recombination:

$$H^{\cdot} + H^{\cdot} \rightarrow H_2 \qquad (28)$$

The activation energy (E_A) of this process deduced from the data is 6.5 kJ/mol approximatively.

4.3.1.1.2. RID signal

In addition to trapped H atoms, EPR spectrum of C3S irradiated at 77K is composed of different lines. The characteristic g values are specified in Figure 4. 7.

By the comparison with the spectrum of 1.40 C-S-H (see Chapter 3.3). The same signals are identified:

1) The anisotropic signal with $g_{xx} = g_{yy} = 2.074$ can be attributed to $O^{\circ -}$ center described by Barsova et al. [113] in $Ca(OH)_2$ (The blue line in Figure 4. 7 is a simulation using the spin parameters reported by the authors). As C3S contains portlandite, this hypothesis is valid.

2) A broad shoulder whose maximum is located around g=2.040. This shoulder reveals a broad distribution of g value. Similar distributions have been reported for hole centers trapped in alkali aluminosilicate or silicate glasses. We assign this to a $O^{\circ -}$ centre.

3) A central line centered around g=2.010.

4) A narrow singlet line with g=2.00285.

5) The high field signal corresponding to g=1.9956 reveals an anisotropic signal (called RID I). From the comparison with various published results, this signal is attributed either to O_2^- or peroxy radical (see Chapter 1.2.8.6).

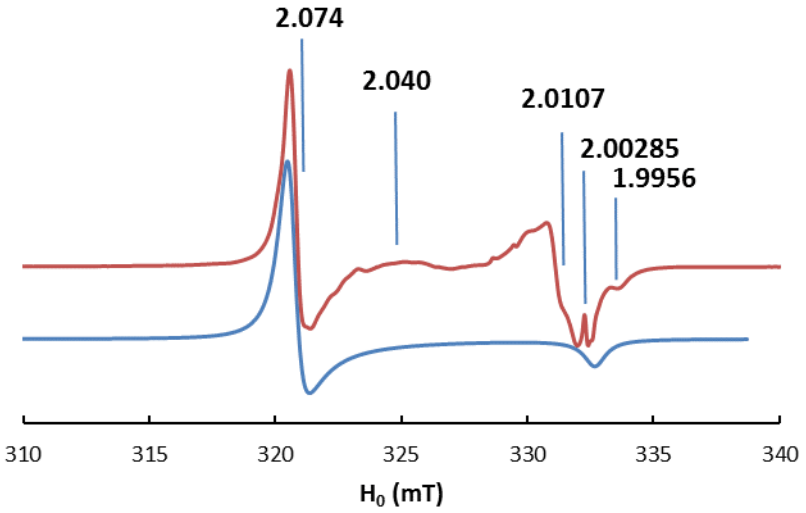

Figure 4. 7. EPR spectrum of C3S irradiated at 77K and recorded at 100K.

4.3.1.2. C2S hydrates

Figure 4. 8 presents the EPR signal of the C2S sample irradiated at 77 K and recorded at 100 K. We point out some differences:

H atoms signal is symmetric and more intense. The hyperfine coupling constant is 1423.7 MHz.

A hyperfine structure is superimposed to the broad line centered at g=2.010. The hyperfine pattern is rather complicated and the coupling constant is comprised between 0.5 and 0.7 mT. This value is close to those reported for $O^{\circ -}$ center bonded to aluminum atoms, for example in zeolite [102]. In fact, this signal could be the superposition of a six-lines and an eleven-lines (see Figure 4. 9, a stick plot is shown to precise the coupling) that may be attributed to centers bonded to one and two equivalent aluminum atoms, respectively [133]. There is no hyperfine structure observed in C3S sample (see Chapter 4.3.1.1.2), this may be explained as the aluminium content decreased in C3S sample, which has been suggested in Aluminium deficient zeolites by Vedrine [133].

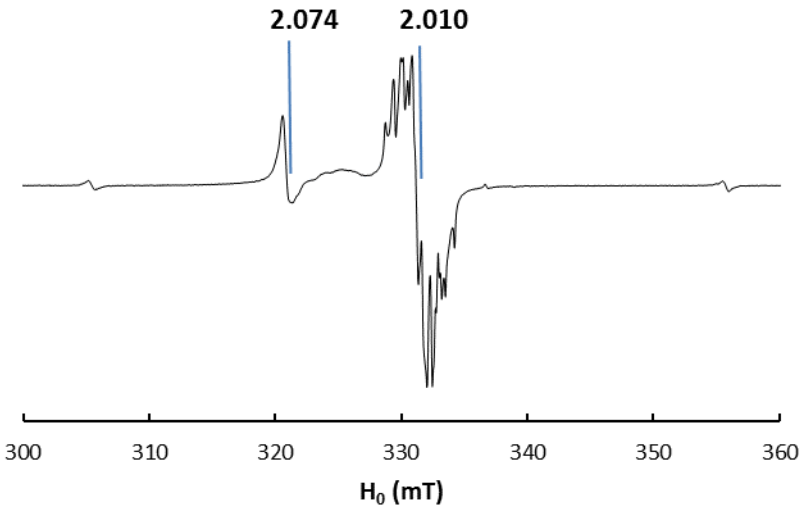

Figure 4. 8. The EPR spectrum of C2S sample irradiated at 77 K and recorded at 100 K.

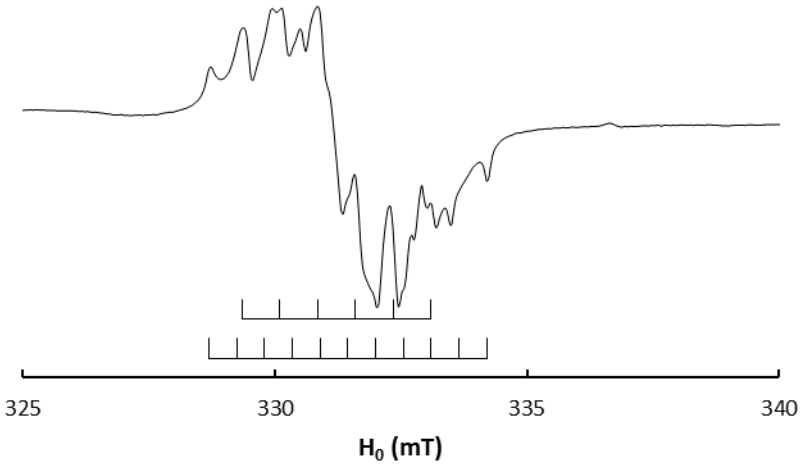

Figure 4. 9. Part of the EPR spectrum of C2S sample is displayed, showing the hyperfine peaks more clearly.

4.3.1.3. Comparison C3S and C2S

Table 28 shows the concentration of H and RID centers in electron irradiated C2S/ C3S samples at doses 30 kGy at 100K. The concentration of $O^{\circ-}$ centers associated with Portlandite is also given.

The ratio of the concentration of $O^{\circ-}$ centers in portlandite between C3S and C2S is close to 5. This value is close with the fraction of $Ca(OH)_2$ in C3S/ C2S determined by TGA techniques.

Table 28. The concentration of centers in electron irradiated C2S/ C3S samples at doses 30 kGy at 100K. The error bar is 35%.

	C3S	**C2S**
H atoms	$5.8\ 10^{15}$	$5.4\ 10^{15}$
$O^{\circ-}$ (portlandite)	$4.5\ 10^{17}$	$8.2\ 10^{16}$
RID	$1.6\ 10^{18}$	$1.7\ 10^{18}$
G(RID) (mol/J×10^{-7})	0.88	0.96

CHAPTER 5: Molecular hydrogen production from alkali salt uptake in C-S-H

This section presents preliminary results related to the effect of alkali (potassium/ sodium ions) and scavenger ions (NO_3^-) on H_2 gas production in calcium silicate hydrates. This was intended in order to observe the effect of impurities such as alkali ions, additional hydroxides or nitrates ions in C-S-H.

Materials were characterized in the same way described for C-S-H. Firstly, the solution composition was determined by ion chromatography, ICP-AES analysis and pH measurements. Secondly, TGA, XRD and BET were used to characterize the solid phases. Finally, samples were irradiated with gamma-rays to determine the radiolytic yields of hydrogen production.

5.1. Characterization

5.1.1. Sample chemical composition

The presence of alkali hydroxides raises the pH values, a key parameter in the system. For 0.8 C-S-H (see Table 29), the pH increases from 10.3-10.8 in nitrates system to 11.9-12.9 in the system containing hydroxide ions.

The results (see Table 29) show that the adsorption capacity of K^+ and Na^+ increases with the decrease of C/S ratio. For the same C/S ratio, the adsorption of K^+ and Na^+ gradually increases with the concentration of alkali solution. The adsorption of K^+ and Na^+ by C-S-H is related to the Ca^{2+} concentration in the solution (related to the pH of the alkali solution). At

high Ca/Si ratio, alkali adsorption was almost suppressed by high Ca^{2+} concentration. As a consequence, C-S-H samples at 1.6 C/S ratio were not used for further radiation study.

Table 29. Calculated composition of the synthesized phases. Measurement error: aqueous silicon, calcium, alkali ions and concentrations ±10%; pH ±0.1unit.

C-S-H composition			
Initial alkali concentration	**Ca/Si**	**([M+] / Si)**	**pH**
C/S = 0.8			
[NaOH]= 0.01M	0.8	0.017	12.5
[NaOH]= 0.05M	0.8	0.084	12.9
[KOH]= 0.01M	0.8	0.026	11.9
[KOH]= 0.05M	0.8	0.099	12.7
[$NaNO_3$]= 0.01M	0.79	0.010	10.7
[$NaNO_3$]= 0.05M	0.79	0.045	10.8
[KNO_3]= 0.01M	0.79	0.017	10.8
[KNO_3]= 0.05M	0.78	0.060	10.3
C/S = 1.6			
[$NaNO_3$]= 0.01M	1.45	0.001	12.6
[$NaNO_3$]= 0.05M	1.48	0	12.5
[KNO_3]= 0.01M	1.45	0.001	12.7
[KNO_3]= 0.05M	1.43	0	12.7

5.1.2. The purity of C-S-H samples with alkali sorption

The presence of alkali ions in C-S-H has a little influence on the solid formed. The experimental patterns show that all the samples present the diffraction peaks corresponding to the tobermorite structure [37][51] . Few small peaks are attributed to a small amount of portlandite and calcite. The presence of portlandite and calcite is quantified by TGA analysis in the following part (see Quantification of water and impurities section).

The XRD pattern of the C-S-H samples with KOH sorption are shown in Figure 5. 1. They are compared to a 0.80 C-S-H. Figure 5. 1 shows a 0.80 C-S-H with 12.7 Å interlayer distance. With the presence of K^+ ions, an increase of K ion concentration from 10 to 50 mM leads to a decrease of the interlayer distance from 11.9 to 10.9 Å. Interlayer distances are summarized in Table 30. This trend is only observed for alkali hydroxide samples, which is in good consistence with [141,142]. In the interlayer, the formation of ion bonds between deprotonated silanol groups and potassium or sodium ions instead of protons or calcium ions, leads to a smaller interlayer distance [124]. For alkali nitrates samples, a different trend is observed. Nevertheless, the reasons for these different observations on the role of anion on interlayer distance are unclear: it may be related to the effect of pH. Comparing to pure 0.8 C-S-H, pH was raised in the presence of alkali hydroxides while it was decreased in the presence of alkali nitrates.

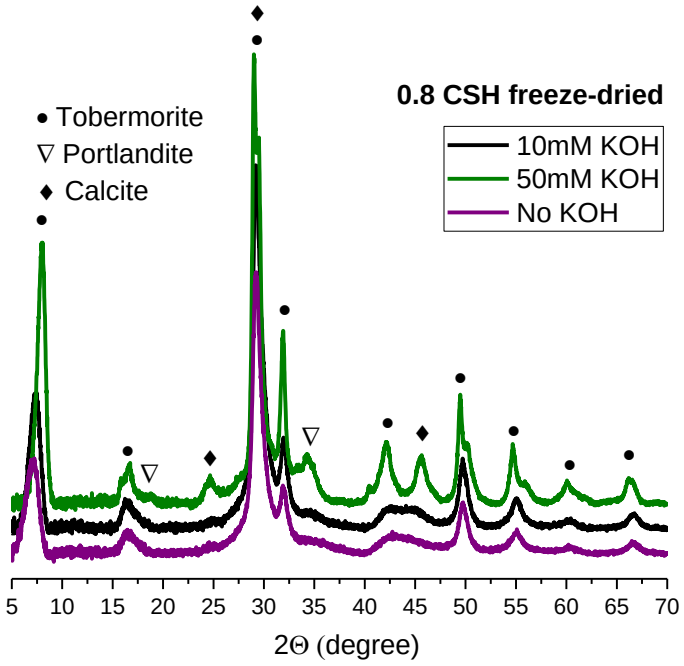

Figure 5. 1. Powder XRD patterns of C-S-H (C/S ratio =0.8) equilibrated with KOH solutions of increasing concentration (10mM and 50mM) or with an alkali-free solution (C-S-H).

Table 30. Summary of the interlayer distance of 0.8 C-S-H with/ without alkali sorption. The error on the d001 value is estimated at 0.5 Å [121].

Alkali salt	**$[M^+]/[Si]$**	**pH**	**Interlayer distance (Å)**
$NaNO_3$	0.010	10.7	12.7
	0.045	10.8	12.7
KNO_3	0.017	10.8	13.3
	0.060	10.3	13.5
NaOH	0.017	12.5	11.9
	0.084	12.9	11.9
KOH	0.026	11.9	11.9
	0.099	12.7	10.9
0.8 CSH	0	11.3	12.7

Quantification of water and impurities

Figure 5. 2 shows the thermogram of C-S-H samples with alkali sorption. They are compared to the 0.8 C-S-H thermogram. In all cases, the thermograms showed extremely similar curves as 0.8 C-S-H. Parameters are summarized in the Table 31. For all alkali-CSH, a small quantity of portlandite/ calcite is observed as it has already found in pure C-S-H samples.

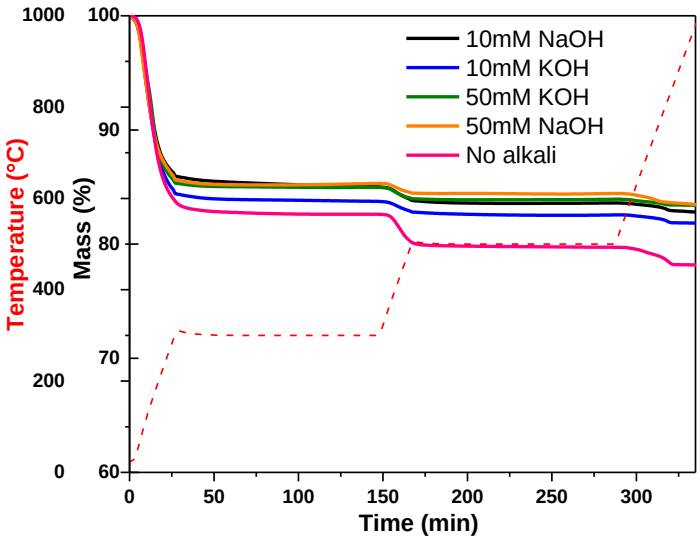

Figure 5. 2. TGA curves of C-S-H (C/S ratio =0.8) equilibrated with NaOH/ KOH solutions of increasing concentration (10Mm and 50mM) or with an alkali-free solution (C-S-H).

Table 31. Summary of the amount of water content (from 25 to 300 ℃, portlandite and calcite in the case of 0.8 C-S-H samples with/ without alkali sorption. The relative uncertainty of water content, portlandite and calcite is estimated to be 10%.

Samples	RH	Water content (%)	Portlandite (%)	Calcite (%)
10mM NaOH	3%	13.8	1.6	1.4
10mM KOH	3%	15.1	2.3	0.7
50mM NaOH	3%	14.1	2.6	0.7
50mM KOH	3%	14.4	1.9	0.7
10mM $NaNO_3$	3%	14.3	2.0	1.2
10mM KNO_3	3%	14.0	1.4	1.9
50mM $NaNO_3$	3%	14.2	1.9	2.1
50 mM KNO_3	3%	13.9	1.2	1.4
No Alkali	3%	16.1	3.2	1.5

5.1.3. Porosity and specific surface area

For all samples, the isotherms were all type-IV according to IUPAC, which is characteristic of a mesoporous material [136]. Therefore, only isotherms from 50 Mm $NaNO_3$ 0.8 CSH were presented as an example (Figure 5. 3). The type H3 hysteresis loops are typically given by non-rigid aggregates of plate-like particles (e.g., certain clays).

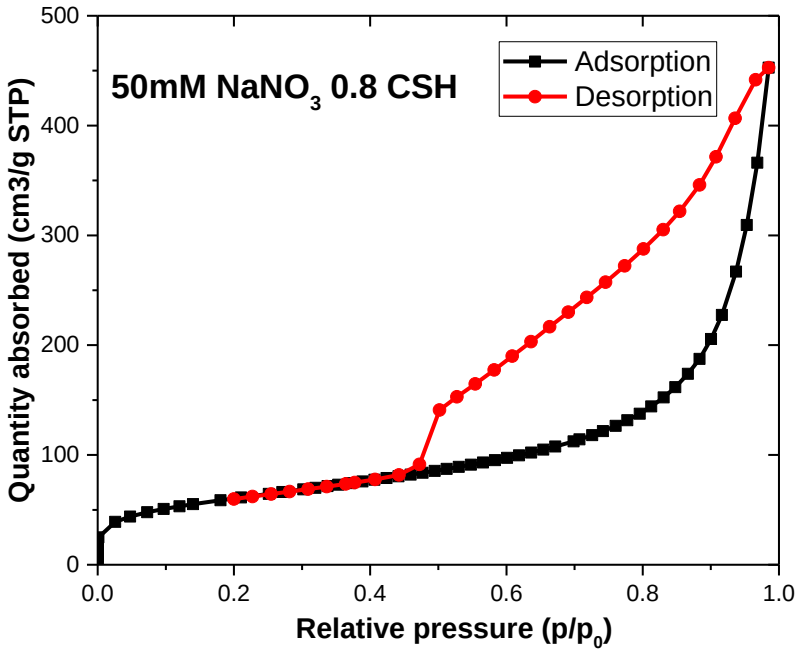

Figure 5.3. Nitrogen adsorption/desorption isotherms of 50mM $NaNO_3$ 0.8 C-S-H sample

In Table 32, results are compared to 0.80 C-S-H pristine. For alkali hydroxide samples, the specific surface area values are comprised between 152 and 169 m^2/g, these values are lower than that of pure 0.80 C-S-H (226 m^2/g). No significant difference is observed on SSA by varying alkali concentration. In contrast, for CSH with nitrates samples, the specific surface area didn't change for $NaNO_3$ samples, while the values decrease from 226 m^2/g (pure 0.8 CSH) to 167 and 177 m^2/g for KNO_3 samples. This reveals that SSA is affected by the alkali uptake, which depends also on the nature of the anion: hydroxide or nitrate.

Table 32. Surface area from BET theory of 0.8 C-S-H sample measured from Nitrogen adsorption isotherms.

Alkali salt	**$[M^+]/[Si]$**	**pH**	**Specific surface area (m^2/g)**
$NaNO_3$	0.010	10.7	220
	0.045	10.8	214
KNO_3	0.017	10.8	167
	0.060	10.3	177
NaOH	0.017	12.5	157
	0.084	12.9	169
KOH	0.026	11.9	160
	0.099	12.7	152
0.8 CSH	0	11.3	226

5.2. H_2 production from alkali-C-S-H

The production of H_2 from freeze-dried alkali-C-S-H samples, irradiated using gamma rays at a dose ranging between 100 and 200 kGy is proportional to the dose except for 50 mM NaOH sample. Thus, this data set has been ignored and should be reproduced.

The radiolytic yields deduced from the slope of the different curves are summarized in Table 33. Each gamma test was done on a separate sample and the uncertainties considered are that related to experimental errors.

Table 33. Hydrogen radiolytic yields released from Gamma-rays irradiated alkali-C-S-H samples at room temperature. The experimental error on $G(H_2)$ are estimated to be 15%.

Samples	**$G(H_2)$ ($mol/J\times10^{-7}$)** **(calculated with respect to the total energy received by the system)**
50mM $NaNO_3$ 0.8 C-S-H	0.016±0.002
10mM NaOH 0.8 C-S-H	0.61±0.09
10mM KOH 0.8 C-S-H	0.26±0.04
50mM KOH 0.8 C-S-H	0.38±0.06
0.8 C-S-H	0.52±0.08

Concerning hydrogen production in alkali-hydroxide-C-S-H samples (see Table 33), the sodium samples released the same magnitude hydrogen gas as that in 0.80 C-S-H pristine sample. We observe a significative effect of potassium that is difficult to interpret from structural data. In contrast, alkali-nitrate-C-S-H produce much less hydrogen 30 times lower than that of pure 0.80 C-S-H, even if nitrates are known to reduce the production of radiolytic hydrogen of bulk water [23,143], the drop of H_2 production is much weaker in bulk water [143] and in C3A free Portland cement pastes [23] than in 0.80 C-S-H. EPR experiments may be interesting in order to investigate the different mechanisms involved.

DISCUSSION

On the basis of the previous results, the mechanisms of hydrogen production in C-S-H are discussed in this section.

✓ Let's recall the absolute $G(H_2)$ in the C-S-H system:

The $G(H_2)$ values are presented in Figure 3. 17 as well as the value of primary $G(H_2)$ of bulk water and other similar systems [18,23,70,95,99,144], while the comparison among different systems is rather complex because different radiation sources were used. As it was described in Chapter 3.2.1, Figure 6.1 shows C-S-H produce the same quantity as an equivalent mass of bulk water. This result indicates very efficient H_2 production from C-S-H itself. This result highlights a great efficiency of the lysis of the structural –OH groups and of the recombination of hydrogen atoms.

The $G(H_2)$ of C-S-H is very close to $G(H_2)$ of cement paste S3 (S3 is mainly composed of C-S-H, about 93%) reported by Le Caer [18].

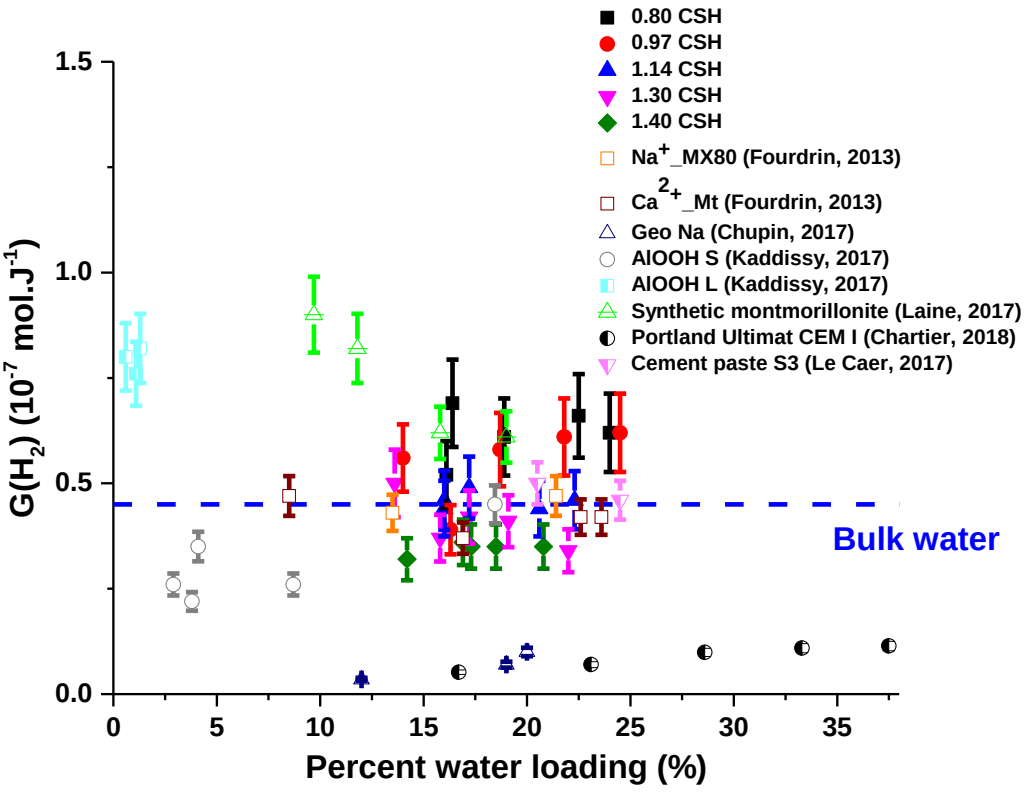

Figure 6. 1. Hydrogen production from C-S-H with respect to water loading. Black dotted line (primary radiolytic yield of liquid water). Yields standard deviations are estimated to be 15% for all samples.

Let's recall no O_2 production was observed during the gas measurements, but it is possible O_2 is produced and is still trapped in the structure. The global mechanism could be proposed as:

$$ROH \xrightarrow{ionizing\ radiation} RID + H_2 \quad (29)$$

This mechanism can be proposed based on the absence of oxygen and on the relative values of G(RID) and G(H_2). (Table 34). The question of the relative proportion of RID and H_2 is complex. Considering that G(RID) comprises mainly $O°^-$ (trapping of one hole on HO^-), we are not far from the stoichiometry. In this discussion we will rather use the notation RO° to take also into account the atom connected to the oxygen.

Table 34. The concentration of H atoms and RID and the corresponding radiation yields in different electron irradiated samples at doses 30 kGy (except 1.4 CSH, at dose 15kGy) at 77K, the experimental accuracy is estimated to be ±35%.. Hydrogen radiolytic yields released from Gamma irradiated CSH samples at room temperature are recalled, the experimental accuracy is estimated to be ±15%.

C/S ratio	**0.80**	**0.97**	**1.14**	**1.30**	**1.40**
H atoms (/g)	$1.3\ 10^{16}$	$2.0\ 10^{16}$	$5.4\ 10^{15}$	$8.5\ 10^{15}$	$4.4\ 10^{15}$
RID (/g)	$1.4\ 10^{18}$	$1.6\ 10^{18}$	$1.5\ 10^{18}$	$5.4\ 10^{17}$	$1.4\ 10^{18}$
G(RID) (mol/J×10^{-7})	0.81	0.89	0.82	0.60	0.81
G(H_2) (mol/J×10^{-7}) **(calculated with respect to the total energy received by the system)**	0.52	0.56	0.46	0.50	0.32

Moreover, in bulk water, $G(hole^+)$ (5×10^{-7} mol/J) with $G(H_2)$ (0.45×10^{-7} mol/J), while in C-S-H, G(RID at low temperature) is around 0.8×10^{-7} mol/J and $G(H_2)$ equal to 0.5×10^{-7} mol/J.

From these observations, we can deduce that the initial energy deposition process is less efficient in C-S-H than in water. This is quite surprising, as it was found to be more efficient in other hydroxides [70].

✓ Then the following mechanism could be suggested:

$$ROH \xrightarrow{ionizing\ radiation} R - O^{\circ} + H^{\circ} \quad (30)$$

H°, observed by EPR spectroscopy, is certainly the precursor of H_2. RO° is observed as RID.

H° intermediate in H_2 production has already been observed in other hydroxides like Aluminum hydroxide [91], Hydrated Layered Double Hydroxides [145], Synthetic Talc [146], montmorillonite and synthetic saponite [99].

According to the recombination of reactions previously described in Chapter 4.3.1.1.1.:

$$H^{\circ} + H^{\circ} \rightarrow H_2 \quad (31)$$

As the initial energy deposition process are less efficient than in water, but the final H_2 production is still high, this recombination processes leading to H_2 production must be very efficient. The most straightforward explanation is that RID are trapped whereas H atom can diffuse very easily.

This reaction is indeed already very active at low temperature, as shown by the much lower concentration in H atoms than in RID (Table 34).

The anions present in C-S-H will add an extra degree of complexity as it was described in Talc [146].

✓ Let's recall the $G(H_2)$ and $G(O_2)$obtained with NO_3^- to evaluate the effect of NO_3^- ions:

Table 35. Radiolytic yields $G(H_2)$ and $G(O_2)$ of irradiated CSH with and without NO_3^- using gamma rays (calculated with respect to the total energy received by the system).

Samples	**$G(H_2)$ (mol/J×10^{-7})** (calculated with respect to the total energy received by the system)	**$G(O_2)$ (mol/J×10^{-7})** (calculated with respect to the total energy received by the system)
50mM $NaNO_3$ 0.8 C-S-H	0.016±0.002	0.0036±0.0005
0.8 C-S-H	0.52±0.08	Not significant

The influence of nitrate on hydrogen production is very significant. Indeed, a drop of factor 30 is observed in Table 35 in the presence of sodium nitrate. The drop of H_2 production is weaker in cement pastes of Portland ultimate (about a factor 5) according to [23] than in C-S-H, but it is also present and significant. The production of O_2 is known to come from the direct radiolysis of nitrate ions [147-149] as proposed in Equation 32 and Equation 33:

$$NO_3^- \xrightarrow{ionizing\ radiation} NO_3^{-\circ} \rightarrow NO_2^- + O_2 \quad (32)$$

$$NO_3^- + O \rightarrow NO_2^- + O_2 \quad (33)$$

By analogy with the work done in aqueous solution [150], the following reactions can be expected:

$$NO_3^- + e_{aq}^- \rightarrow NO_3^{2-} \quad (34)$$

$$NO_3^{2-} + H_2O \rightarrow NO_2^{\circ} + 2OH^- \quad (35)$$

The identification of the radical species NO_3^{2-} by EPR spectroscopy at low temperature must be further developed.

The smaller H_2 radiolytic yield measured can be explained by an electron or Hydrogen atom scavenging by NO_3^-, as it was suggested in portland cement by [23]. Considering the reaction kinetic constant from NIST Chemical Kinetics [151], it seems NO_3^- do not scavenge efficiently H atoms, but NO_3^- scavenge electrons. Based on this finding, by analogy with other hydroxide containing nitrate [145], we can suppose during the irradiation, an electron/ hole pair (e^-/ h^+) is formed, prior to H atom formation so the following mechanism is suggested:

$$ROH \xrightarrow{ionizing\ radiation} hole^+ + e^- \quad (36)$$

$$e^- + R-OH \rightarrow R-O^- + H^{\circ} \quad (37)$$

$$hole^+ + R-OH \rightarrow R-O^{\circ} + H^+ \quad (38)$$

This step can explain the low efficiency of the initial energy deposition process described above (low RID yield), as it adds a potential recombination pathway between electron and holes before RID formation. Other electrons scavenger ions (for example: Cd^{2+}, SeO_4^{2-}, $Cr_2O_7^{2-}$, MnO_4^{2-}, SO_4^{2-}, NO_2^-) or holes scavenger ions should be studied to verify our hypothesis.

✓ Additional reaction proposed in Chapter 3.3.3 must also be considered:

$$R - O^{\circ} + R - O^{\circ} \rightarrow R \cdots O_2^{2-} \cdots R \quad (39)$$

$$R \cdots O_2^{2-} \cdots R + hole^{+} \rightarrow R \cdots O_2^{-} \cdots R \quad (40)$$

✓ Finally, the mechanisms could be proposed as:

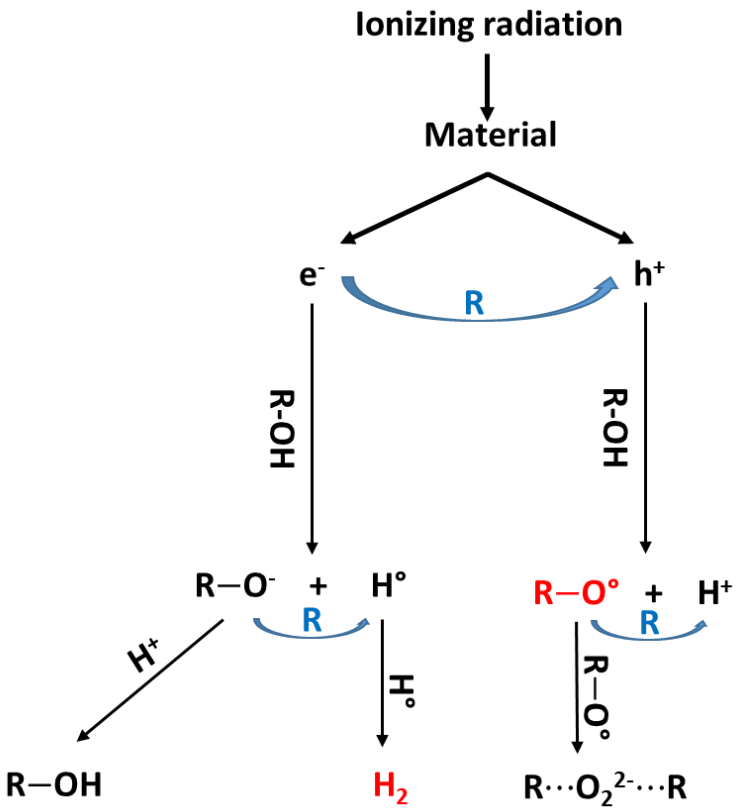

R: Recombination reaction process

- ✓ How can we interpret the LET effect (or absence of effect) within this scheme?

As it was discussed in Chapter 3.2.2, by comparing the results obtained using heavy ions (HI) with those obtained with gamma-rays irradiations (Table 36), $G(H_2)$ values obtained with HI irradiations are barely similar with gamma-rays irradiations (for example, for 0.8 CSH RH 85%, $G_{HI}(H_2) = 0.74\times10^{-7}$ and $G_{\gamma}(H_2) = 0.62\times10^{-7}$ respectively). This result suggests that no LET effect is observed in C-S-H with a low C/S ratio.

The equation 36-38 allows proposing an explanation for this observation. Indeed, LET effect is based on the difference in diffusion/recombination in tracks as a function of the radiation used. At low LET: diffusion is promoted, at high LET: recombination is promoted. The trapping of the hole as RID will abolish their diffusion and thus limit most recombination effects for them, irrespective of the radiation used, and amongst them, LET effects.

In C-S-H with a high C/S ratio (1.4 and 1.6 CSH), the difference of $G(H_2)$ suggests: a limited LET effect exists. This suggests an effect of Ca^{2+} ions on the H°-H° radicals recombination, but we cannot say if it acts by changing the structure of the material, or as suggested by Le Caer et al. [18], by trapping H atom, and thus, favouring their reaction with RID rather than with other H atoms.

Table 36. Radiolytic yields of irradiated samples using gamma rays and heavy ions (calculated with respect to the total energy received by the system).

samples	**$G_{HI}(H_2)$ (mol/J×10^{-7})** **(calculated with respect to the total energy received by the system)**	**$G\gamma(H_2)$ (mol/J×10^{-7})** **(calculated with respect to the total energy received by the system)**
0.8 CSH RH 85%	0.74±0.15	0.62±0.09
1.0 CSH RH 85%	0.69±0.14	0.62±0.09
1.2 CSH RH 85%	0.68±0.14	0.46±0.07
1.4 CSH RH 85%	0.69±0.14	0.34±0.05
1.6 CSH RH 85%	0.63±0.13	0.35±0.05
0.8 CSH RH 30%	0.56±0.11	0.69±0.10
1.2 CSH RH 30%	0.50±0.10	0.42±0.06
Bulk water	1.04	0.44

✓ How can we interpret the effect of water content:

The comparison of the raw $G(H_2)$ values of C-S-H with various C/S ratio cured at different RH (3%, 30%, and 60%) shows that an increase in the water content does not affect the raw $G(H_2)$, this result is in consistence with that obtained by EPR measurements which was presented in Chapter 3.3.2: G(RID) do not change with water content. The same trend was reported in Ca^{2+}_Mt system [144] and in Talc [146] where the raw $G(H_2)$ is almost constant for all RH. On the contrary, different tendencies were noticed in Na+_MX80, Na+_Mt, Geo-Na, Geo-K, Geo-Cs where the raw $G(H_2)$ increases with water content [144] [95].

This marginal role of the amount of water is traditionally interpreted through energy transfer phenomena from the solid to the liquid (see introduction part 1.2.8). However, in our case, we probably simply consider that the solid produces intrinsically as much hydrogen as the liquid that can adsorb.

✓ How can we interpret the effect of the C/S ratio within this scheme?

Let's recall the results were summarised in Table 18. At 30%, 60, 75 and 85% RH hydrogen production decreased in the order (except from 0.97 CSH at 30% and freeze-dried samples):

0.80 C-S-H > 0.97 C-S-H > 1.14 C-S-H > 1.30 C-S-H > 1.40 C-S-H

From Table 34, it can be observed that the creation of RID at low temperature seems independent of the C/S ratio. Therefore we can hypothesize that the difference observed for the final H_2 production can be attributed to the difference in recombination process or in back reaction of H_2 with RID for example.

In clays, the interlayer distance was a major parameter in controlling the H_2 production [126], with a nonmonotonous $G(H_2)$ evolution with this distance.

These structural variation (such as grain size, interlayer distance…) can obviously impact H atom diffusion.

However, the variation of C/S changes also the nature of the material itself, with Ca^{2+} ions increasing, changes in electronic densities or in bridging and non-bridging oxygens.

Sophie Le Caer et al. [18] studied cement paste and point out that the water-rich interlayer regions with Ca^{2+} ions act as electrons traps that promote the formation of H_2. But we don't have any evidence in our case that C-S-H hydrates richer in Ca^{2+} ions promote more efficiently H_2 formation.

✓ How can we interpret the effect of other cation impurities?

Chupin et al. reported the radiolytic yield in the hydrogen of geopolymers synthesized with different cations: sodium (Geo Na), potassium (Geo K) and cesium (Geo Cs) [95]. He shows that the electron density of the geopolymers may influence the variation of $G(H_2)$ values in Geo Na, Geo K, and Geo Cs.

In our case, $G(H_2)$ value in C-S-H with Na^+ impurities is very close to the $G(H_2)$ value of pristine C-S-H. However, when K^+ ions are introduced in C-S-H, the $G(H_2)$ value decreases. This could not be explained from an effect of the specific surface area because we observe a decrease of specific surface area in all C-S-H with impurities. As sodium and potassium CSH have a similar specific surface area, the evolution of $G(H_2)$ values cannot be related to the changes in the specific surface area (Table 37). While structural modifications could not be excluded between the different C-S-H with K^+ and Na^+ impurities, we could point out that the ionic radius of Ca^{2+} and Na^+ are similar, contrary to the ionic radius of K^+ which is a little bigger (Figure 6. 2.). If the ionic radius of K^+ is higher, the electron density in C-S-H with K^+ impurities may decrease, changing the energy deposition process.

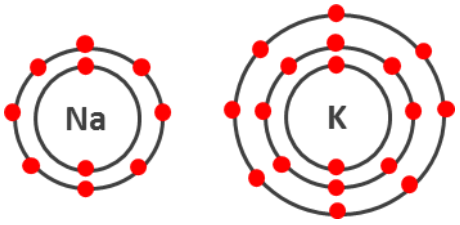

Figure 6. 2. Electronic configuration of Na^+ and K^+

In further work, it should be interesting to compare the electron interaction properties of these three materials by experimental measurements using TEM (for example using electron energy loss spectroscopy) or to perform EPR experiments to study the reaction mechanism of H atoms for example.

.

Table 37. Hydrogen radiolytic yields released from Gamma-rays irradiated alkali-C-S-H samples at room temperature. The experimental error on G(H2) is estimated to be 15%.

Samples	**$G(H_2)$ (mol/J×10^{-7})** **(calculated with respect to the total energy received by the system)**	**Specific surface area (m^2/g)**	**Ionic radius of the cation (pm)**
10mM NaOH 0.8 C-S-H	0.61±0.09	157	102
10mM KOH 0.8 C-S-H	0.26±0.04	160	138
50mM KOH 0.8 C-S-H	0.38±0.06	152	138
0.8 C-S-H	0.52±0.08	226	100

- ✓ Comparison our results with experimental values of cement paste from literature

Table 38 is taken from [18], which presents the different composition of cement pastes.

Table 38. The fraction of silicon atoms that belong to anhydrous phases containing silicon (alite, belite…), C-S-H and quartz, corrected from the relaxation effects. (Taken from [18]).

Samples	**S1-11%**	**S2-11%**	**S3-11%**
Anhydrous phases containing Si (%)	27	5	3
C-S-H (%)	73	40	93

The theoretical results (see Table 39) were calculated only by considering the contribution of C-S-H in the cement paste, using the values presented in Chapter 3.2.1.

From Table 39, it is noticeable that the calculated values are quite close to the experimental results from the literature [18], below the uncertainty. This is an interesting outcome; these results infer of quartz and of anhydrous phases present in the cement pastes does not impact H_2 production.

Table 39. Experimental and theoretical hydrogen radiolytic yields of cement paste at room temperature.

Samples	**Experimental $G(H_2)$ (mol/J×10^{-7})**	**Calculated $G(H_2)$ (mol/J×10^{-7})**
S1	0.26±0.03 [18]	0.26±0.04
S2	0.12±0.03 [18]	0.14±0.02
S3	0.46±0.05 [18]	0.52±0.08

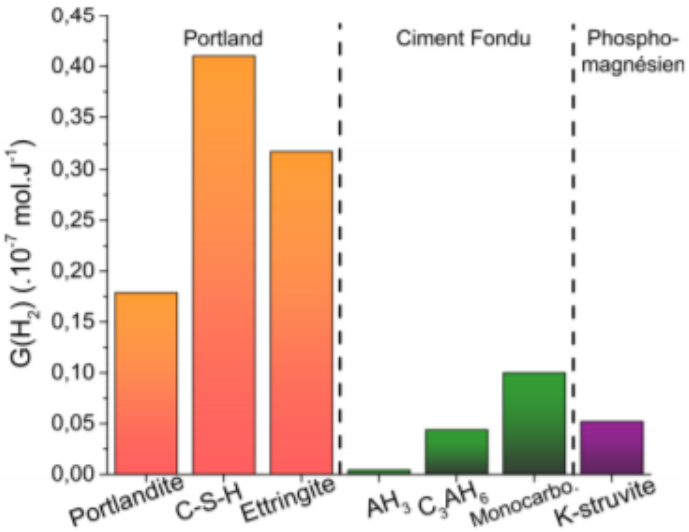

Figure 6. 3. Comparison of radiolytic yields $G(H_2)$ in mol J^{-1} obtained for Portland cement, calcium-aluminate cement(Cement Fondu) and Phospho-magnesium cement (taken from [15]

Comparison of the behavior of different types of cement was made by [15], among Portland cement, calcium-aluminate cement (Cement Fondu) and phospho-magnesium cement. The recorded values of radiolytic yields were considerably higher for Portland cement compared to the other types of cement which were governed by the nature of hydrates (Figure 6.). From our result, this behavior of Portland cement can be connected to large H_2 production from C-S-H under irradiation.

- ✓ The significance in the context of nuclear waste conditioning

Portland cement paste is mainly composed of C-S-H and portlandite. Although C-S-H produces a large amount of H_2, one strategy to mitigate this production would be to add NO_3^- into the Portland cement, which we proved to reduce hydrogen production significantly.

When cemented waste packages display a complex radiological inventory with fission (or activation) products and actinides (fuel clads, for example), as a consequence, there are different radiation field emitted, such as γ rays, β rays, and α rays. Let's recall in C-S-H, there is no LET effect, consequently, for alpha emitters, the $G(H_2)$ value is the same as for beta/ gamma emitters. This represents an advantage concerning the conditioning and the embedding of nuclear wastes with a major contribution of alpha emitters (such as ^{238}Pu and ^{239}Pu) in terms of safety evaluation. It means also that if we manage to use a strategy to mitigate H2 production under gamma rays, it will probably also be efficient under alpha irradiation.

CONCLUSION AND PERSPECTIVES

In France, the low and intermediate level wastes issued from the dismantling of nuclear facilities are usually conditioned in Portland cement to ensure the stability and the confinement of the radioactivity for disposal and future geological storage. However, ionizing radiations, due to nuclear wastes, lead to water radiolysis in these materials. Therefore, this study aimed to elucidate the behavior of C-S-H, the main hydrate of Portland cement, under ionizing radiation in order to allow us to understand the radiolytic mechanisms of hydrogen production.

For this purpose, different parameters known to influence directly on the radiolysis were investigated: the C/S ratio, water content, the presence of impurities (such as alkali ions, additional hydroxides or nitrates ions) and of the nature of the ionizing source (gamma rays and heavy ions (HI) beams). The existence of energy transfers between different main phases (C-S-H and portlandite) in cement hydrates has also to be explored, to get closer to real conditions. The radiolytic mechanisms of molecular hydrogen production under irradiation were studied using electron paramagnetic resonance (EPR) spectroscopy experiments at low temperature.

The irradiation of C-S-H with gamma rays show that the formation of H_2 is more efficient in low C/S ratio. However, the creation of RID at low temperature seems to be independent of the C/S ratio. Therefore we can hypothesize that the difference observed for the H_2 production can be attributed to the difference in recombination process or in back reaction of H2 with RID for example. Contrary to the general phenomena, where energy transfer phenomena occur from the solid to the liquid, in our case, we have here to consider that the solid itself produce intrinsically hydrogen. Moreover, hydrogen production is independent of the water content and C-S-H produces the same quantity as an equivalent mass of bulk water. These results indicate very efficient H_2 production from C-S-H and the strong recombination of reactive species (hydrogen atoms) in the materials. However, the presence of impurities as scavengers of the precursors of dihydrogen, like nitrates ions, can strongly hinder the H_2 production in C-S-H.

The comparison of the results obtained using heavy ions (HI) with those obtained with gamma-rays irradiations, suggests that no LET effect is observed in C-S-H with low C/S ratio.

The study of C3S and C2S hydrates infers that there is no energy transfer between the different phases (portlandite and C-S-H).

- Hydrogen production mechanisms

The different mechanisms highlighted in this thesis can be described in the following Figure 7.1. The primary step is the formation of an electron-hole pair by the interaction of the radiations ionizing with C-S-H. Then, the electron/hole pair formed will give rise to different reactions:

- The electron reacts to the structural hydroxyl groups. This reaction can lead to hydrogen radical formation which results in hydrogen gas production.
- The hole can react with the hydroxyl groups of the structure.
- The recombination of electron and hole.

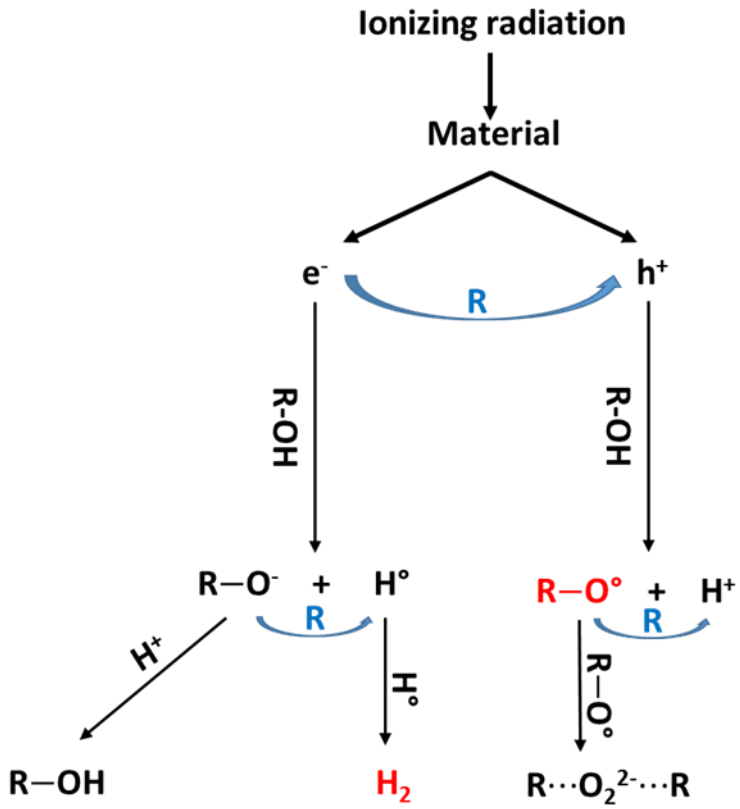

Figure 7. 1 The scheme summarizes the different reactions possible in the materials studied in this work.

R: Recombination reaction process

- Perspectives

From the results of the hydrogen production measurements, it would be important to assess the role of potassium on the H_2 gas production. For this purpose, EPR experiments at low temperature on Potassium-C-S-H must be performed to confirm our hypothesis. The role of impurities in the production of radiolysis gases is a parameter to be taken into account more in future work and their study needs to be further developed. For this purpose, C-S-H should be synthesized by varying more impurity types (Cd^{2+}, SeO_4^{2-}, $Cr_2O_7^{2-}$, MnO_4^{2-}, SO_4^{2-}, NO_2^-) and amounts to confirm and to generalize our hypothesis.

It would be interesting to evaluate the thermal stability of radiation-induced defects of Portlandite at low temperature on synthetic portlandite, as it is actually impossible to avoid precipitation of portlandite during C3S hydration. This would help to compare the H atoms in portlandite with that in C-S-H/ C2S/ C3S hydrates. Other interesting experiments would be the following of reactions in irradiated samples in real-time in order to detect the transient species that might be formed and recombined.

REFERENCES

[1] M. Lainé, PhD thesis, Université Paris-Saclay, 2017.
[2] M. Atkins, F.P. Glasser, Waste Management, Volume 12, 1992, pages 105-131.
[3] B. Bonin, M. Colin, A. Dutfoy, Journal of Nuclear Materials, Volume 281, 2000, pages 1-14.
[4] NDA, Waste Package Accident Performance Status Report, 2013, page 7.
[5] A. Hilal, Microstructure of Concrete, 2016, page 3.
[6] N.E. Bibler, Scientific Basis for Nuclear Waste Management, Springer, 1980, page 585.
[7] P. Bouniol, E. Bjergbakke, Journal of Nuclear Materials, 2008, page 1.
[8] H. Christensen, E. Bjergbakke, Radiolysis of concrete, 1984, page 32.
[9] B. Craeye, G. De Schutter, C. Vuye, I. Gerardy, Progress in Nuclear Energy, volume 83, 2015, page 212-219.
[10] F. Foct, M.-V. Di Giandomenico, P. Bouniol, EDP Sciences, volume 56, 2013, page 05002.
[11] C. Gallé, H. Peycelon, P. Le Bescop, S. Bejaoui, V. L'Hostis, B. Bary, P. Bouniol, C. Richet, Journal de Physique IV, volume 136, 2006, page 25.
[12] H.J. Möckel, R.H. Köster, Nuclear Technology, volume 59, 1982, page 494.
[13] K. Noshita, T. Nishi, M. Matsuda, MRS Online Proceedings Library Archive, volume 353, 1994, page 921.
[14] J. Stone, Scientific Basis for Nuclear Waste Management, 1979, page. 443.
[15] L. Acher, PhD thesis, Université Paris-Saclay, 2017.
[16] R.J.-M. Pellenq, A. Kushima, R. Shahsavari, K.J. Van Vliet, M.J. Buehler, S. Yip, F.-J. Ulm, Proceedings of the National Academy of Sciences, volume 106, 2009, page 16102.
[17] A.J. Allen, J.J. Thomas, H.M. Jennings, Nature materials, volume 6, 2007, page 311.
[18] S. Le Caër, L. Dezerald, K. Boukari, M. Lainé, S. Taupin, R.M. Kavanagh, C.S.N. Johnston, E. Foy, T. Charpentier, K.J. Krakowiak, R.J.M. Pellenq, F.J. Ulm, G.A. Tribello, J. Kohanoff, A. Saúl, Cement and Concrete Research, volume 100, 2017, page 110.
[19] R.C. Ewing, W.J. Weber, F.W. Clinard, Progress in Nuclear Energy, volume 29, 1995, page 63.
[20] L. Dezerald, J.J. Kohanoff, A.A. Correa, A. Caro, R.J.M. Pellenq, F.J. Ulm, A. Saúl, Environmental Science and Technology, volume 49, 2015, page 13676.
[21] P. Bouniol, B. Muzeau, V. Dauvois, Journal of Nuclear Materials, volume 437, 2013, page 208.
[22] J.A. Kaddissy, S. Esnouf, D. Durand, D. Saffre, E. Foy, J.-P. Renault, The Journal of Physical Chemistry C, volume 121, 2017, page 6365.
[23] D. Chartier, J. Sanchez-Canet, B. Laetitia, S. Esnouf, J.P. Renault, Journal of Nuclear Materials Volume 511, 2018, pages 183-190
[24] H.F. Taylor, Hydration of Portland cement, chapter 7, in Cement chemistry, 2nd edition, Thomas Telford, 1997, page 187.
[25] H.W. Taylor, Journal of the Chemical Society, 1950, page 3682.
[26] X. Cong, R.J. Kirkpatrick, Advanced Cement Based Materials, volume 3, 1996, page 144.
[27] E. Flint, J. Research NBS, volume 12, 1934, page 751.
[28] X. Lecoq, PhD thesis, University of Burgundy, 1993.
[29] P.S. Roller, G. Ervin Jr, Journal of the American Chemical Society, volume 62, 1940, page 461.
[30] M. Grutzeck, A. Benesi, B. Fanning, Journal of the American Ceramic Society, volume 72, 1989, page 665.
[31] S. Greenberg, T. Chang, Journal of Physical Chemistry, volume 64, 1965, page 1151-1157.
[32] A. Nonat, X. Lecoq, the Structure, Stoichiometry and Properties of C-S-H Prepared by C3S Hydration Under Controlled Condition, Chapter 14, in Nuclear magnetic resonance spectroscopy of cement-based materials, Springer, 1998, page 197.
[33] S. Grangeon, F. Claret, C. Lerouge, F. Warmont, T. Sato, S. Anraku, C. Numako, Y. Linard, B. Lanson, Cement and Concrete Research, volume 52, 2013, page 31.
[34] G. Renaudin, J. Russias, F. Leroux, F. Frizon, C. Cau-dit-Coumes, Journal of Solid State Chemistry, volume 182, 2009, page 3312.

[35] H.F. Taylor, Journal of the American Ceramic Society, volume 69, 1986, page 464.
[36] D.A. Kulik, Cement and Concrete Research, volume 41, 2011, page 477.
[37] I. Richardson, G. Groves, Cement and Concrete Research, volume 23, 1993, page 131.
[38] Courault, A.-C., PhD thesis, Université de Bourgogne, 2000.
[39] E. Bonaccorsi, S. Merlino, A.R. Kampf, Journal of the American Ceramic Society, volume 88, 2005, page 505.
[40] S. Hamid, Zeitschrift für Kristallographie-Crystalline Materials, volume 154, 1981, page 189.
[41] W.-S. Chiang, G. Ferraro, E. Fratini, F. Ridi, Y.-Q. Yeh, U. Jeng, S.-H. Chen, P. Baglioni, Journal of Materials Chemistry A, volume 2, 2014, page 12991.
[42] D. Winslow, S. Diamond, Journal of the American Ceramic Society, volume 57, 1974, page 193.
[43] J. Völkl, R. Beddoe, M. Setzer, Cement and Concrete Research, volume 17, 1987, page 81.
[44] R. Beddoe, K. Lang, Cement and concrete research, volume 24, 1994, page 605.
[45] D. Winslow, J.M. Bukowski, J.F. Young, Cement and Concrete Research, volume 25, 1995, page 147.
[46] A. Allen, C. Windsor, V. Rainey, D. Pearson, D. Double, N.M. Alford, Journal of Physics D: Applied Physics, volume 15, 1982, page 1817.
[47] J.J. Thomas, H.M. Jennings, A.J. Allen, Cement and Concrete Research, volume 28, 1998, page 897.
[48] A. Allen, R. Oberthur, D. Pearson, P. Schofield, C. Wilding, Philosophical Magazine B, volume 56, 1987, page 263.
[49] J.J. Thomas, A.J. Allen, H.M. Jennings, Journal of the American Ceramic Society, volume 91, 2008, page 3362.
[50] W.-S. Chiang, E. Fratini, P. Baglioni, D. Liu, S.-H. Chen, Journal of Physical Chemistry C, volume 116, 2012, page 5055.
[51] A. Nonat, Cement and Concrete Research, volume 34, 2004, page 1521.
[52] S. Grangeon, F. Claret, C. Roosz, T. Sato, S. Gaboreau, Y. Linard, Journal of applied crystallography, volume 49, 2016, page 771.
[53] C. Roosz, S. Gaboreau, S. Grangeon, D. Prêt, V. Montouillout, N. Maubec, S. Ory, P. Blanc, P. Vieillard, P. Henocq, Langmuir, volume 32, 2016, page 6794.
[54] L. Nachbaur, PhD thesis, University of Burgundy, 1997.
[55] H.M. Jennings, Cement and concrete research, volume 30, 2000, page 101.
[56] H.M. Jennings, Cement and Concrete Research, volume 38, 2008, page 275.
[57] I. Klur, B. Pollet, J. Virlet, A. Nonat, C-S-H Structure Evolution with Calcium Content by Multinuclear NMR, Chapter 8, in Nuclear magnetic resonance spectroscopy of cement-based materials, Springer, 1998, page 119.
[58] L. Dezerald, J.J. Kohanoff, A.A. Correa, A. Caro, R.J.M. Pellenq, F.J. Ulm, A. Saúl, Environmental Science & Technology, volume 49, 2015, page 13676.
[59] S. Bagosi, L. Csetenyi, Cement and concrete research, volume 28, 1998, page 1753.
[60] T. IWAIDA, S. NAGASAKI, S. TANAKA, T. YAITA, セメント・コンクリート論文集, volume 55, 2002, page 21.
[61] S.-Y. Hong, F. Glasser, Cement and Concrete Research, volume 29, 1999, page 1893.
[62] H. Stade, Cement and Concrete Research, volume 19, 1989, page 802.
[63] I. Lognot, I. Klur, A. Nonat, NMR and Infrared Spectroscopies of C-S-H and AI-Substituted C-S-H Synthesised in Alkaline Solutions, Chapter 13, in Nuclear magnetic resonance spectroscopy of cement-based materials, Springer, 1998, page 189.
[64] I. Jawed, J. Skalny, Cement and Concrete Research, volume 8, 1978, page 37.
[65] L. Black, C. Breen, J. Yarwood, K. Garbev, P. Stemmermann, B. Gasharova, Journal of the American Ceramic Society, volume 90, 2007, page 908.
[66] G.W. Groves, A. Brough, I.G. Richardson, C.M. Dobson, Journal of the American Ceramic Society, volume 74, 1991, page 2891.

[67] A. Mozumder, Interaction of Fast Charged Particles with Matter, Chapter 2, in Charged Particle and Photon Interactions with Matter, MARCEL DEKKER, 2004, page 9.
[68] L.H. Toburen, Ionization and Secondary Electron Production by Fast Charged Particles, Chapter 3, in Charged Particle and Photon Interactions with Matter, MARCEL DEKKER, 2004, page 31.
[69] J. W. T. Spinks and R. J. Woods, Water and inorganic aqueous systmes, Chapter 7, in An introduction in radiation chemistry, John Wiley &. Sons, Third Edition, 1990, page 243.
[70] J. Kaddissy, PhD thesis, Université Paris-Saclay, 2016.
[71] R.J. Woods, A.K. Pikaev, Introduction, Chapter 1, in Applied radiation chemistry: radiation processing, John Wiley & Sons, 1994, page 6.
[72] BUXTON, G. V., An overview of the radiation chemistry of liquids, Chapter 1, in Radiation chemistry, EDP sciences, 2012, page 3.
[73] J.A. LaVerne, R.H. Schuler, The Journal of Physical Chemistry, volume 87, 1983, page 4564.
[74] G. Auclair, PhD thesis, Université Paris 6, 2001.
[75] C. Ferradini, J.-P. Jay-Gerin, Research on Chemical Intermediates, volume 26, 2000, page 549-565.
[76] A. Allen, The Journal of Physical Chemistry, volume 52, 1948, page 479.
[77] A.O. Allen, C. Hochanadel, J. Ghormley, T. Davis, The Journal of Physical Chemistry, volume 56, 1952, page 575.
[78] A. Garibov, K.B. Gezalov, G. Velibekova, A. Khudiev, M.K. Ramazanova, R. Kasumov, T. Agaev, A. Gasanov, High Energy Chem.(Engl. Transl.), volume 21, 1988.
[79] N. Mikio, N.M. Masaki, Radiation Physics and Chemistry, volume 47, 1996, page 241.
[80] N.G. Petrik, A.B. Alexandrov, A.I. Vall, The Journal of Physical Chemistry B, volume 105, 2001, page 5935.
[81] J.A. LaVerne, L. Tandon, The Journal of Physical Chemistry B, volume 106, 2002, page 380.
[82] P. Rotureau, J. Renault, B. Lebeau, J. Patarin, J.C. Mialocq, ChemPhysChem, volume 6, 2005, page 1316.
[83] S. Le Caër, P. Rotureau, F. Brunet, T. Charpentier, G. Blain, J.P. Renault, J.C. Mialocq, ChemPhysChem, volume 6, 2005, page 2585.
[84] S. Le Caër, Water, volume 3, 2011, page 235.
[85] Y.D. Glinka, S.-H. Lin, Y.-T. Chen, Physical Review B, volume 62, 2000, page 4733.
[86] N. Brodie-Linder, S. Le Caër, M.S. Alam, J.P. Renault, C. Alba-Simionesco, Physical Chemistry Chemical Physics, volume 12, 2010, page 14188.
[87] J. Kaddissy, S. Esnouf, D. Saffré, J.-P. Renault, Journal of Hydrogen Energy, volume 44, 2019, Pages 3737-3743.
[88] M.L. Westbrook, R.L. Sindelar, D.L. Fisher, Journal of Radioanalytical and Nuclear Chemistry, volume 303, 2015, page 81.
[89] J.A. Kaddissy, S. Esnouf, D. Saffré, J.-P. Renault, International Journal of Hydrogen Energy, volume 44, 2019, page 3737.
[90] J.A. LaVerne, L. Tandon, The Journal of Physical Chemistry A, volume 109, 2005, page 2861.
[91] J. Kaddissy, S. Esnouf, D. Durand, D. Saffre, E. Foy, J.-P. Renault, The Journal of Physical Chemistry C, volume 121, 2017, page 6365−6373
[92] J.L. Provis, J.S.J. Van Deventer, Introduction to Geopolymers, Chapter 1, in Geopolymers : structure, processing, properties and industrial applications, CRC Press, 2009, page 1.
[93] D. Lambertin, F. Frizon, F. Bart, Surface and Coatings Technology, volume 206, 2012, page 4567.
[94] P. Duxson, J.L. Provis, G.C. Lukey, S.W. Mallicoat, W.M. Kriven, J.S. Van Deventer, Colloids and Surfaces A: Physicochemical and Engineering Aspects, volume 269, 2005, page 47.
[95] F. Chupin, A. Dannoux-Papin, Y.N. Ravache, J.-B.d.E. de Lacaillerie, Journal of Nuclear Materials, volume 494, 2017, page 138.
[96] T. Allard, E. Balan, G. Calas, C. Fourdrin, E. Morichon, S. Sorieul, Nuclear Instruments and Methods in Physics Research Section B: Beam Interactions with Materials and Atoms, volume 277, 2012, page 112.

[97] D. Gournis, A. Mantaka-Marketou, M. Karakassides, D. Petridis, Physics and Chemistry of Minerals, volume 28, 2001, page 285.
[98] D. Gournis, A. Mantaka-Marketou, M. Karakassides, D. Petridis, Physics and Chemistry of Minerals, volume 27, 2000, page 514.
[99] M. Laine, E. Balan, T. Allard, E. Paineau, P. Jeunesse, M. Mostafavi, J.L. Robert, S. Le Caer, RSC Advances, volume 7, 2017, page 526.
[100] L. Sommer, A. Krivokapic, S. Svelle, K.P. Lillerud, M. Stöcker, U. Olsbye, The Journal of Physical Chemistry C, volume 115, 2011, page 6521.
[101] K.M. Wang, J.H. Lunsford, The Journal of Physical Chemistry, volume 74, 1970, page 1512.
[102] J.C. Vedrine, C. Naccache, The Journal of Physical Chemistry, volume 77, 1973, page 1606.
[103] A. Abou-Kais, J.C. Vedrine, J. Massardier, Journal of the Chemical Society, Faraday Transactions 1: Physical Chemistry in Condensed Phases, volume 71, 1975, page 1697.
[104] R. Cases, D. Griscom, Nuclear Instruments and Methods in Physics Research Section B: Beam Interactions with Materials and Atoms, volume 1, 1984, page 503.
[105] I.A. Shkrob, B.M. Tadjikov, A.D. Trifunac, Journal of non-crystalline solids, volume 262, 2000, page 6.
[106] D.L. Griscom, Journal of Non-Crystalline Solids, volume 64, 1984, page 229.
[107] D. Dutt, P. Higby, C. Merzbacher, D. Griscom, Journal of non-crystalline solids, volume 135, 1991, page 122.
[108] R. Stoesser, J. Bartoll, L. Schirrmeister, R. Ernst, R. Lueck, Applied radiation and isotopes, volume 47, 1996, page 1489.
[109] S. Sorieul, T. Allard, G. Morin, B. Boizot, G. Calas, Physics and Chemistry of Minerals, volume 32, 2005, page 1-7.
[110] F. Holuj, J. Wieczorek, Journal of Magnetic Resonance, Journal of Magnetic Resonance, Volume 25, 1977, pages 1-241.
[111] W. Känzig, M. H. Cohen, Phys. Rev. Lett, volume 3, 1959, page 509.
[112] D. Dutt, P. Higby, D. Griscom, Journal of non-crystalline solids, volume 130, 1991, page 41.
[113] L. Barsova, T. Yurik, V. Spitsyn, Russian Chemical Bulletin, volume 35, 1986, page 879.
[114] J. Marks, W.T. Wenckebach, N. Poulis, Journal of Physics C: Solid State Physics, volume 13, 1980, page 5481.
[115] L.I. Barsova, T.K. Yurik, S.L. Orlov, M.B. Zubareva, Khimiya Vysokikh Ehnergij, 1990, page 329.
[116] L. Barsova, T. Yurik, S. Orlov, M. Zubareva, High energy chemistry, volume 24, 1990, page 284.
[117] S. Brunauer, P.H. Emmett, E. Teller, Journal of the American chemical society, volume 60, 1938, page 309.
[118] J.F. Ziegler, M.D. Ziegler, J.P. Biersack, Nuclear Instruments and Methods in Physics Research Section B: Beam Interactions with Materials and Atoms, volume 268, 2010, page 1818.
[119] S. Grangeon, F. Claret, Y. Linard, C. Chiaberge, Acta Crystallographica Section B: Structural Science, Crystal Engineering and Materials, volume 69, 2013, page 465.
[120] Geng, G., Myers, R.J., Qomi, M.J.A. et al., Sci Rep, volume 7, 2017, page 10986
[121] M. Holmboe, S. Wold, M. Jonsson, Journal of Contaminant Hydrology, volume 128, 2012, page 19.
[122] H.F. Taylor, Hydration of the calcium silicate phases, Chapter 5, in Cement chemistry, 2nd edition, Thomas Telford, 1997, page 119-120.
[123] K.J. Krakowiak, J.J. Thomas, S. Musso, S. James, A.-T. Akono, F.-J. Ulm, Cement and Concrete Research, volume 67, 2015, page 103.
[124] É.M. L'Hôpital, PhD thesis, EPFL, 2014.
[125] J S Pedersen and P Schurtenberger, Macromolecules, volume 29, 1996, page 7602-7612.
[126] W R Chen, P D Butler and L J Magid, Langmuir, volume 22, 2006, page 6539-6548.
[127] Z. Li, Fresh Concrete, Chapter 3, in Advanced concrete technology, John Wiley & Sons, 2011, page 94.
[128] R. Barrer, Pure and Applied Chemistry, volume 61, 1989, page 1903.

[129] R. Sierra, Rapport de recherche, Laboratoire Central des Ponts et Chausees (LCPC), volume 39, 1974, page 14-20.
[130] F. Nallet, R. Laversanne, D. Roux, Journal de Physique II, volume 3, 1993, page 487.
[131] M. Schönlein, J. Plank, Cement and Concrete Research, volume 106, 2018, page 33.
[132] V.I. Spitsyn, T.K. Yurik, L.I. Barsova, Bulletin of the Academy of Sciences of the USSR, Division of chemical science, volume 31, 1982, page 672.
[133] J.C. Vedrine, B. Imelik, E.G. Derouane, Journal of Magnetic Resonance Journal of Magnetic Resonance, volume 16, 1969, page 95-109.
[134] D.L. Griscom, C.I. Merzbacher, R.A. Weeks, R.A. Zuhr, Journal of Non-Crystalline Solids, volume 258, 1999, page 34.
[135] B. Henderson, J.E. Wertz, Defects in the alkaline earth oxides with applications to radiation damage and catalysis, volume 9, 1977, page 159.
[136] J. Rouquerol, D. Avnir, C. Fairbridge, D. Everett, J. Haynes, N. Pernicone, J. Ramsay, K. Sing, K. Unger, Pure and Applied Chemistry, volume 66, 1994, page 1739.
[137] K. Watcharathamrongkul, B. Jongsomjit, M. Phisalaphong, Sonklanakarin Journal of Science and Technology, volume 32, 2010, page 627.
[138] M. Kouzu, T. Kasuno, M. Tajika, Y. Sugimoto, S. Yamanaka, J. Hidaka, Fuel, volume 87, 2008, page 2798.
[139] H.J. Möckel, R.H. Köster, Nuclear Technology, volume 59, 1982, page 494.
[140] T. Yurik, G. Ionova, L. Barsova, V. Spitsyn, Radiation effects, volume 106, 1988, page 87.
[141] I. Lognot, PhD thesis, Université de Dijon, 1996.
[142] T. Bach, E. Chabas, I. Pochard, C.C.D. Coumes, J. Haas, F. Frizon, A. Nonat, Cement and Concrete Research, volume 51, 2013, page 14.
[143] B. Pastina, J.A. LaVerne, S. Pimblott, The Journal of Physical Chemistry A, volume 103, 1999, page 5841.
[144] C. Fourdrin, H. Aarrachi, C. Latrille, S. Esnouf, F. Bergaya, S. Le Caër, Environmental science & technology, volume 47, 2013, page 9530.
[145] M. Laine, Y. Liao, F. Varenne, P. Picot, L. J. Michot, E. Barruet, V. Geertsen, A. Thill, M. Pelletier, J.-B. Brubach, P. Roy, S. Le Caer, ACS Appl. Nano Mater, volume 1, 2018, page 5246-5257.
[146] M. Lainé, T. Allard, E. Balan, F.o. Martin, H.J. Von Bardeleben, J.-L. Robert, S.L. Caër, The Journal of Physical Chemistry C, volume 120, 2016, page 2087.
[147] M. Hyder, The Journal of Physical Chemistry, volume 69, 1965 page 4425.
[148] H.B. Pogge, F.T. Jones, The Journal of Physical Chemistry, volume 74, 1970, page 1700.
[149] P.-Y. Jiang, R. Nagaishi, T. Yotsuyanagi, Y. Katsumura, K. Ishigure, Journal of the Chemical Society, Faraday Transactions, volume 90, 1994, page 93.
[150] M. Daniels, E.E. Wigg, The Journal of Physical Chemistry, volume 71, 1967, page 1024.
[151] J. Manion, R. Huie, R. Levin, D. Burgess Jr, V. Orkin, W. Tsang, W. McGivern, J. Hudgens, V. Knyazev, D. Atkinson, NIST standard reference database, volume 17, 2008, page 20899.
[152] B. C. Boss, K.J. Fredeen, ICP-OES instrument, Chapter 3, in Instrumentation and Techniques in Inductively Coupled Plasma Optical Emission Spectrometry, Third Edition, Perkin Elmer Corporation, 1997, page 3.
[153] E.P. Barrett, L.G. Joyner, P.P. Halenda, Journal of the American Chemical society, volume 73, 1951, page 373.
[154] P. LLEWELLYN, J. ROUQUEROL, L. LUCIANI, R. DENOYEL, F. ROUQUEROL, Adsorption d'un gaz par un solide, Chapter 3, in Texture des matériaux pulvérulents ou poreux, Ed. Techniques Ingénieur, 2003, page 5-7.
[155] R, Philip, Introduction, Chapter 1, in Electron spin resonance: analysis and interpretation, Royal Society of Chemistry, 2007, page 1.
[156] G. Porod, Kolloid Z, volume 124, 1951, page 83.

ANNEX 1

ICP-AES analysis

Inductively Coupled Plasma - Atomic Emission Spectrometry (ICP-AES) is an emission spectrophotometric technique, exploiting the fact that excited electrons emit energy at a given wavelength as they return to ground state after excitation by high temperature Plasma. Argon gas was used to create the plasma and the plasma is sustained by a radio-frequency (RF) generator. When the plasma energy is absorbed by a sample, the component elements (atoms) are excited. When the excited atoms return to low energy position, emission rays (spectrum rays) are released and the emission rays that correspond to the photon wavelength are measured. The element type is determined based on the position of the photon rays and the content of each element is determined based on the ray intensities. Figure V. 1 shows the principle and major components of a typical ICP-AES instrument.

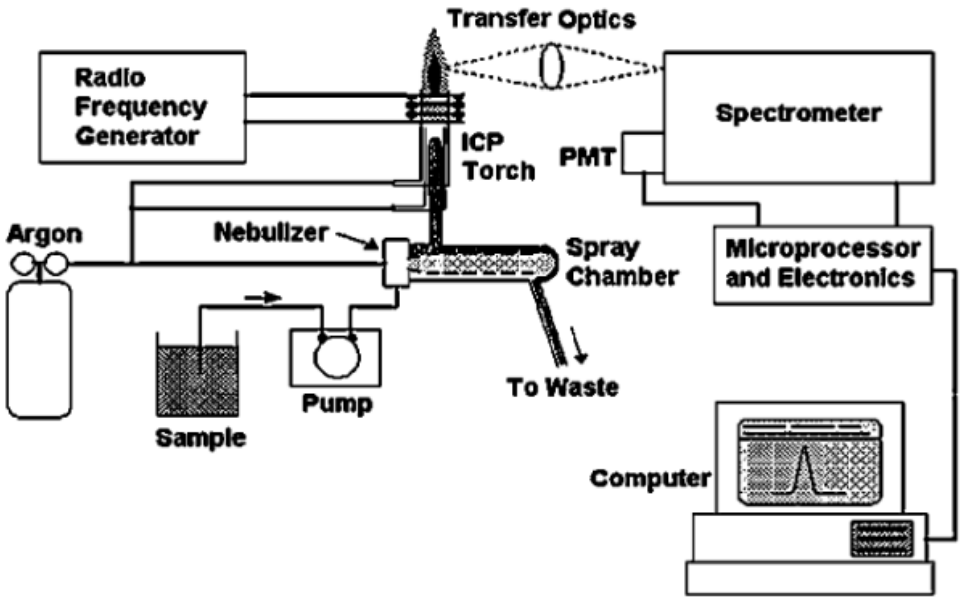

Figure V. 1. The principle and major components of a typical ICP-AES instrument [152].

ANNEX 2

XRD

XRD analysis is based on constructive interference of monochromatic X-rays and a crystalline sample: The X-rays are generated by a cathode ray tube, filtered to produce monochromatic radiation, collimated to concentrate, and directed toward the sample. The interaction of the incident rays with the sample produces constructive interference (and a diffracted ray) when conditions satisfy Bragg's Law (nλ=2d sin θ) (see Figure V. 2). This law relates the wavelength of electromagnetic radiation to the diffraction angle and the lattice spacing in a crystalline sample.

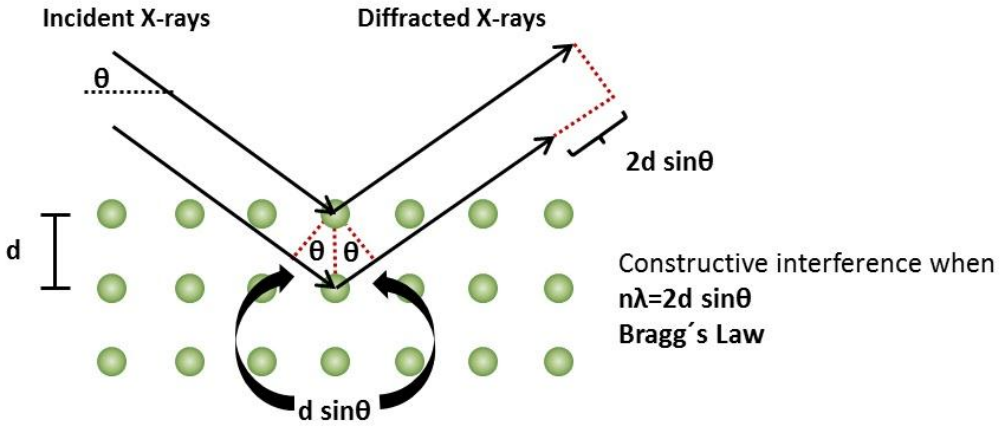

Figure V. 2. Schematic representation of the Bragg equation.

with λ, the wavelength of the incident X-rays (here, λ = 1.5418 Å),

n, an integer,

d, the depth between diffraction surfaces,

θ, the scattering angle between the incident X-rays and the diffraction surface.

ANNEX 3

The principle of nitrogen gas adsporption-desorption

The gas adsorption technique is performed by the addition of a known volume of gas (adsorbate), typically nitrogen, to a solid material in a sample vessel at cryogenic temperatures. At cryogenic temperatures, weak molecular attractive forces will cause the gas molecules to adsorb onto (attach to the surface of) a solid material. An adsorbate (gas) is added to the sample in a series of controlled doses, the pressure in the sample vessel is measured after each dosing. There is a direct relationship between the pressure and the volume of gas in the sample vessel. By measuring the reduced pressure due to adsorption, the ideal gas law can then be used to determine the volume of gas adsorbed by the sample. The resulting relationship of volume of gas adsorbed vs. relative pressure at constant temperature is known as an adsorption Isotherm. From the analysis, and the cross-sectional area of the adsorbate gas molecule, the surface area and pore size distribution of the sample can be derived.

SSA and porosity calculations from nitrogen gas adsorption-desorption

The generalized BET equation for gas adsorption is based on the following assumptions:

- Gas molecules physically adsorb on a solid in layers infinitely;
- Gas molecules only interact with adjacent layers;
- The Langmuir theory can be applied to each layer.

The resulting BET equation can then be described as follows (Brunauer et al. 1938):

$$v = \frac{v_m c\, p}{(p_0 - p)[1 + (c-1)(\frac{p}{p_0})]} \qquad \text{(V41)}$$

With v, the adsorbed volume of gas, in millilitres,

v_m, the adsorbed monolayer volume, in millilitres,

p, the equilibrium gas pressure, in Pascals,

p_0, the saturation pressure, in Pascals,

c, the BET constant.

This equation can then be rearranged as a linear function of p/p_0 as follows:

$$\frac{1}{v[\left(\frac{p}{p_0}\right)-1]}=\frac{c-1}{v_m c}\left(\frac{p}{p_0}\right)+\frac{1}{v_m c} \quad \text{(V42)}$$

The y-intercept and the slope of this function can then be used to determine the constants c (=slope/intercept +1) and v_m (=1/ (slope+intercept)). The specific surface area S, in cm^2/g can then be found by the equation:

$$S=\frac{v_m NA}{22{,}400\times m} \quad \text{(V43)}$$

with N, the Avogadro constant (6.022×10^{23} mol^{-1}),

A, the effective cross-sectional area of one adsorbate molecule, in square metres (0.162 nm^2 for nitrogen),

m, the mass of test powder, in grams.

Pore size distribution was obtained using Barrett Joyner Halenda (BJH) model [153] on the desorption isotherm using Kelvin equation:

$$ln\frac{p}{p^o}=\frac{-2\gamma V_l}{r_p RT}cos\,\theta \quad \text{(V44)}$$

With p, the equilibrium vapor pressure of a liquid contained in a capillary, in Pascals,

p^o, the equilibrium pressure of the same liquid over a free surface, in Pascals,

γ, the surface tension of liquid nitrogen, in mN/m,

V_l, the molar volume of liquid nitrogen, in L/mol,

r_p, the pore radius, in angstroms,

R, the universal gas constant,

θ, the contact angle (usually zero for liquid N_2).

The BJH method is based on a number of basic assumptions summarized in [154]:

- The porous texture is supposed to be rigid and consists only of independent mesopores and of well-defined shape,
- The filling of the pores does not depend on their location in the network,
- The multimolecular adsorption takes place on the surface of the mesopores in the same way as on a flat surface,
- The Kelvin law describing the pressure at which a gas condenses in a cavity is assumed to be applicable throughout the mesoporous domain.

ANNEX 4

Theory of Electron Paramagnetic Resonance (EPR)

Electron Paramagnetic Resonance (EPR) is a branch of magnetic resonance spectroscopy which utilizes microwave radiation to probe species with unpaired electrons, such as radicals, radical cations, and triplets in the presence of an externally applied static magnetic field.

Electron paramagnetic resonance (EPR) is similar to the nuclear magnetic resonance (NMR) where both of them describe the case of resonance of an atomic particle as a result of high-frequency electromagnetic radiation absorption in the presence of external magnetic field. The main difference is that NMR is related to nucleus, while EPR is related to the unpaired electron.

The electron, as a charged rotating particle, possesses a magnetic field which makes the electron appears as a minute magnet [155]. In normal cases, for the unpaired electron (single electron), the spin energy levels are degenerate, and electrons spin randomly.

After applying an external magnetic field, spin energy levels split, and electrons spin either aligned to or opposite to the direction of the magnetic field. Splitting of the spin energy levels results in the emergence of some energy difference (ΔE); hence, electrons aligned parallel to the external magnetic field and occupying the lower energy level are more than those aligned antiparallel to the external magnetic field and occupying the upper energy level.

When incident photon energy (hv) matches the energy difference between the two energy levels, some electrons are excited in the upper energy level and flip their spin direction. After a time (t1), the relaxation time, excited electrons return to their original state emitting photons whose energy is equal to ΔE (see Figure V. 3.).

Such process is expressed by the following formula:

$$\Delta E = h\nu = g\mu_B H_0 \qquad \text{(V45)}$$

Where μ_B is the Bohr magneton and g the gyromagnetic factor which is 2.0023 for free electron and H_0 the magnetic field. To induce transition between the energy levels, the electron should absorb a quanta of energy $h\nu$ (h is Planck's constant).

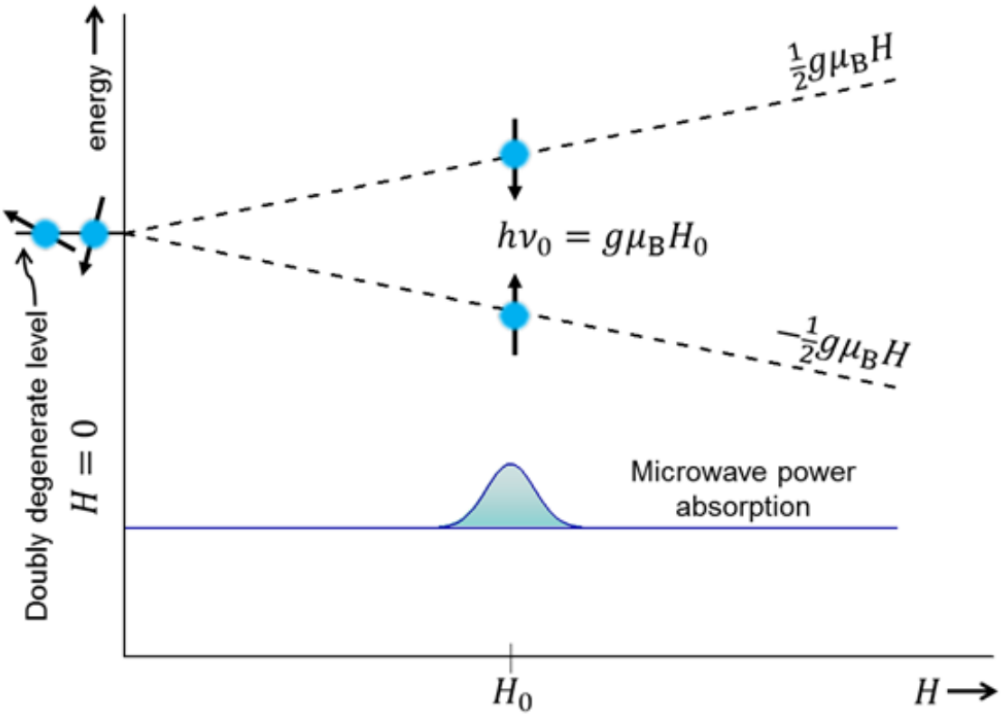

Figure V. 3. Energy diagram showing the origin of an electron spin resonance signal.

Then g value is given below:

$$g = \frac{714.4775 \times \gamma(GHz)}{H_0(mT)} \quad \text{(V46)}$$

The g-factor of the paramagnetic center is sensitive to its constituting atoms due to spin-orbit coupling. In most cases, it is a tensor that mirrors the electronic structure of the paramagnetic centres resulting from the interaction of crystal field with orbitals.

In a spectrum, the hyperfine coupling constant 'A' is directly related to the distance

(Figure V. 4.) between peaks and its magnitude indicates the extent of delocalization of the unpaired electron over the molecule.

In the Figure V. 4, the hyperfine coupling constant could be expressed as:

$$A = H_2 - H_1 \quad \text{(V47)}$$

$$A(MHz) = \frac{4.6683E-5}{10^6} \times g \times A(Gauss) \times c(cm.s^{-1}) \quad \text{(V48)}$$

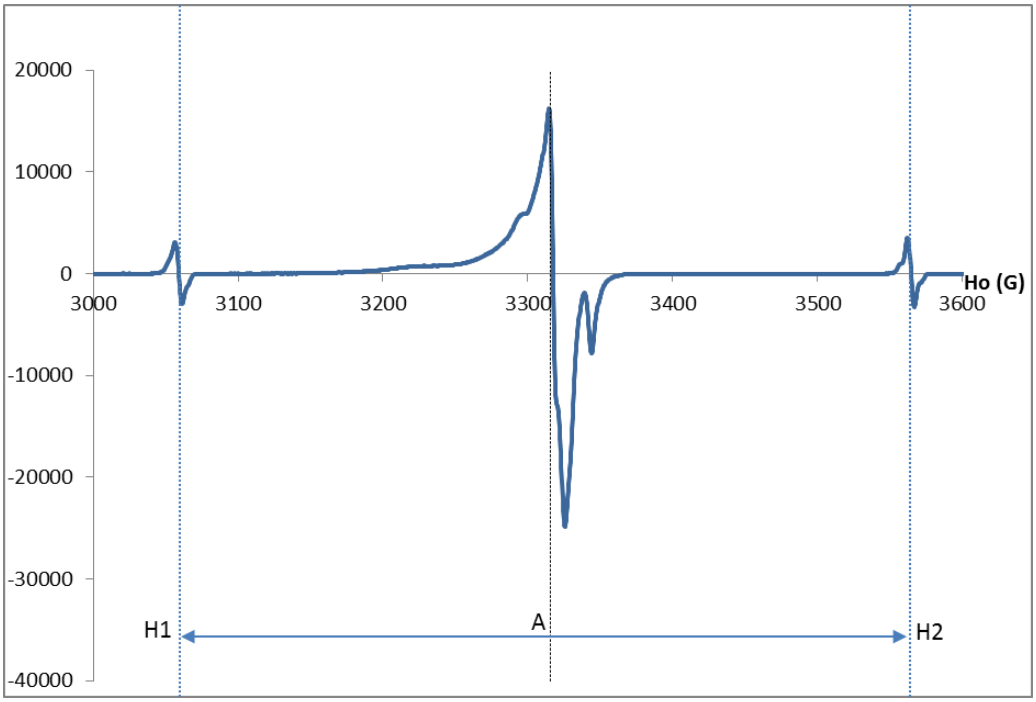

Figure V. 4. EPR spectra of irradiated 0.80 CSH RH 30% at 30kGy recorded at 100K.

ANNEX 5

The principle of SAXS

SAXS can determine the nanoscale structure of solids, liquids and gaseous particulate matter of almost any material, including colloids of all types. The method is non-destructive with minimal sample preparation, and may equally be applied to metals, polymers, proteins, oils, or ceramics, among others.

This is achieved by analyzing the elastic scattering behaviour of X-rays when travelling through the material, recording their scattering at small angles (typically 0.1 - 10°, hence the "Small-angle" in its name). It belongs to the family of small-angle scattering (SAS) techniques along with small-angle neutron scattering, and is typically done using hard X-rays with a wavelength of 0.07 - 0.2 nm. Depending on the angular range in which a clear scattering signal can be recorded, SAXS is capable of delivering structural information of dimensions between 1 and 100 nm, and of repeat distances in partially ordered systems of up to 150 nm. The detected scattering pattern is characteristic for the nanostructures of the sample and can be used to determine important structural parameters such as particle size, shape, internal structure, porosity, and arrangement (orientation).

SSA calculations from SAXS

When the model fits the Porod function:

I(q) = C/q^4

Here C = $2\pi\Delta\rho^2$ S/v is the scale factor where S/v is the specific surface area (ie, surface area / volume) of the sample, and Δρ is the contrast factor.

Then, the specific surface area is calculated based on Porod's theory [156], as follows:

$$S/v = \frac{1}{\varphi_G} \lim_{q \to 0} (I_{Abs} q^4)/2\pi\Delta\rho^2 \qquad \text{(V49)}$$

S/v : Specific surface (ie, surface area / volume) of the sample (cm^2/cm^3)

φ_G: Volume fraction of the grain

$I_{Abs} = I_{measured}/E_{effective}$ (to normalize the intensity in order to remove the packing effect)

$E_{effective} = -\ln(T)/\mu(C\text{-}S\text{-}H)$

$\mu C_aS_bH_c = a\mu_{CaO} + b\mu_{SiO2} + C\mu_{H2O}$

μ_{solid} : mass attenuation coefficient

T : transmission

μ : Mass attenuation coefficient

I_{Abs}: absolute intensity

q(diffusion vector) = $(4\pi/\lambda)\sin(\theta)$, in $Å^{-1}$

λ : neutron wavelength

2θ : scattering angle

ρ: scattering length density

$\Delta\rho$ (electronic density between C-S-H and air) = $SLD_{CSH} - SLD_{AIR} = 2.14\times10^{-5}$

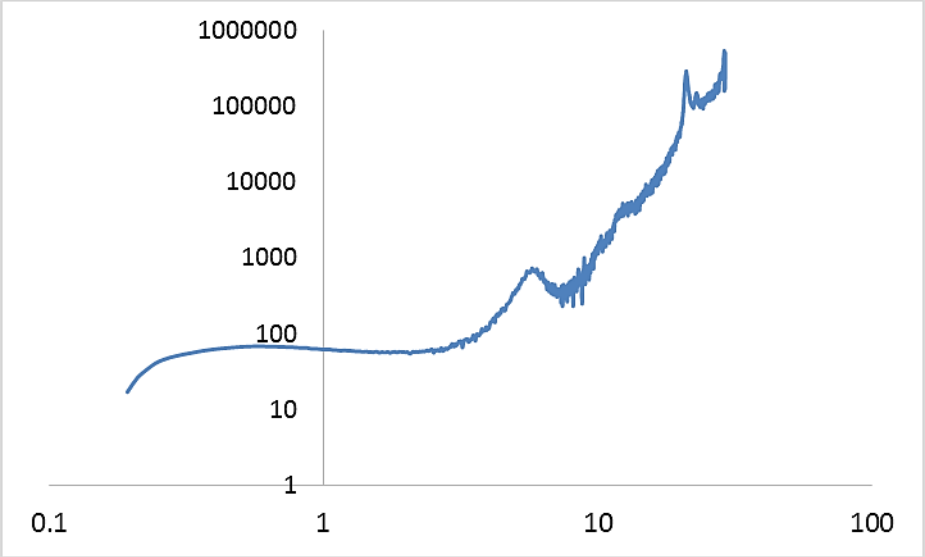

Figure V. 5. The plot of Ln(q) and Ln($I_{Abs}\,q^4$)

In Figure V. 5, y value of the plateau corresponds to $\frac{1}{\varphi_G}\lim_{q\to 0}(I_{Abs}q^4)$, consequently the specific surface area could be calculated by equation V49.

ANNEX 6

Theoretical calculation

The calculation was based on the following equation:

$$C2S+H_2O \rightarrow CSH+CH \quad \text{(V50)}$$

We assume C/S ratio in CSH is 1.6.

Using the Extreme value method, by assuming C2S is completely reacted, to calculate a theoretical portlandite. Then use the real quantity of portlandite determined by TGA analysis. Then the amount of reacted C2S could be deduced.

Titre : Production d'hydrogène des silicates de calcium hydratés sous irradiation

Mots clés : Radiolyse de l'eau, C-S-H, production de gaz H_2, défauts induits par le rayonnement

Résumé : En France, les matériaux à base de ciment sont utilisés comme matrice de conditionnement des déchets nucléaires de faible et moyenne activité. La radiolyse de l'eau est due aux déchets nucléaires stockés dans les matériaux. La formation de ses produits radiolytiques tels que le gaz H_2 doit être évaluée pour des raisons de sécurité. Les silicates de calcium hydratés (C-S-H) représentent le principal produit (50%) d'hydratation du ciment Portland (CP). L'objectif de cette étude est de comprendre les mécanismes radiolytiques de la production d'hydrogène dans les C-S-H, d'étudier l'effet d'impuretés (telles que des ions alcalins, hydroxydes ou nitrates supplémentaires) sur la production de gaz H_2 dans les C-S-H et d'examiner l'existence d'interactions entre les phases principales (C-S-H et portlandite) du ciment Portland. Après avoir caractérisé les échantillons par diverses techniques, ils ont été soumis à différents types d'irradiation (faisceaux gamma et électrons et ions lourds (HI)) pour déterminer leur rendement radiolytique en H_2, $G(H_2)$. Dans les C-S-H, il a été démontré que, sous irradiation gamma, la production d'H_2 est indépendante de la teneur en eau et que les C-S-H produisaient autant d'H_2 que la même masse d'eau. Ainsi, le mécanisme de production d'hydrogène est très efficace dans les C-S-H. La comparaison entre les résultats obtenus sous rayons gamma et ceux obtenus sous HI implique qu'il n'y a pas ou peu d'effet de transfert d'énergie linéique (TEL) dans les C-S-H. Ainsi, les réactions de recombinaison semblent limitées. L'introduction d'ions nitrates dans la structure des C-S-H induit une diminution importante du $G(H_2)$. L'irradiation des hydrates de C2S et C3S constitués majoritairement de C-S-H et de portlandite indique qu'il n'y a pas de phénomènes de transfert d'énergie entre ces phases. Enfin, les expériences de spectroscopie par résonance paramagnétique électronique (RPE) ont permis de proposer des mécanismes radiolytiques dans les C-S-H. L'ensemble de ces résultats nous permettent de mieux comprendre les effets d'irradiation dans les ciments.

Title : Hydrogen production from irradiated calcium silicate hydrate

Key words : Water radiolysis, C-S-H, H_2 gas production, radiation-induced defects

Abstract : In France, cementitious materials are used as conditioning matrix of low level and intermediate level nuclear wastes. Water radiolysis occurs due to the nuclear wastes stored in the materials. The formation of its radiolytic products such as H_2 gas must be evaluated for safety reasons. Calcium silicate hydrate (C-S-H) is the main product (50%) of hydration of Portland Cement (PC). The aim of this study is to understand the radiolytic mechanisms of the hydrogen production in C-S-H, to investigate the effect of impurities (such as alkali ions, additional hydroxides or nitrates ions) on H_2 gas production in C-S-H and to examine if interactions exist between different main phases (C-S-H and portlandite) in cement matrix. After using various characterization techniques, samples were submitted to different types of irradiation (gamma rays and electrons and heavy ions (HI) beams) to determine their H_2 radiolytic yield, $G(H_2)$. In C-S-H system, it has been shown, under gamma irradiation, that $G(H_2)$ does not depend on water content, moreover, C-S-H system itself produce efficiently H_2 gas. The comparison between the results obtained under gamma rays and that obtained under HI implies: there is no/ low LET effect in C-S-H. While with nitrate ions in C-S-H, a large decrease of $G(H_2)$ is observed. Irradiation of C2S and C3S hydrates mainly composed of C-S-H and portlandite shows that here is no energy transfer phenomena between these two phases. Finally, the electron paramagnetic resonance (EPR) spectroscopy experiments have enabled proposing radiolytic mechanisms. All these results help us to understand the radiation effects in cements.

Université Paris-Saclay
Espace Technologique / Immeuble Discovery
Route de l'Orme aux Merisiers RD 128 / 91190 Saint-Aubin, France